Organic semiconductors in the limit of a few monolayers: Molecular surface doping of pentacene thin film transistors

Inauguraldissertation

zur

Erlangung der Würde eines Doktors der Philosophie

vorgelegt der

Philosophisch-Naturwissenschaftlichen Fakultät

der Universität Basel

von

Tatjana Hählen

aus Lenk (Bern)

UNI
BASEL

Villigen, 2014

Genehmigt von der Philosophisch-Naturwissenschaftlichen Fakultät auf Antrag von:
Prof. Dr. Thomas Jung
Dr. Michel Calame

Basel, den 10. Dezember 2013

Prof. Dr. Jörg Schibler
Dekan

Abstract

In this thesis the transport in organic semiconductors is investigated at the nanoscale. For this, organic thin film transistors with channel thickness in the limit of a few monolayers have been successfully fabricated and characterized *in-situ* in vacuum. The electronic properties in such devices were tuned by the addition of guest molecules onto the surface of the device-active semiconductor layer (surface doping). Different dopant molecules were used and the length scale of the doping induced charge transfer was studied to get further insight into the doping mechanism in organic semiconductors. An improved understanding of the doping process enables the design of a variety of organic devices, which can contribute to the future of ubiquitous computing by their low cost and flexibility. Further, the addition of guest molecules on the semiconductor surface provides a simple and effective, as well as flexible, doping method: both local variations of the concentration and of the type of guest molecules can be readily controlled. The here presented results can contribute to the design of organic chemical sensor devices where the analyte either takes the role of a surface dopant or reacts with the functionalized guest molecules. Possible applications of such sensors could comprise their use in future lab on a chip devices.

As a key parameter to study the transport in such thin devices, controlled film growth of the active material was achieved. High quality films of pentacene, the organic semiconductor studied in this thesis, were deposited in the channel of the organic thin film transistors, on the gate dielectric SiO_2. With molybdenum oxide (MoO_x) as the electrode material in the bottom contact thin film transistors, the high quality pentacene film also extends across the contact edge and establishes good electrical contact. In transport measurements even the completion of each pentacene monolayer was detected during the deposition of these high quality films.

Subsequent surface doping of these pentacene thin film transistors was demonstrated to be efficient to increase or decrease the charge carrier density depending on the nature of the guest molecule. Especially the strong electron acceptor F_4TCNQ (2,3,5,6-

tetrafluoro-7,7,8,8-tetracyanoquinodimethane) increased the hole concentration, as recognized by a shift of the transfer curves towards positive voltage, whereas the porphyrin MnTPPCl (manganese(III)-tetraphenylporphyrin-chloride) decreased the hole concentration. Interestingly, surface doping with a second and similar porphyrin CoTPP (cobalt(II)-tetraphenylporphyrin) did not induce a change in the carrier concentration. Complementary to the transport measurements, the doping mechanism was further investigated by photoelectron spectroscopy: The surface doping induced variation of the charge carrier density can be associated to a charge transfer with pentacene in the case of F_4TCNQ, whereas in the case of MnTPPCl it is tentatively associated to the molecular dipole moment in MnTPPCl.

Furthermore, the length scale of the surface doping induced charge transfer was found to be in the order of one monolayer. This was investigated by measuring the F_4TCNQ surface doping efficiency for a series of transistors with increasing pentacene film thickness. The results show that the surface doping induced charge carriers are essentially confined within the top pentacene monolayer and that the F_4TCNQ molecules do not diffuse through the different monolayers. These results are compared to calculations and to the presence (or absence) of a saturation in the source-drain current with increasing channel thickness.

These results show that surface doping is effective to change the charge carrier density in organic thin film transistors at the nanometer scale. Moreover, surface doping provides an interesting tool to investigate the effect of different guest molecules, where the detailed molecular structure crucially determines the resulting doping effect, and to gain further insight into the doping mechanism in organic semiconductors such as the demonstrated strong localization of the doping induced charge carriers.

Contents

CHAPTER 1

Introduction

Use of electronic devices is constantly increasing. Today most people do not only possess a simple cell-phone but rather a smart phone including also many different additional functionalities. Also the different devices are more and more interconnected and today there exists for example the possibility to control remotely the temperature or the position of the blinds at home. So far most of these devices are based on inorganic semiconductor devices. In particular transistors are present in large numbers in such devices. On the way to ubiquitous computing inorganic semiconductors are complemented by organic semiconductors. Organic semiconductors have a few advantages over inorganic semiconductors and allow for applications which are difficult to be realized with inorganic semiconductors. More specifically organic semiconductor devices are interesting because of their low price and their mechanical flexibility. Low temperature processing makes them suitable for flexible substrates such as plastics and solution processing as *e.g.* printing technologies allow for the fabrication of large area devices. These properties open the path to ubiquitous and low-cost organic electronic appliances on plastic [1] as well as for disposable electronics. Three main devices are fabricated from organic semiconductor materials: organic light emitting diodes (OLEDs), organic photovoltaic cells and organic thin-film transistors (OTFTs). OLEDs are currently well established in commercial products (*e.g.* in cell phones but also in TVs) and are in significant aspects performing better in displays than liquid crystal displays. Applications of OTFTs include flexible integrated circuits, simple low-cost radio-frequency identification (RFID) tags (*e.g.* to replace the optical bar code), sensing devices, but also back planes for

flexible displays[1]. Flexible displays allow the fabrication of electronic paper displays and roll-up displays. Sony demonstrated in 2010 an OTFT-driven OLED display which could be rolled up onto a pen [6]. But also more sophisticated products such as electronic artificial skins (e-skin) are envisaged, where among others pressure sensors could provide touch recognition for next-generation robots.

For organic semiconductor materials both small molecules and polymers are used. Polymers can provide a good stability in air, in moisture and when exposed to light. This provides the advantage that no encapsulation is needed. Solution-based processing opens the way to a roll-to-roll processing and finally to ultra-low cost electronics. On the down side, however, polymers exhibit rather low mobilities due to the larger molecular disorder. Here organic semiconductor materials consisting of small molecules provide an advantage as more ordered films and thus higher mobilities are more readily obtained. Also purification of small molecules is generally easier. However, solution processing of small molecules is a greater challenge for small molecules because of the generally low solubility.

Since the first OTFT in 1986 [7] with a mobility of $\sim 10^{-5}$ cm^2/Vs large technological progress was made. Today OTFT with mobilities comparable to amorphous silicon in the order of $\sim 0.5-1$ cm^2/Vs can be produced. This mobility range is considered as a benchmark for more demanding applications. Such improvements have been brought along by new, tunable organic semiconductor materials and the tailoring of their characteristics and structure [8, 9], but also by improved dielectrics, circuit design and processing techniques (See *e.g.* the review by Klauk [10]).

The main difference between organic semiconductors and inorganic semiconductors lies in their different electronic structure. In inorganic semiconductors the atoms are covalently bonded whereas the molecules in organic semiconductors are held together by the weak van der Waals forces. An organic semiconductor is therefore closer to an insulator than to a semiconductor. These weak intermolecular forces lead to only weak overlap of the electronic orbitals of the molecules and therefore to narrow electronic bands ($\sim$ 0.1 eV), which is two orders of magnitude lower than in silicon. Also this characteristic difference leads to low mobilities μ in the range of $0.01-10$ cm^2/Vs, which is significantly lower than in inorganic semiconductors ($\mu = 100 - 10^4$ cm^2/Vs [11]). The individual molecules, polymers or small molecules, in the organic semiconductor are largely composed of *conjugated* chemical bonds where the π orbitals are delocalized across a large part of the molecule. The electron transport is therefore not limited by the electron transport within an individual molecule but rather by the electron transfer

[1] Alternative to organic backplanes, flexible OLED displays with backplanes based on amorphous or polycrystalline silicon, or based on transition metal oxides (TMO) are also investigated. (See Ref. [2] for an overview on flexible electronics). Among the TMO, amorphous indium gallium zinc oxide (a-IGZO) has gained interest due to its large mobility > 10 cm^2/Vs and possible room temperature fabrication making it suitable for plastic substrates [3–5].

between the molecules in the bulk organic semiconductor. Except for highly purified single crystals at low temperatures, charge transport in organic semiconductors can thus not be described by the band picture but is better described by a polaron hopping transport. A hopping transport means that the charge carrier jumps from an ionized molecule to an adjacent neutral molecule as schematically illustrated in Figure 1.1. The term polaron refers to the fact that a charge polarizes the neighboring region, which means that not a "naked" charge moves through the organic semiconductor but rather a "dressed" charge where the polarized cloud moves with the charge [12]. Note that in inorganic semiconductors the charge moves faster than the time needed for the formation of such a cloud. In the general case of an organic semiconductor material the charge transport properties depend on the packing of the molecules and the degree of ordering in the organic semiconductor, and on the density of impurities and structural defects [13]. This means that the mobility is related to the quality of the sample [14]. For a more detailed discussion the reader is referred to books treating the different aspects of organic semiconductors especially for their application in OTFTs [12, 15].

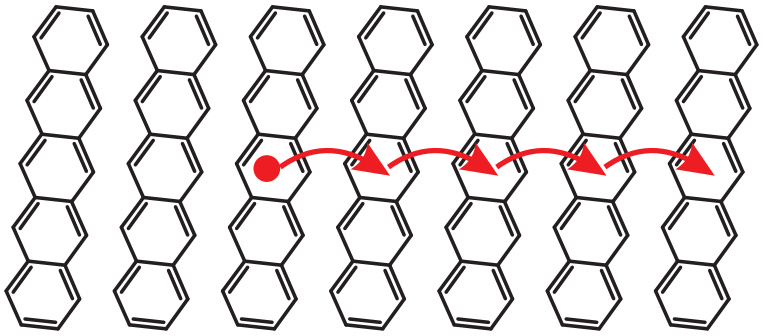

Figure 1.1: Schematic illustration of hopping transport.

Similar to the case of inorganic semiconductor materials it is also desired to tune the charge carrier density in organic semiconductors by doping. Only the controlled doping of inorganic semiconductors, mainly of silicon, enabled the large variety of semiconductor devices. Doping in organic semiconductors was mostly studied in OLEDs. Doping in OLEDs was shown to increase the conductivity by several orders of magnitude and to make ohmic contacts by generation of narrow space charge regions at the contacts which allow charge injection by tunneling. By doping, the driving voltage could therefore be reduced. Additionally the formation of the ohmic contact allows for a wider choice of electrode materials to be used as the work function has no more to be aligned with the energy level of the semiconductor. The large conductivity of the doped material also allows to tune the thickness of the OLED cavity for a better outcoupling efficiency without introducing additional voltage losses. Similarly the controlled doping of organic semiconductor materials in organic solar cells allows to adjust the thickness of the doped window layer for efficient optical design. Likewise to OLEDs also here doping induced

ohmic contacts which reduce undesired voltage drops across the contacting interfaces (for a recent review of doping in OLED and organic solar cells see *e.g.* Ref. [16]).

Doping in organic semiconductor materials follows the same basic principles as they are known in inorganic semiconductors: Electron donors or acceptors are introduced into the organic semiconductor material and will increase the respective charge carrier density. For n-type doping the highest occupied molecular orbital (HOMO) of the dopant should by at higher or comparable energy than the lowest unoccupied molecular orbital (LUMO) of the host semiconductor to enable electron transfer from the HOMO of the dopant to the LUMO of the semiconductor. Similar for p-type doping the LUMO of the dopant should be at comparable or lower energy than the HOMO of the semiconductor to extract electrons from the HOMO of the semiconductor. For p-type doping a variety of dopant-semiconductor combinations have been studied [17], where F_4TCNQ (2,3,5,6-tetrafluoro-7,7,8,8-tetracyanoquinodimethane) is a strong electron acceptor and thus a widely used p-dopant. N-type dopants are generally harder to find as the requested high lying HOMO reduces their stability against oxidation. Here mainly three approaches are used: (1) doping with alkali metals which raise the issue of uncontrolled diffusion of the dopants, (2) doping by molecules with very high HOMO levels and (3) doping by air-stable precursor molecules which will only donate an electron after activation by *e.g.* heat or illumination [16]. Molecular dopants are generally introduced in the semiconductor matrix by co-evaporation of the dopants and the matrix material, but also by solution-based doping [18].

Similar to OLEDs, doping in OTFTs is applied to reduce the contact resistance. The contact resistance in OTFTs is often relatively large with respect to the channel resistance and thereby limits the down-scaling of the channel dimensions because at small dimensions the contact resistance may become the dominating resistance (see *e.g.* Ref. [19]). Comparable to OLEDs, it is thus desirable to obtain ohmic contacts in OTFTs, meaning the contact resistance should be much smaller than the channel resistance. In principle low contact resistances should be reached by choosing the electrode material such that its work function aligns with the HOMO (p-type) or LUMO (n-type) level of the organic semiconductor. The formation of an interface dipole, however, shifts the vacuum level of the organic semiconductor with respect to the metal and makes thus the appropriate choice of the electrode material difficult [20]. Also Structural disorder in the organic semiconductor near the contacting interface can contribute to an increased contact resistance (see Chapter 2.4 in Ref. [12]). To reduce the contact resistance, several groups studied the selective doping of the contact interface; this was either done by introduction of a thin layer of the dopant molecules at the interface between the semiconductor and the electrodes [21–23], or by a doped layer, obtained by co-evaporation of the dopant and the semiconductor, at the electrode-semiconductor interface [24, 25]. A reduction of the contact resistance was also observed by Vanoni *et al.*

in OTFT where the complete organic semiconductor, in this case pentacene, was bulk doped with F_4TCNQ, *i.e.* by co-evaporation of the pentacene and F_4TCNQ [26]. This reduction of the contact resistance is associated to a reduction of the charge injection barrier height [27].

Doping the complete OTFT channel with F_4TCNQ not only modifies the contact resistance but also the charge carrier density in the channel as observed by a shift of the transfer curves [26]. Temperature dependent measurements revealed also a modified density of state (DOS) for F_4TCNQ doped pentacene; an additional peak in the DOS was observed at $\sim$ 140 meV above the HOMO level of pentacene [27]. In addition, Abe *et al.* observed an increased conductance as well as a shifted transfer curve for pentacene OTFT with top contacts containing a F_4TCNQ layer on top of the channel [28]. Wakatsuki *et al.* showed that placing F_4TCNQ doped pentacene layers 10 nm or 20 nm above the source and drain electrodes enhances the transistor characteristics of pentacene OTFT, *i.e.* larger source-drain currents were observed without shifting of the transfer curves [29]. An additional method to modify the charge carrier density in the channel, respectively the threshold voltage of OTFTs, is the use of self-assembled monolayers (SAM) on the insulator surface [30–32]. This effect is generally associated to the electric dipole of the molecules forming the SAM [30–32]. Due to the same dipole, these effects are also observed when the SAMs are placed in between gate electrode and insulator [33], which does therefore not correspond to a doping in the sense of a charge transfer between dopant and organic semiconductor. However, also some degree of weak charge transfer between the organic semiconductor and SAMs has been observed [30].

A different approach for doping will be used in this thesis: surface doping, also named surface transfer doping. By surface doping the dopants are not imbedded into the host matrix but placed on the surface of the semiconductor [34]. Surface doping does therefore not modify the structure of the semiconductor and can be applied for a variety of dopants (see Ref. [35] for a review on surface doping of semiconductors). Surface doping was mostly applied to diamond [36–38], but also to silicon [39], germanium [40] and silicon [41] nanowires, carbon nanotubes [42] and graphene [43, 44]. Also the above mentioned use of SAMs, usually applied at the interface between the organic semiconductor and the insulator, can be considered as surface doping if a charge transfer occurs. In this thesis surface doping will be performed on pentacene OTFT with bottom contacts by deposition of molecular dopants such as F_4TCNQ on top of the channel.

Even though doping was successfully applied for a number of dopants and organic semiconductors, the understanding of the doping mechanism is still rudimentary. The models describing doping in inorganic semiconductors cannot be applied to doping in organic semiconductors; the dielectric constant ϵ of organic semiconductors is low compared to inorganic semiconductors, giving rise to increased electrostatic interactions between electrons and holes but also between charge carriers and fixed ions, and the

usually larger effective mass in organic semiconductors reflects the more localized wave functions [16, 45]. These differences lead to the fact that the interaction of the doping induced charge carriers with the dopant ion is enhanced by the Coulomb interaction. Additionally molecular dopants and organic semiconductor molecules are not symmetric, which may also lead to anisotropic doping. In a few recent studies the doping in the model semiconductor pentacene with the widely used acceptor molecule F_4TCNQ was studied: Salzmann *et al.* provide evidence for a hybridization between the electronic states in the molecular dopant and in the organic semiconductor. Instead of an integer electron transfer from the HOMO of the organic semiconductor to the LUMO of the dopant, this hybridization is suggested to reduce the doping efficiency [46]. Theoretical studies by Mityashin *et al.* show that the interaction between dopant molecules is important to overcome the Coulomb potential associated with the parental dopant ion, indicating that there should be a threshold doping concentration below which doping efficiency will be small or zero [47]. An STM study of pentacene with subsequent deposition of a small amount of F_4TCNQ by Ha and Kahn revealed that the F_4TCNQ molecules preferentially diffuse to pentacene vacancies and that the donated hole remains localized near the dopant [48].

In this thesis doping of pentacene OTFTs is studied in progress of the work by Vanoni *et al.* who studied pentacene OTFT bulk doped with F_4TCNQ and observed an increase of the charge carrier density, reflected by a shift of the transfer curves and by additional states in the DOS. Also they observed a reduction of the contact resistance related to the lowering of the charge injection barrier at the gold-pentacene interface [26, 27]. Instead of bulk doping of the channel materials used by Vanoni, here surface doping is used which easily allows to control the gradual increase of doping concentration in one single device as well as the study of different molecular dopants. Initial work from Vanoni already demonstrated that surface doping on pentacene OTFT is feasible [49]. Pentacene was chosen as the organic semiconductor due to its model character [50] and its high mobility of up to 3 cm^2/Vs in OTFT [51]. Surface doping on pentacene OTFTs is applied to study the effect of different molecular dopants in transport experiments. The results are compared with photoelectron spectroscopy measurements to clarify the different nature and effect of the doping by the molecules. To study the length scale of the charge transfer induced by surface doping, F_4TCNQ surface doping is studied on pentacene OTFT with different channel thickness. Due to the confinement of the current to a narrow layer next to the insulator surface in OTFT devices [52–54], surface doping will only affect the transport characteristics when the charge transfer extends down to this narrow layer. Consequently the doping efficiency as a function of the channel thickness will provide a measure of the charge transfer length. Additionally the effect of different film morphologies, both in the channel and next to the contact regions, is discussed with respect to contact resistance, mobility and surface doping efficiency.

In this thesis I will first, in Chapter 2, introduce the working principle of the thin film transistor and explain how important device performance characteristics such as the mobility, the threshold voltage and the contact resistance can be extracted from transport measurements. Further, the fabrication procedure of the pentacene OTFT will be presented, as well as the methods to characterize the film morphology.

In Chapter 3 the morphology of the pentacene films produced under different growth conditions is studied both in the OTFT channel and in proximity of the electrodes. The morphology of the device active layer is then discussed with respect to their contact resistance and mobility. Additionally, the confinement of the current next to the bottom of the channel, close to the insulating gate-oxide is investigated by measuring the evolution of the current during pentacene evaporation. Next, surface doping with different molecular dopants is discussed in Chapter 4 on the basis of transport measurements performed with pentacene OTFTs and then, in Chapter 5, compared to photoelectron spectroscopy measurements. In Chapter 6 we study surface doping with F_4TCNQ on pentacene OTFT with different channel thickness to investigate the dimension of the charge transfer layer induced by the surface dopant. These results are compared to calculations of the charge carrier density with respect to the distance from the semiconductor-insulator and semiconductor-dopant interface respectively.

Besides the research on the doping mechanism in pentacene OTFT, I was involved in on-surface magnetochemistry experiments performed at the SIM beamline at the Swiss Light Source (SLS) in the Paul Scherrer Institute. These experiments, where I was mainly responsible for the sample fabrication during the synchrotron beamtime sessions, resulted in several papers. A brief overview of these experiments is described in Appendix A.

CHAPTER 2

Fabrication and characterization of organic thin film transistors

This thesis explores the effect of surface doping on Pentacene thin film transistors (TFT). In this chapter the basic functionality of organic TFTs is explained as well as the parameters which can be obtained from transport measurement on such TFTs. The fabrication of the TFTs as well as the experimental setup are described.

2.1 Organic thin film transistor

An organic TFT, as an inorganic TFT, is an active device with three contacts; source, drain and gate. The active part of the device consists of a thin organic semiconductor layer in contact with the two electrodes denominated source and drain. The third electrode, the gate, is situated parallel to the active layer, electrically isolated from the organic semiconductor by a thin insulator layer. By applying a gate voltage (V_g) between the gate and source electrode, an accumulation layer is induced at the semiconductor-insulator interface, thus leading to a conductive channel between the source and drain electrodes. The gate voltage thus controls the charge carrier density in the active material and therefore, for a given applied drain-source voltage (V_{ds}), the current between the two electrodes (I_{ds}) depends on the applied V_g.

2.1.1 Threshold voltage and mobility

As stated above, the drain-source current I_{ds} depends on both the gate voltage V_g and the source-drain voltage V_{ds}. This dependency on the two voltages can be measured

in two ways: either by measuring the *output characteristics*, where I_{ds} as a function of V_{ds} is plotted for different fixed V_g values, or by measuring the *transfer characteristics*, where I_{ds} is plotted as a function of V_g at a given V_{ds}. In the output characteristics one distinguishes two regions; the linear regime at low V_{ds}, where I_{ds} varies linearly with V_{ds}, and the saturation regime at large V_{ds}, where I_{ds} is no longer controlled by V_{ds} but only by V_g. In those two regimes the currents can be expressed by the following equations [11, 55]:

$$I_{sd,lin} = \frac{W}{L} C_{ox} \mu (V_g - V_{g,th}) V_{ds} \tag{2.1}$$

$$I_{sd,sat} = \frac{W}{2L} C_{ox} \mu (V_g - V_{g,th})^2 \tag{2.2}$$

where: L – the channel length,
W – the channel width,
$C_{ox} = 23\text{nF/cm}^2$ – gate capacitance,
μ – mobility in the semiconductor [cm^2/Vs], and
$V_{g,th}$ – threshold voltage.

The threshold voltage $V_{g,th}$ is the on-set voltage for which a conductive channel is formed between source and drain electrodes. With those equations we can therefore extract both the mobility of the semiconductor as well as the threshold voltage. In this thesis the values are extracted from the transfer characteristics in the linear regime, with generally $V_{ds} = -5\text{V}$. In this case $V_{g,th}$ follows from a linear fit to the transfer curve and its intersection with the V_g axis at $I_{ds} = 0$. The mobility μ_{TFT} can be extracted from the slope of the same linear fit:

$$\mu_{TFT} = \frac{L}{W C_{ox}} \frac{1}{V_{ds}} \frac{\partial I_{ds}}{\partial V_g} \tag{2.3}$$

Due to charge neutrality, the amount of induced charges per area p for an applied V_g can be expressed as

$$p(V_g) = \frac{C_{ox}}{e} V_g \tag{2.4}$$

However, the amount of charge contributing to the charge transport depends on the threshold voltage $V_{g,th}$ and thus equation 2.4 becomes

$$p(V_g) = \frac{C_{ox}}{e} (V_g - V_{g,th}) \tag{2.5}$$

The threshold voltage $V_{g,th}$ can be modified by doping to induce additional charge carriers in the channel, which will result in a shift of $V_{g,th}$. This shift $\Delta V_{g,th}$ is directly

related to the doping induced charge carriers p_{doping} by

$$p_{\text{doping}} = \frac{C_{ox}}{e}\Delta V_{g,th} \tag{2.6}$$

For more details see Refs. [11, 12, 55]

2.1.2 Contact resistance

Contact resistance in organic TFTs is often quite large and can even, especially for short channel devices, dominate over the channel resistance. It is thus interesting and relevant to determine the contact resistance of TFT devices. This can be done by applying the so called transmission line method (TLM) [19, 56–59]. For this the total device resistance $R_{tot} = \partial V_{ds}/\partial I_{ds}$ of series of TFTs with different channel length is measured. The total device resistance is the sum of the channel resistance R_{ch} and the contact resistance R_c.

$$R_{tot} = \frac{\partial V_{ds}}{\partial I_{ds}} = R_c + R_{ch}(L) \tag{2.7}$$

In the linear regime, the channel resistance R_{ch} is proportional to the channel length L, see equation 2.1, and equation 2.7 can thus be expressed as

$$R_{tot} = \frac{\partial V_{ds}}{\partial I_{ds}} = R_c + \frac{L}{WC_{ox}\mu(V_g - V_{g,th})} \tag{2.8}$$

The contact resistance is evaluated by extrapolating the total resistance R_{tot} to zero channel length ($L = 0$)

$$R_c = R_{tot}(L = 0) \tag{2.9}$$

Further, equation 2.8 allows for the evaluation of the contact free mobility μ_{cf} by

$$\mu_{cf} = \frac{1}{WC_{ox}}\frac{\partial}{\partial V_g}\left(\frac{\partial R_{tot}}{\partial L}\right)^{-1} \tag{2.10}$$

2.2 Organic thin film transistor fabrication

This section first describes the fabrication of the organic TFTs, including a description of the vacuum chamber where both the organic semiconductor *i.e.* pentacene and the dopant molecules are evaporated and where the electrical measurements are performed. In a second part, the methods used for the characterisation of the film morphology are presented.

2.2.1 Vacuum chamber for deposition and *in-situ* measurement

The organic TFTs are produced by evaporating the organic semiconductor material on top of pre-patterned TFT template chips and are subsequently electrically characterized. Organic semiconductor deposition, doping as well as the electrical characterization are performed in the same ultra high vacuum (UHV) system without breaking the vacuum. The UHV system enables us to study the doping of organic TFT with channel thickness of only a few ML. Exposure of pentacene TFT to air leads to an increase of the charge carrier concentration while reducing the mobility [49], thus the UHV strongly reduces such unintentional doping effects.

The chamber (see Figure 2.1) consists of two parts, a load lock, where the sample is introduced into the system and temporarily stored, and the main chamber, where the deposition of the molecules is performed. The load lock was in a first stage open to the main chamber, so that the complete chamber had to be vented for sample loading (Figure 2.2) and has been later complemented by a gate valve, such that only the load lock has now to be vented (Figure 2.3). The sample is placed in a chip holder at the end of a linear feedthrough, which allows to move the sample from the load-lock into the main chamber for the deposition of either pentacene or the dopant molecules, while the default sample position is in the load lock, hidden from the molecular evaporators. The chip holder, and thus the sample, is connected with an electrical feedthrough enabling the *in-situ* electrical characterization of the 2×14 TFTs on one chip. The deposition is performed by physical vapor deposition (evaporation) in the main chamber, where up to four different organic materials can be evaporated. The molecules are filled into crucibles equipped with a resistive heating stage. Water cooling of the evaporators ensures that the operation of one evaporator does not heat the others in order to avoid the contamination of the to be deposited layer by a second compound. The different crucibles are separated by small aluminium walls to reduce cross-contamination of the different organic materials.

A water cooled quartz crystal microbalance is used to monitor the amount of molecules deposited. The calibration is performed by measuring the film thickness by atomic force microscopy. The evaporation rate of the organic materials was adjusted for values between 0.02 ML/min and 0.5 ML/min. The sample is kept at room temperature during evaporation.

After each refill of an evaporator, for which the main chamber has to be vented, a bake-out cycle is performed first. Then the molecules are carefully degassed at a very low evaporation rate to remove low molecular weight impurities. The base pressure of the chamber was below 2.5×10^{-9} mbar after bake-out. After sample loading it raised to a higher value of the order of $(4-6) \times 10^{-8}$ mbar without and below 2×10^{-8} mbar with load-lock gate. The load-lock chamber, separated by a gate, is first pumped with a

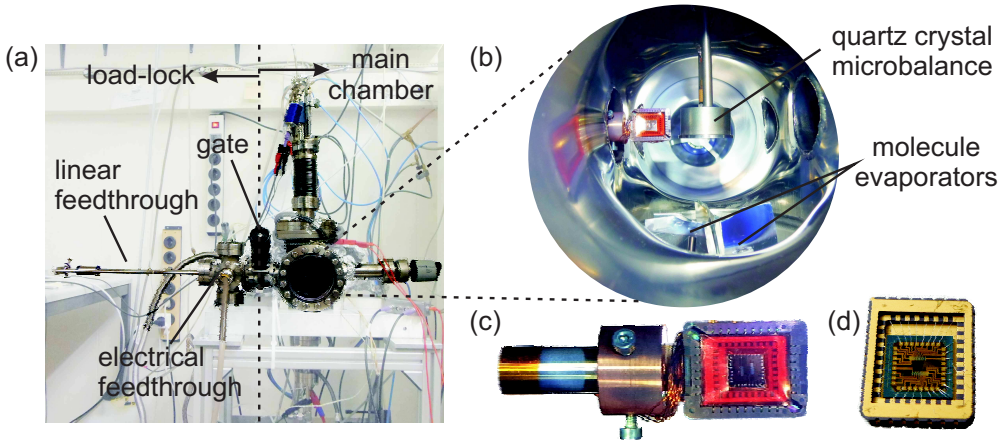

Figure 2.1: (a) Vacuum chamber with the load-lock on the left, separated from the main chamber on the right by the gate valve. (b) Evaporation chamber with the molecule evaporators on the bottom. In the center the quartz crystal microbalance and the sample can be seen. (c) Sample on the linear feed through with the Kapton cover (red colour). (d) Bonded sample.

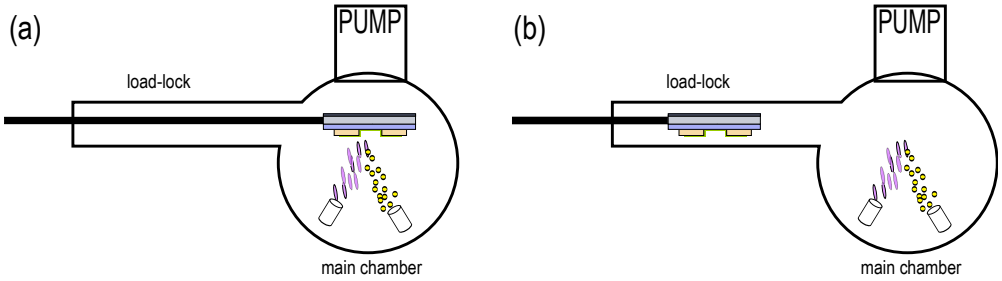

Figure 2.2: Schematic drawing of the UHV system with the load-lock open to the main chamber. (a) Position of sample during molecule deposition. (b) Storage position of the sample.

prevacuum membrane pump to $\sim 1\times10^{-1}$ mbar before slowly opening the load-lock gate to the main chamber. The pressure in the main chamber does not exceed 1×10^{-4} mbar during this process.

2.2.2 Sample layout and fabrication

There are four main different TFT layouts; bottom or top gate in combination with bottom or top source and drain contacts. The TFT layout used in this thesis is a bottom gate, bottom contact device as illustrated in Fig. 2.4. The TFTs are fabricated on highly p-doped silicon substrates equipped with a 150 nm thermal oxide layer on top and a back-side metallation consisting of 250 nm Al and 50 nm Ti capping layer, serving as the gate electrode. The source and drain electrodes consist of 100 nm Au with 10 nm Ti as a sticking layer between the Au and the SiO_2 (see also Appendix C for the detailed process steps). On one chip 2×14 transistors are fabricated with a channel length L, *i.e.* the distance between the source and gate electrode, between 5 μm and 200 μm (Fig. 2.5(a)). The device active organic semiconductor material, *i.e.* the pentacene, is

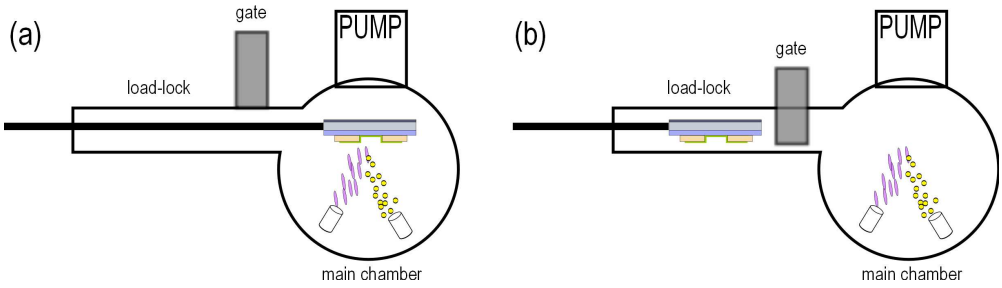

Figure 2.3: Schematic drawing of the UHV system with a gate valve between main chamber and load-lock. (a) Position of sample during molecule deposition and with the gate open. (b) Storage position of the sample with the gate almost closed to act as shutter.

evaporated at a later stage on top of the patterned silicon substrates equipped with the gold electrodes. When the organic semiconductor is evaporated on the chip, a double layer resist, serving as a mask, ensures the electrical isolation of the different TFTs on the same chip and at the same time defines the channel width W of 400 μm (see Fig. 2.5).

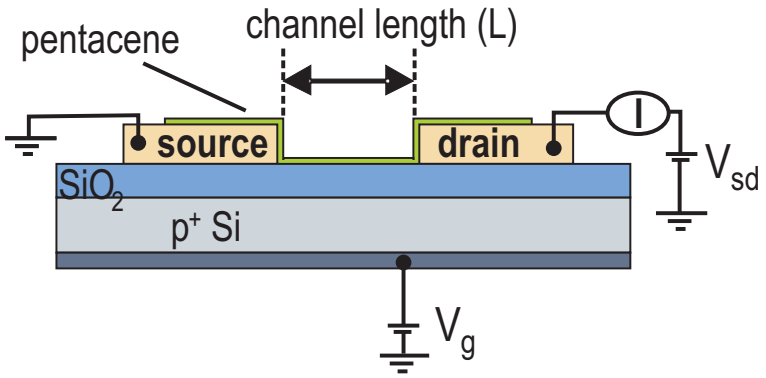

Figure 2.4: Schematic drawing of the thin film transistor device structure used in this thesis.

Before the organic semiconductor is deposited on the TFT template, an O_2-plasma is applied to clean the surface, e.g. to remove organic residues. The O_2-plasma cleaning is performed in Oxford RIE 80+ with an O_2 flow of 10 sccm, a pressure of 100 mtorr and 100 W plasma power applied for 60 seconds. After the O_2-plasma cleaning the sample chip is glued into a chip carrier with a conductive epoxy and bonded by an aluminium wedge bonder (see Figure 2.1(d)). Afterwards the sample is transferred to the vacuum chamber, where both the organic semiconductor and dopant evaporation, as well as the *in-situ* electrical measurements are performed. A Kapton cover is used to shadow the contacts of the chip carrier from the deposited molecules in order to avoid parasitic conductance (see Figure 2.1(c)). The transfer time is minimized to achieve good organic semiconductor film growth which is essential to obtain good electrical TFT characteristics. Otherwise island growth is observed and/or low or no conductance is measured. After sample loading, the chamber is pumped over night to reach the base

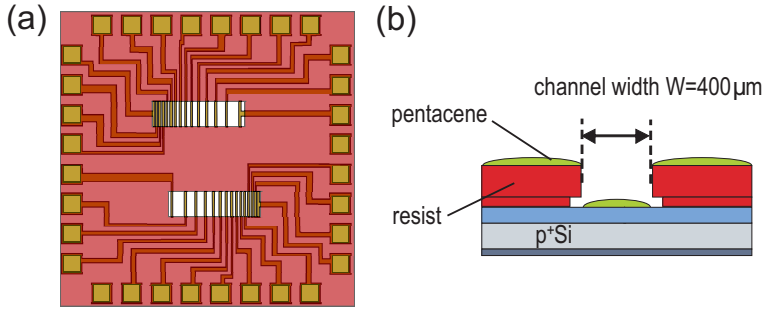

Figure 2.5: (a) Layout of one chip with 2×14 TFTs with channel lengths between 5 μm and 200 μm and the resist mask (red) is seen, (b) cross section showing the double layer resist mask defining the channel width.

pressure before both the deposition of the molecules and the electrical measurements are performed on the next day.

We fabricated also TFT samples with MoO_x electrodes by replacing the Ti/Au electrode material by Mo. The oxidation of the Mo electrodes to MoO_x occurs during the O_2-plasma cleaning (see Refs. [60, 61]). The sample preparation remained otherwise the same as described above for the TFTs equipped with Au contacts. X-ray photoelectron spectroscopy confirmed that the O_2-plasma oxidizes the Mo as can be seen in Figure 2.6. Whereas before O_2-plasma the Mo film consists mostly of metallic Mo with contributions of MoO_2 and MoO_3, after the O_2-plasma treatment the main contribution comes from the MoO_3 (see also Table 2.1). Using a simple substrate-overlayer model [62] and a mean free path of 2.1 nm, the thickness of the MoO_3 film is estimated to about 3.5 nm.

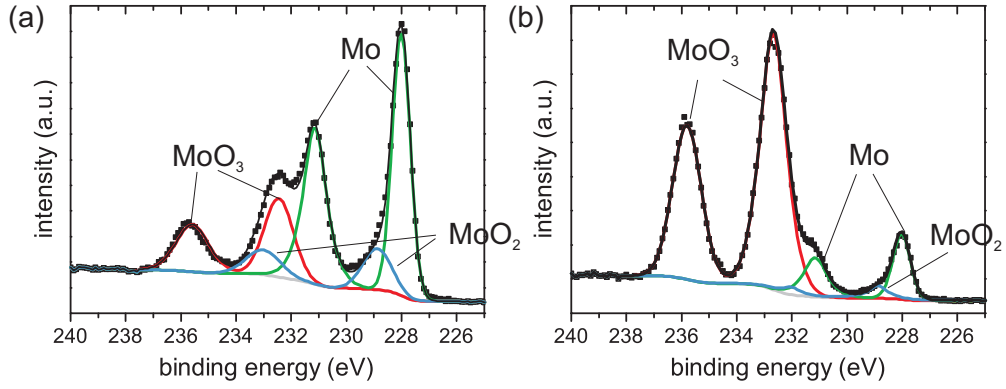

Figure 2.6: Mo3d XP spectra of the sputter deposited Mo film (a) before and (b) after the O_2-plasma. The green curve shows the contribution of the metallic Mo, the blue curve the one of MoO_2 and the red curve the contribution of MoO_3. The black line is the sum of the different contributions.

Samples showing a large positive threshold voltage in the pristine state have been excluded from further experiments. Contamination of the pentacene with one of the studied dopant molecules F_4TCNQ can lead to unintentional doping in some occasions. This may lead to the large threshold voltages observed for some of our samples.

	Before O_2-plasma	After O_2-plasma
Mo - metallic	∼60 %	∼15 %
MoO_2	∼14 %	∼ 4 %
MoO_3	∼26 %	∼81 %

Table 2.1: Relative concentrations of metallic Mo, MoO_2 and MoO_3 in sputter deposited Mo film before and after the O_2-plasma as measured by XPS.

2.2.3 Characterization of film morphology

After all measurements on one sample have been performed, the samples are removed from the UHV system to investigate the film morphology both by scanning electron microscopy (SEM) and by atomic force microscopy (AFM). SEM gives a nice overview of the sample morphology: islands of pentacene on the electrode and on SiO_2 are well recognized as well as the local variation of film thickness is visualized. In order to achieve a good contrast a low acceleration voltage of 1 keV was used: a low acceleration voltage reduces charging of the sample (especially on SiO_2) and gives good surface contrast for our only few monolayer thick pentacene films. The in-lense detector of the SEM and a working distance between 2 and 3 mm were used. Tapping-mode AFM is used both to calibrate the quartz crystal microbalance, by measuring the average pentacene thickness for a series of samples, and for a more detailed analysis of the morphology and the local, absolute thickness. SEM, on one hand, gives a good overview of the homogeneity of the pentacene films both on the electrodes and on the SiO_2 as well as at the edge of the electrodes. However, it does not provide information about the local and absolute thickness of the film as only relative changes in the thickness can be observed. AFM, on the other hand, reveals good information about the local thickness but is limited in the resolution of the morphology at the edge of the electrodes due to the surface roughness and large thickness of 100 nm of the electrodes compared to the pentacene ML thickness of 1.5 nm. The complementary combination of SEM and AFM gives thus a good understanding of the film morphology.

2.2.4 Photoelectron spectroscopy

Complementary to the charge transport measurements, X-ray photoelectron spectroscopy (XPS) and UV-photoelectron spectroscopy (UPS) experiments were undertaken for pentacene films deposited on Au(111) single-crystal substrates with pentacene thickness comparable to the 2.5 ML on SiO_2. The Au(111) substrate was chosen to provide a conducting support for the pentacene film. In photoelectron spectroscopy the kinetic energy E_{kin} of excited photoelectrons (photoelectric effect [63, 64]) is measured. The binding energy E_B of the electron, referenced to the Fermi

level E_F, can be calculated from the kinetic energy by

$$E_B = h\nu - E_{kin} - \phi_{sp} \tag{2.11}$$

where $h\nu$ – the energy of the photon, and
ϕ_{sp} – the work function of the spectrometer.

XP spectra are measured using monochromatized X-rays from an Al anode ($h\nu =$ 1486.7 eV) giving a full width half-maximum of 0.8 eV. XPS measures the binding energy of the core levels which depends primarily on the specific element but also on its chemical environment which gives rise to chemical shifts ΔE_B.[62]

UP spectra were acquired by electron excitation with UV-light with a photon energy of 21.218 eV (He I line). UPS provides information on the binding energy of the valence electrons but also on the sample work function. A sample bias of ~ -9 V was applied to observe the secondary electron cut-off.

CHAPTER 3

Pentacene thin film growth and morphology

In this chapter the film morphology in pentacene TFTs is discussed. Both the morphology in the TFT channel as well as at the edge of the electrodes is investigated. The morphologies, obtained under modified evaporation conditions and for different electrode materials, are compared as well as their contact resistance and mobility. Further the evolution of the current during pentacene film growth is investigated: the occurrence of a saturation of the current (or its absence) can be observed and in the best case even completion of the monolayers can be detected.

3.1 Pentacene - background

Amongst a large variety of both small molecules and polymers used for organic thin film transistors, pentacene, a small molecule (see Figure 3.1), is often considered as a model organic semiconductor [8, 50]. Pentacene is generally used as a p-type semiconductor for which large hole mobilities up to 35 cm^2/Vs for single crystals [13] and up to 3 cm^2/Vs for thin films [51] could be achieved. See the review of J.E. Anthony [65].

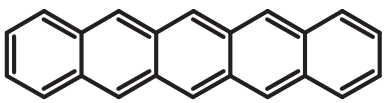

Pentacene

Figure 3.1: Illustration of the chemical structure of pentacene.

Pentacene is known to grow in the so called thin film phase on oxide and organic surfaces. In this thin-film phase the pentacene molecules are stacking on the substrate in an upright position, standing almost perpendicular to the substrate (see Figure 3.2). The height of one monolayer therefore corresponds to about 1.55 nm. [66–70] On metal

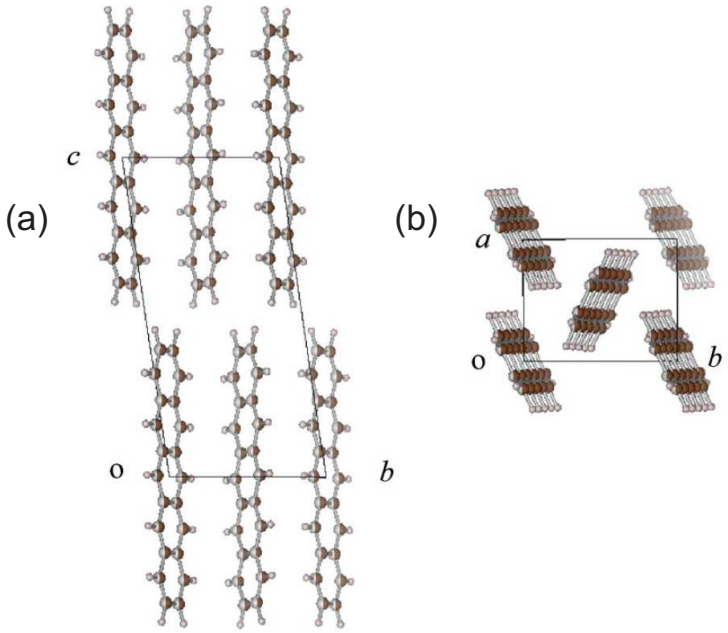

Figure 3.2: Illustration of the thin film phase of pentacene. (a) presents the upright position of the pentacene molecules and the relative stacking of subsequent layers. (b) shows the molecular ordering within one monolayer. Reprinted with permission from *Appl. Phys. Lett.*, **90**, 181930 (2007) [70]. Copyright 2007, AIP Publishing LLC.

surfaces, such as Au(111), the pentacene grows different than on the oxide surfaces; here the pentacene molecules lie flat on the substrate with their long axis parallel to the surface [71, 72]. On polycrystalline Au only the first monolayer of pentacene molecules seem to lie flat on the substrate (wetting layer) and for higher monolayer the molecules are nearly standing upright [73].

3.2 Pentacene morphology

The morphology of the pentacene films was characterized both by SEM and by AFM (see section 2.2.3). Film edges obtained through shadowing from the bond wires are used to calibrate the film thickness by AFM. Figure 3.3 shows a SEM micrograph of such an edge both for a sample equipped with Au contacts and a channel thickness of 1.5 ML and for a sample equipped with MoO_x electrodes and a channel thickness of 2.5 ML. The image has been taken on a spot outside the bond pads, next to the edge of the sample which is again uncovered by the resist. The spot is thus situated just above of

the position of the contact patterns as they are illustrated in Figure 2.5. The uncovered substrate can be seen on the left side of the image. Here no pentacene was deposited due to the bond wire which served as a shadow mask. The SiO_2 surface is situated at the top of the figures and the metal surface at the bottom. The film thickness gradually increases from left to right from 0 ML to 1.5 ML and 2.5 ML respectively. Especially in Figure 3.3(b) the increase from 0 ML to 1 ML and 2 MLs and finally the on-set of the third monolayer can be observed, visible as layers with increasingly darker shades of grey. It can be observed that the film morphology on Au differs from the morphology observed on SiO_2. On MoO_x patterns, the observed morphology is comparable on the electrode and on the SiO_2 (See discussion below in section 3.2.2).

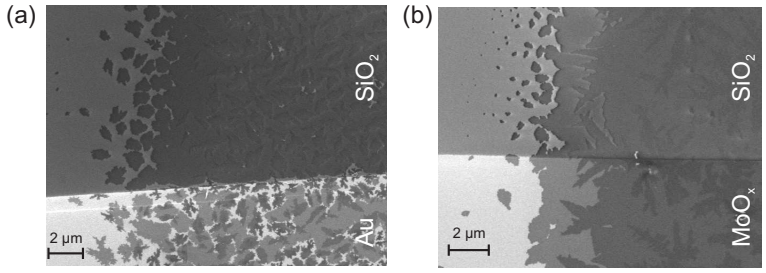

Figure 3.3: Edge of pentacene film caused by shadowing from the bond wires. The pentacene grows at the top of both images on SiO_2 and at the bottom of both images on the electrode material consisting of (a) Au and (b) MoO_x, respectively. On the left side the uncovered substrate can be seen. The film thickness gradually increases in each image from left to right, from 0 ML to (a) 1.5 ML and to (b) 2.5 ML, respectively. Different morphology of the pentacene film on Au and on SiO_2 can also be observed.

In Figure 3.4 AFM micrographs of the edge of pentacene films grown on SiO_2 are presented for devices with a channel thickness of 2.5 ML, both on a sample with Au and one with MoO_x electrodes. The uncovered SiO_2 can be again observed on the left and the pentacene thickness increases gradually from 0 ML at the left to 2.5 ML at the right of the imaged frame. The line-profiles taken along the blue line show the monolayer steps. The height of the monolayer corresponds roughly to 1.5 nm which is in agreement with the thin film phase [66]. The thickness calibration was performed from such AFM figures by measuring the average thickness at the right part of the figure, where the film thickness is highest. The uncovered SiO_2 surface serves as a reference corresponding to 0 ML pentacene coverage. The average thickness is divided by 1.5 nm to get the number of monolayers. The final calibration is averaged from a series of samples with different channel thickness. Note that this method might lead to an underestimation of the effective channel thickness if the pentacene thickness at the edge of the sample is slightly lower than in the center.

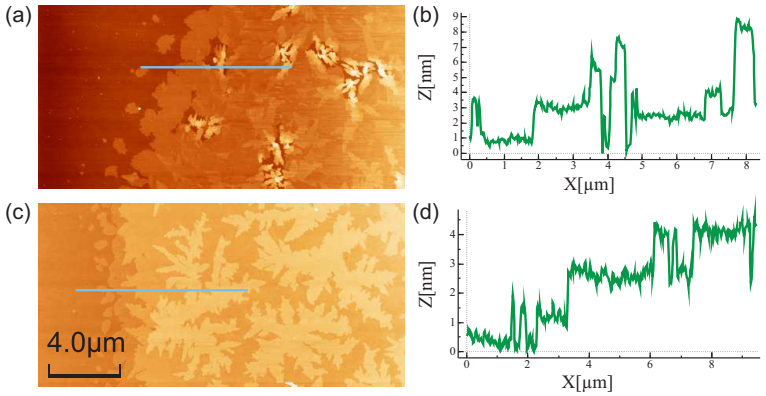

Figure 3.4: (a) and (c): Edge of pentacene film on SiO_2 caused by shadowing from the bond wires. On the left hand side the uncovered substrate can be seen. The film thickness gradually increases from the left to the right from 0 ML to 2.5 ML. (b) and (d) show the profile along the blue line in figures (a) and (c) respectively. The monolayer steps can be well recognized; one monolayer step height corresponds to ~ 1.5 nm.

3.2.1 Pentacene growth in the channel

Figure 3.5 shows AFM figures of pentacene films grown on SiO_2, *i.e.* in the TFT channel, with the thickness between 0.8 ML and 10 ML and for films showing different film morphologies. The *rough films* correspond to the first series of pentacene TFTs (used for the studies in Chapter 4). It can be observed that the pentacene islands are relatively small and that, even for thin films such as the 2.5 ML film, pentacene grows in an island growth mode instead of a layer-by-layer growth mode. Those films show therefore a relatively large film roughness, which also implies that the 5 ML and 10 ML films have regions where the local thickness is below 2 ML or where even the SiO_2 surface remains uncovered. This can be best seen in Figure 3.6 which shows a smaller scale AFM image as well as SEM images of those rough films. The bright spots in the SEM images are associated to patches of the uncovered SiO_2 surface (compare also to Figure 3.3). Even though those films showed nice TFT characteristics (see also Chapter 4), the large film roughness will render the interpretation difficult when studying the relation of surface doping efficiency and channel thickness (see Chapter 6). For such studies the film morphology should be improved to achieve a more uniform layer structure.

As can be seen in Figure 3.5 for the *flat films* such an improvement of the film morphology has been achieved; by changing the deposition parameters, layer-by-layer growth is observed up to a pentacene thickness of 2 ML. To improve the thin film morphology, we modified the pentacene deposition chamber used in the previous experiments [26, 27] and the preparation of the *rough films* (see Figure 2.2) by introducing a load-lock gate between the sample load-lock chamber and the main evaporation chamber (see Figure 2.3). This way, we were able to minimize the exposure of the, previously degassed, pentacene and dopant molecules to ambient air during sample

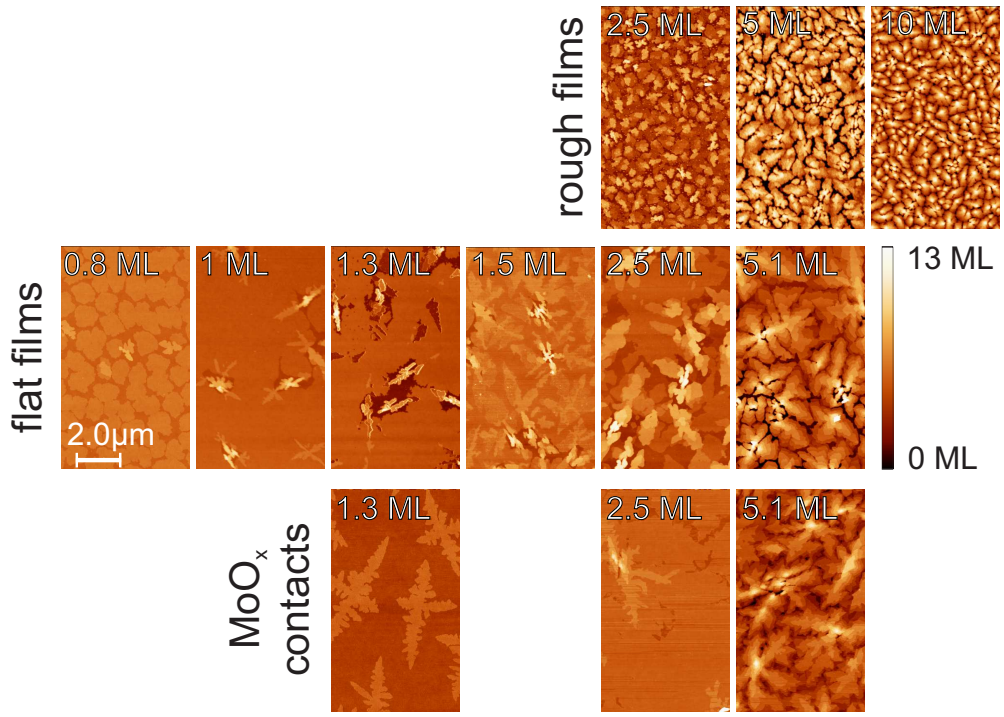

Figure 3.5: AFM micrographs of pentacene films on SiO_2 with different thickness. The *rough films* from TFTs with Au contacts show small islands. The average observed island size is much larger for the *flat films* from TFTs with Au contacts and the pentacene films from TFTs with MoO_x contacts. The film growth mode of the *rough films* is island-like whereas the *flat films* and the films grown on the devices with *MoO_x contacts* grow in a layer by layer mode for coverages below 2 ML and 3 ML respectively. At higher coverages the growth mode changes to dendritic.

loading. The maximum pressure in the main chamber just after sample loading was below 1×10^{-4} mbar. We also reduced the background pressure to below 2×10^{-8} mbar after loading the TFT-template chips. This pressure is a factor of ~ 3 lower than in the previous system without load-lock gate. The evaporation rate of pentacene was also reduced to a rate of $0.05 - 0.09$ ML/min, which is a factor of ~ 5 slower than the rate used for the *rough films*.

We consider that the improved film morphology is a consequence of the increased surface migration length of the pentacene molecules on the device surface, due to the deposition at a low deposition rate [74–77] assisted by the slightly reduced background pressure. Also the molecules might be cleaner as they are not exposed to air with every use of the load-lock *e.g.* to load a sample. This could lead to an overall cleaner source – similar to an improved outgasing procedure for the pentacene source and thereby also influence the pentacene film morphology. Other factors which influence the film morphology, such as the substrate temperature [68, 74, 75, 78, 79], the surface properties of the dielectrics [80–83] and the gas ambience conditions [84], have been also reported in literature, suggesting that further improvement of the film morphology is possible.

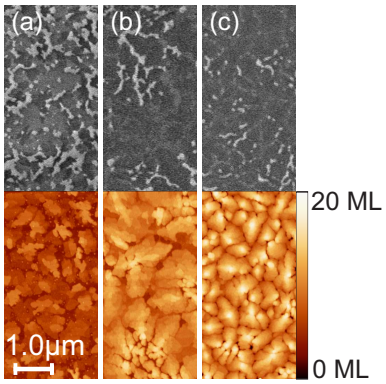

Figure 3.6: SEM (top) and AFM (bottom) data for (a) 2.5 ML, (b) 5 ML, and (c) 10 ML thick pentacene on SiO_2.

If we have a closer look at the *flat films* in Figure 3.5, we see that the 0.8 ML-thick film shows partly connected islands exhibiting a height of 1.5 nm, corresponding to the 1 ML step height of pentacene molecules aligned in upright direction perpendicular to the substrate (thin film phase [66]). The homogeneity of the film manifests itself in the small proportion of second layer pentacene islands observed for the 0.8 ML and 1 ML-thick films. The 0.8 ML-film did not (yet) form a complete first monolayer. We observed, however, a clear TFT characteristic for this film (see Chapter 6) which indicates that this thickness is above the percolation limit. For the film with the average thickness of 1 ML, a homogeneous pentacene monolayer is observed. The 1.5 ML-thick film shows that about one half of the surface was covered by the second monolayer. Three and higher monolayer coverages are also observed, mostly aggregated at defects centers, but they cover only a small percentage ($\sim$ 6%) of the surface area. Defect centers are generally characterized by island consisting of the local stacking of several monolayers surrounded by depressions where the SiO_2 locally remains uncovered (seen best in Figure 3.5 for the 1 ML of the *flat films*). For pentacene films of 2.3 ML thickness and above, dendritic growth is observed in agreement with literature reports [85]. We thus observe a layer-by-layer growth up to 2 ML thick films.

To quantify the film morphology, we evaluated the RMS surface roughness and the lateral correlation length for these films (*flat films*), and the differently produced *rough films*, using the software WSxM [86] (see Figure 3.7). The spatial correlation length is equal to $\sqrt{2}$ times the standard deviation obtained from a Gaussian fit to the auto-correlation function along the scan direction. The improved morphology of the *flat films* is evident from the reduced roughness by a factor of $2-5$ in comparison to the *rough films*. The lateral correlation length also increased for the *flat films* by a factor of $2.5-3.5$.

The samples with MoO_x contacts (see in Figure 3.5) are fabricated under the same conditions as the *flat films*, *i.e.* the same low evaporation rate, in the modified chamber

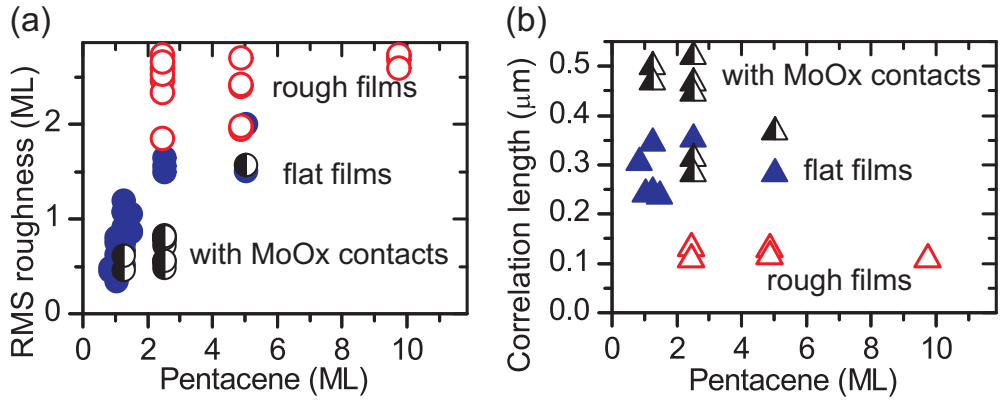

Figure 3.7: Comparison of the RMS roughness and the lateral correlation length of the *rough films* (red open symbols), *flat films* (blue filled symbols) and those with MoO_x contacts (black half-filled symbols).

with load-lock gate and at the same pressure. The 1.3 ML film shows a completed first ML film with roughly a third of the film covered with the second ML. The nominal 2.5 ML film shows almost completion of the third monolayer. The effective thickness is thus slightly larger than its nominal thickness of 2.5 ML. We thus observe layer-by-layer growth almost up to the completion of the third monolayer. For thicker films as the 5.1 ML film, dendritic growth is again observed as for the *flat films*. The 5.1 ML thick film showed a large threshold voltage (probably due to unintentional doping) and is thus not considered for performing doping experiments. However the film morphology is likely not affected by this unintentional doping. The RMS roughness (see Figure 3.7(a)) for the 1.3 ML and the 5.1 ML films is comparable to the *flat films*. The RMS roughness of the 2.5 ML film is lower, which could be direct consequence of the still observed layer-by-layer growth for the samples with MoO_x contacts whereas for the *flat film* dendritic growth starts at ~ 2 ML. The correlation length of the samples with MoO_x contacts is comparable or slightly larger than the *thin films* (see Figure 3.7(b))

3.2.2 Contact region

Not only the morphology in the TFT channel is important but also the morphology at the edges of the electrodes. For good electrical contact between the electrodes and the pentacene channel a good coverage of the electrode edge should be achieved. Figure 3.8 shows AFM figures of the contact region from the different films described in the previous section. Due to the relatively large thickness of the electrodes compared to the thickness of one ML of pentacene, the detailed structure of the pentacene film at the edge of the contacts is sometimes hard to see. The AFM images are thus complemented by SEM micrographs (Figure 3.9).

It can be seen in Figures 3.8 and 3.9 that the film morphology in pentacene TFTs

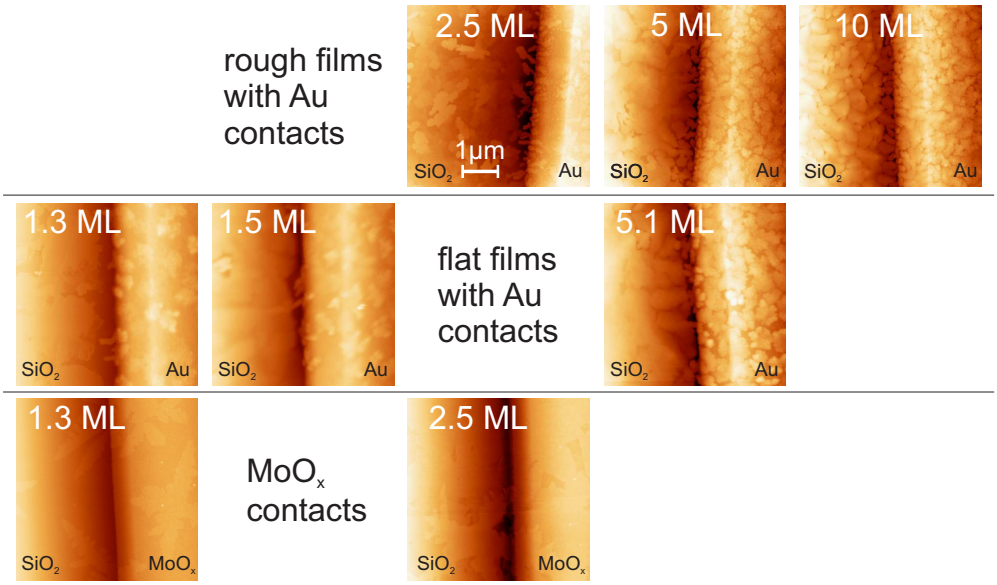

Figure 3.8: AFM micrographs of the pentacene coverage at the electrode edge for Au and MoO_x contacts and different channel thickness. The channel with the SiO_2 is situated on the left and the electrode on the right side.

with Au contacts is discontinuous at the electrode edge. This applied both for the *rough films* as well as for the *flat films*, even though the morphology in the channel was substantially different (see section 3.2.1). The contact between the electrode and the channel seems only to be achieved through small, elongated pentacene islands which stretch across the electrode edge. It can also be observed that the morphology in the channel differs from the morphology on the Au electrodes. This is best seen for the *flat films* where the pentacene forms a continuous film in the channel whereas on the electrode only partially connected islands are formed. This difference in the film morphology is in agreement with the different growth mode on SiO_2 and on Au (see section 3.1). This difference in the film growth might also be the origin for the film discontinuity at the electrode edge. Different morphologies of the pentacene film in the channel and near the electrodes have also been observed by Kymissis *et al.* [87].

The morphology on MoO_x electrodes differs from the one on Au electrodes as can be seen in Figures 3.8 and 3.9. The morphology in the channel and on the MoO_x electrodes are comparable. The pentacene forms a continuous film both in the channel and on the electrodes as well as over the electrode edge. It can even be observed that pentacene islands grow across the electrode edge. This is best illustrated in Figure 3.9 for the 1.3 ML film where a pentacene island, forming the beginning of the second monolayer, grows continuously across the electrode edge. The layer-by-layer growth continues thus from the channel to the electrode. This observation can be understood by the fact that pentacene grows on MoO_x in the thin film phase [61] in the same way as observed on SiO_2. This implies that the crystal structure of pentacene is the same in the channel

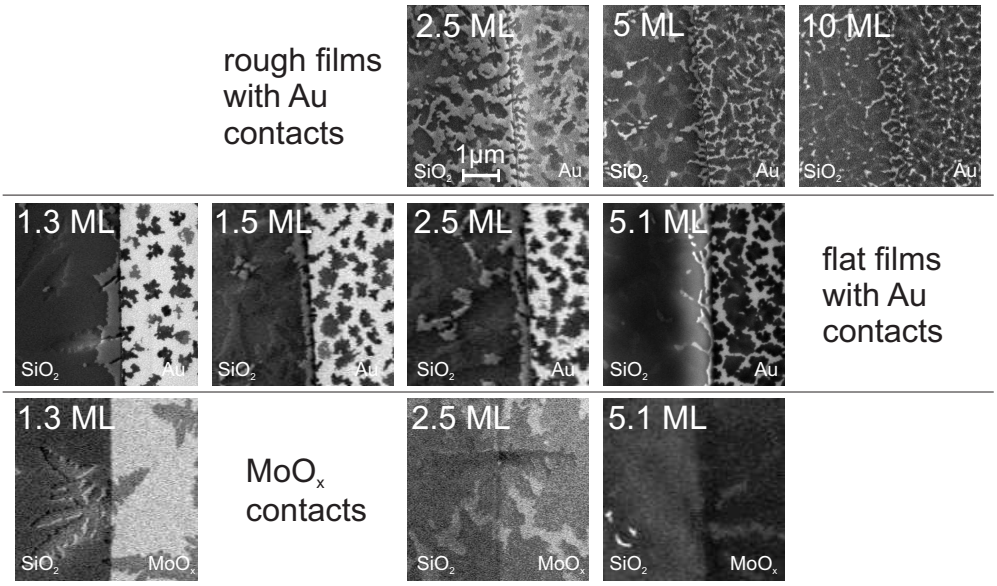

Figure 3.9: SEM micrographs of the pentacene coverage at the electrode edge for Au and MoO_x contacts and different channel thickness. The channel with the SiO_2 is situated on the left and the electrode on the right side.

and on the MoO_x electrodes favoring the growth of continuous film even across the electrode edge.

3.2.3 Self assembled monolayer

As a parallel approach to obtain smooth pentacene films, the SiO_2 surface was surface treated by self assembled monolayers (SAM). Such SAMs have been shown in the literature to improve the performance of pentacene TFT, *e.g.* by increasing the mobility [88–91]. Such SAM can be formed either by dip-coating, where the sample is immersed in a solution containing the respective molecule for the SAM, or by vapor deposition. A widely used SAM in conjunction with pentacene TFT is octadecyltrichlorosilane (OTS), for which increased mobilities in pentacene TFTs were observed [81, 83, 90–92]. We deposited OTS on TFT template chips by dip-coating of OTS *i.e.* by immersing the sample for ∼1 hour in a 2%-solution of OTS in toluene. Afterwards the sample was rinsed with toluene to remove excess OTS and transferred to the vacuum chamber for the pentacene deposition. Even if this process was successfully applied for pentacene TFT in literature [32, 83], the pentacene grew in islands and non-uniformly, probably due to a non-uniform SAM-film, as can be seen in Fig. 3.10. This method did thus not provide conductive films in the thickness range of a few monolayer which provides the focus of the present studies.

Another batch of samples were covered with SAM by the vapor deposition technique. We selected a mixture of fluorinated mono- and trichlorosilanes

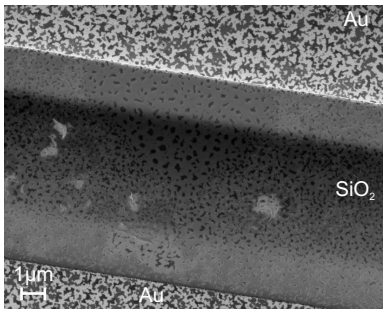

Figure 3.10: SEM image of a 1.3 ML pentacene film grown on SiO_2 surface treated with OTS. The SAM was formed immersing the SiO_2 surface to a 2%-solution of OTS in toluene for ∼1 hour.

((Tridecafluoro-1,1,2,2-tetrahydrooctyl)-dimethylchlorosilane and trichloro(1H,1H, 2H,2H-perfluorooctyl)silane), which has been used in the lab as dense antiadhesive coating for nanoimprinting [93]. The SAM was applied by inducing 5 μl of a 1:1-mixture of the two silanes into the exposure chamber which has previously been pumped by a membrane pump. Figure 3.11 shows AFM and SEM images of a 1.3 ML pentacene film grown on the modified SiO_2 surface. Even though the pentacene grows in small elongated islands leaving part of the SiO_2 surface uncovered, the pentacene films deposited on top of these SAM layers are conductive. However large threshold voltages > 50 V have been measured in the TFT setup. These large threshold voltages could be caused by a charge transfer between the fluorinated silanes and pentacene. Such a charge transfer has been observed between rubrene and the fluorinated monochlorosilane [94]. Large threshold voltages combined with a possible doping effect are not suitable for the doping experiments studied in this thesis. We

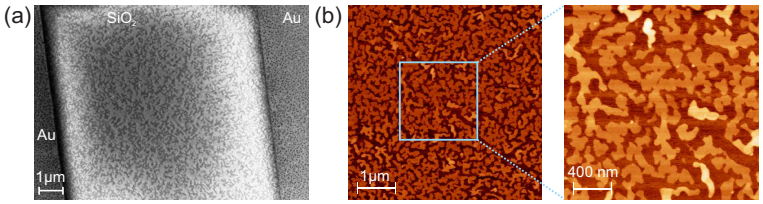

Figure 3.11: (a) SEM and (b) AFM image of a 1.3 ML pentacene film grown on SiO_2 surface treated with a mixture of mono- and trichlorosilane. The SAM was formed by vapor deposition.

therefore applied the vapor deposition with OTS. For this the sample has been placed in a round-bottom flask which is subsequently pumped with a simple prevacuum pump. After evacuation of this flask the pump is disconnected and 5 μl of OTS is introduced in the flask with a syringe. After $\sim$ 10 minutes the vapor deposition is stopped by evacuating the flask again. Figure 3.12 shows SEM and AFM images of four conductive samples with 1.3 ML of pentacene grown on SiO_2 with an OTS film. The pentacene grows in islands and in the best case a continuous first monolayer was

observed. The island size seems generally smaller than what was observed for the *flat films* (see Fig. 3.5). Such smaller islands of pentacene on SiO_2 with OTS compared to clean SiO_2 has also been observed in literature [83, 90]. The TFT performances were comparable to the TFTs without OTS treatment and the morphology of the *flat films* is comparable or better to those on SiO_2 modified by OTS. Therefore pentacene TFTs with OTS treatment were not further studied in this thesis.

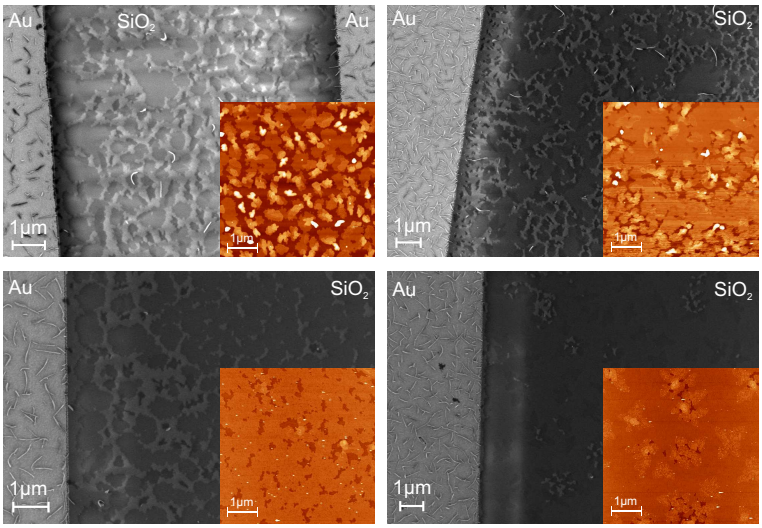

Figure 3.12: SEM and AFM image (inset) of four samples with a 1.3 ML pentacene film grown on SiO_2 surface treated with OTS. The SAM was formed by vapor deposition.

3.3 Source-drain current for increasing pentacene thickness

During pentacene film deposition we measured the drain-source current I_{ds} for the drain-source bias V_{ds} of -1 V and the gate-source bias V_g of either -5 V or -20 V and for the TFT with a channel length of 150 μm. Figures 3.14(a) and (c) show the relation between I_{ds} and the channel thickness for TFTs with MoO_x electrodes. The final channel thickness were 2.5 ML and 5.1 ML and the evaporation rates were 0.04 Hz/min and 0.06 Hz/min respectively. The applied gate bias V_g was -20 V. Because of the formation of a continuous first monolayer, *i.e.* the first connected percolation path between drain and source electrodes, I_{ds} increased abruptly when the channel thickness reached ~0.7 ML. When the film thickness was further increased, I_{ds} increased gradually in agreement with the continuation of percolation in the first monolayer. At a nominal channel thickness of $\sim$ 0.9 ML an inflection point is observed where the slope of the increase of I_{ds} as a function of the channel thickness is suddenly reduced. We associate this effect to the completion of the first monolayer with an additional conductance channel opening via the second monolayer: The different monolayers can be considered

as independent channels for the charge transport, due to the more than two orders of magnitude lower coupling between the different monolayers with respect to the coupling between the molecules of the same monolayer [95]. These different coupling strengths for 'in-plane' and 'out-of-plane' directions have been observed in direction dependent mobility measurements. [96]. A similar inflection point like the one discussed above is observed at a channel thickness of $\sim$ 1.8 ML. The changing slope is best seen when looking at the derivative of I_{ds} versus the channel thickness θ. Here even a third inflection point can be observed at $\sim$ 2.6 ML. These values are close to the nominal thickness of 1 ML, 2 ML and 3 ML respectively. Beyond the inflection points I_{ds} increases further to reach saturation at around 5 MLs.

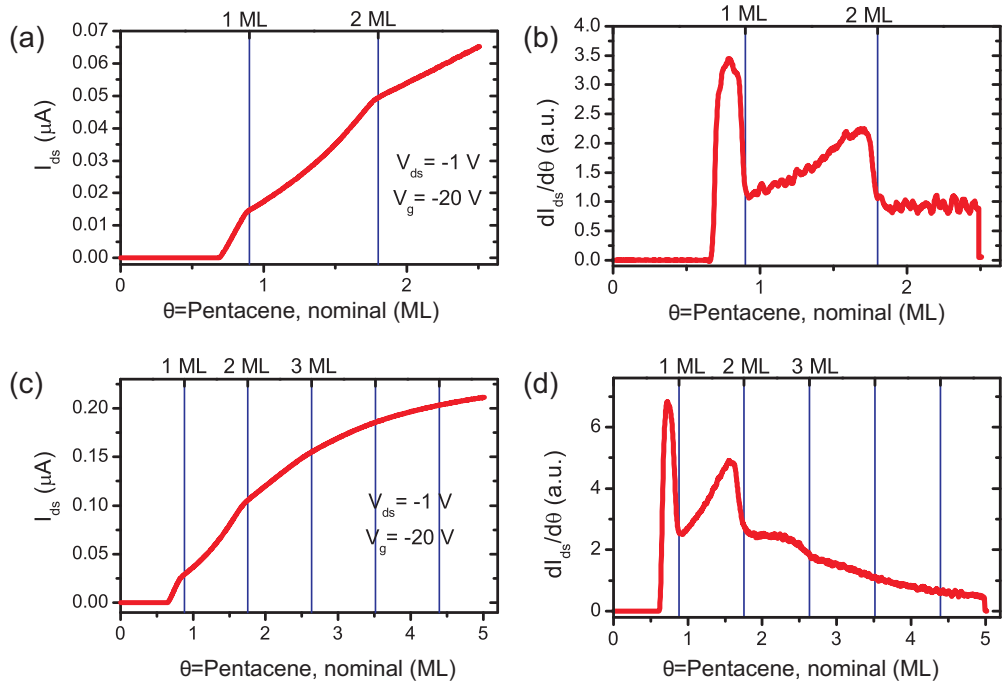

Figure 3.13: The source-drain current I_{ds} was measured during the pentacene evaporation on TFT with MoO_x contact with the final pentacene thickness of (a) 2.5 ML and (c) 5.1 ML respectively. The applied gate voltage V_g was -20 V and a source-drain voltage V_{ds} was -1 V. The top scale and the vertical lines indicate changes in the slope of I_{ds} as a function of pentacene thickness, which is best seen in the derivatives shown in figures (b) and (d).

Similar inflection points have been reported by Muck *et al.* in mobility measurements as function of the channel thickness for dihexylquaterthiophene (DH4T) TFTs where they observed two peaks at 1 ML and 2 ML respectively [97] and by Liscio *et al.* for N,N'-bis(n-octyl)-dicyanoperylene-3,4:9,10-bis(dicarboximide) (PDI8-CN2) TFTs where inflection points at $\sim$1 ML and $\sim$2 ML are observed for films exhibiting a layer-by-layer growth for a substrate temperature of 120°C [98]. If the threshold voltage remains constant during film evaporation the mobility and I_{ds} should be proportional (see equation 2.1). Shehu *et al.* [54] reported the variation of I_{ds} in pentacene TFTs

as function of the channel thickness and for different evaporation rates where they also observed peaks in the derivatives without however exhibiting the clear inflection points reported here. In comparison with these results, the observed layer-by-layer growth up to completion of the third ML of the pentacene film (see Figure 3.5) and the understanding of independent transport channels of the different monolayers as described above, we can associate the inflection points to completion of the respective first, second and third monolayer (indicated by the top scale in Figure 3.13). The discrepancy of the position of the inflection points and the nominal thickness by ∼10% could arise from errors in the thickness calibration by AFM which is performed at the edge of the sample.

The observed saturation of I_{ds} is in agreement with literature reports where saturation of the current in pentacene TFTs have been reported for channel thickness in the range of 2–7 MLs [52–54, 99]. It is understood that the current flows in the first few monolayers of the pentacene film next to the gate oxide interface and that thus the field induced charge carriers are confined within these few monolayers.

Figure 3.14 shows the evolution of I_{ds} of the TFTs with the *flat films* for increasing channel thickness and an applied gate voltage of -5 V. The onset of the current was observed at a channel thickness of ~ 0.8 ML. For those films, the first inflection point at ∼1 ML can still be relatively easy seen whereas the second at ∼2 ML can only be observed when looking at the derivative $\partial I_{ds}/\partial\theta$ (see top scale in Figure 3.14). Beyond the second monolayer no further inflection points were observed and the I_{ds} further increased. Saturation is not observed within the first 5 MLs. This could be issued by the reduction of the contact resistance with increasing channel thickness and thus increasing current (see Section 3.4.1) or partially by the lower applied gate voltage closer to the threshold voltage around 0 V where I_{ds} might not yet vary fully linearly with the applied gate voltage. A saturation of the contact free mobility could however be observed at a channel thickness of ~ 5 ML (see Section 3.4.2). The observation of the two inflection points are in agreement with the observation of the layer-by-layer growth up to the second monolayer (see Figure 3.5).

In Figure 3.15, we show the relation between the channel thickness and the drain-source current I_{ds} of TFTs with the *rough films* for the gate-source bias V_g of -5 V. I_{ds} increased abruptly when the channel thickness reached ∼1 ML. We can again observe two inflection points at 1.3 ML and at 2.6 ML. When the film thickness was further increased, I_{ds} increased gradually in agreement with the observation that contact resistance reduces for thicker films (see Section 3.4.1). The drain-source current saturated only beyond the shown first 5 MLs at around 9 ML.

The first and second inflection point could thus be observed for all films. It was always observed at regular spacing and for the *flat films* and the TFTs with MoO_x

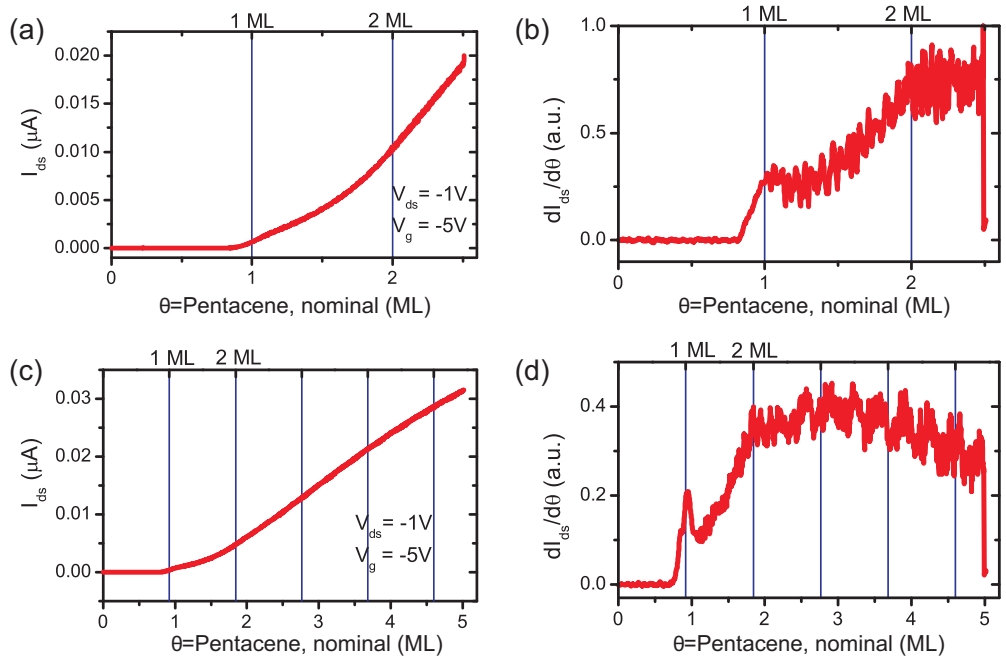

Figure 3.14: The source-drain current I_{ds} was measured during the pentacene evaporation on TFT with Au contact with the final pentacene thickness of (a) 2.5 ML and (c) 5.1 ML respectively corresponding to the *flat films*. The applied gate voltage V_g was -5 V and a source-drain voltage V_{ds} was -1 V. The vertical lines indicate changes in the slope of I_{ds} as a function of pentacene thickness, which is best seen in the derivatives shown in figures (b) and (d).

electrodes $\sim$ 10% below the nominal completion of a monolayer. For those films the onset of the current was at $0.7 - 0.8$ ML. The *rough films* show the onset of the current only at 1 ML and also the inflection points at 1.3 ML and at 2.6 ML are at larger values. This could be a direct consequence of the large film roughness which implies that more pentacene has to be deposited for the completion of one monolayer due to the island growth. Saturation of the current was only observed for the TFTs with MoO_x electrodes which also show the best morphology at the electrode edge. The non-saturation for the TFTs with Au electrodes could be a consequence of the non-continuous pentacene film at the electrode edge so that an increase of the average channel thickness also increases the contact area between pentacene channel and electrode and thus lowers the contact resistance which implies an increase of the current. The area under the peaks in the derivative $\partial I_{ds}/\partial\theta$ is proportional to the current flowing in the respective monolayer and therefore most of the charge transport occurs within the second monolayer in our TFTs. If the mobility is independent from the charge carrier density, $\partial I_{ds}/\partial\theta$ would scale as the charge density in the respective monolayer [54]. However, it was found that the mobility is related by a power law to the charge carrier density [100]. Therefore both mobility and charge carrier density vary for the different monolayers. The fact that most of the current flows in the second and not in the first monolayer can thus be explained either by a lower charge carrier density in the first monolayer, *i.e.* trapping might reduce the

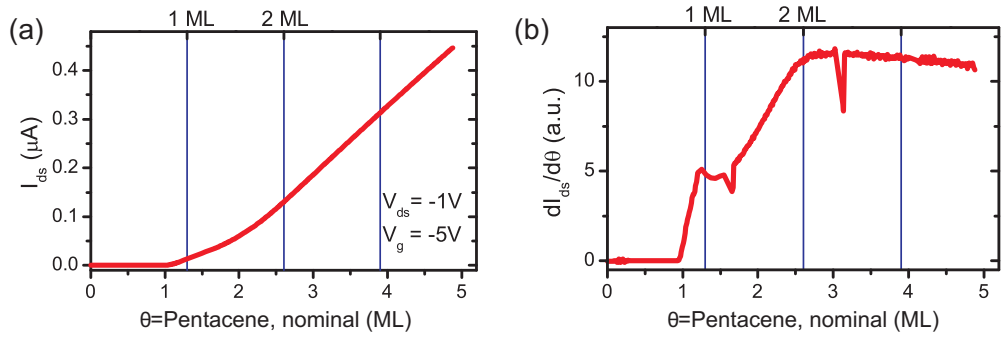

Figure 3.15: (a) The source-drain current I_{ds} was measured during the pentacene evaporation on TFT with Au contact with the final pentacene thickness of 2.5 ML corresponding to the *rough films*. The applied gate voltage V_g was -5 V and a source-drain voltage V_{ds} was -1 V. The vertical lines indicate changes in the slope of I_{ds} as a function of pentacene thickness, which is best seen in the derivative shown in figure (b).

free charge carrier density, or by a lower mobility in the first monolayer, *e.g.* induced by grain boundaries, or likely a combination of both effects.

3.4 Contact resistance and mobility for different films

In Section 3.2 we discussed the different morphologies both in the channel and on the electrode edges. In this section we compare the contact resistance and mobility of the pentacene TFT with different film morphology, *i.e.* the *rough films* and *flat films* with Au electrodes and the TFTs with MoO_x electrodes.

3.4.1 Contact resistance

The contact resistance was extracted with the transmission line method (TLM) described in Section 2.1.2. The total TFT resistance R_{tot} was measured as the inverse of the average slope of the *output curve* between $V_{ds} = -2$ V and $V_{ds} = 2$ V for an applied gate voltage V_g of -20 V. For better comparison of the data, the resistance has been calibrated to the channel width. Figure 3.16 shows the evolution of R_{tot} as function of the channel length for different channel thickness. It can be observed that R_{tot} varies quite linearly with the channel length and that with increasing channel thickness R_{tot} decreases. The fitting to R_{tot} was performed for channel length between 5 μm and 80 μm as indicated by the straight line. For comparison the fit is extended to larger channel length as a dashed line. R_{tot} of the 5 μm was often comparable or even slightly larger than R_{tot} for the 10 μm channel. It can be seen that R_{tot} is relatively large compared to the contact resistance R_c at $L = 0$ μm. The extracted R_c is thus subject to large variation depending on the fitting range which had to be chosen carefully in order to get non-negative R_c.

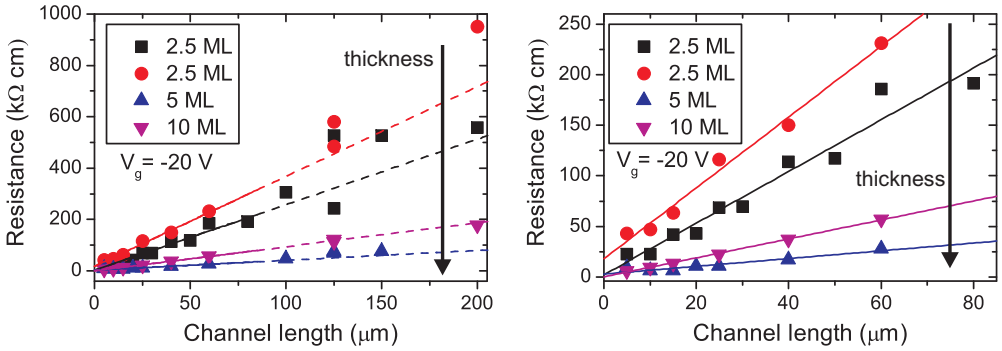

Figure 3.16: Total resistance R_{tot} as function of the channel length L for different channel thickness for the undoped *rough films*. Extrapolating R_{tot} to $L = 0$ gives the contact resistance R_c (see lines). A zoom-in for low L is shown on the right.

Figure 3.17 summarizes R_{tot} of the *flat films* for different channel length and channel thickness. For channel thickness between 1 ML and 2.5 ML, R_{tot} varies linearly with the channel length. For the 0.8 ML film a slower variation of R_{tot} with the channel length is observed for $L > 50$ μm compared to $L \leqslant 50$ μm. The opposite was observed for the 5.1 ML film where a large slope for $L > 50$ μm was observed compared to $L \leqslant 50$ μm. R_{tot} for the 5 μm channel was substantially larger than what would be expected from the linear fit (best seen in the zoom in of Figure 3.17). The fitting for the extraction of R_c has been performed for channel length between 10 μm and 50 μm. The substantially larger R_{tot} for the 5 μm channel and the often observed saturation of R_{tot} for $L < 20$ μm for the *flat films* and in smaller extend also for the *rough film* could be in relation with different morphology at the edge of the Au electrode leading to a non-zero width of the contact region.

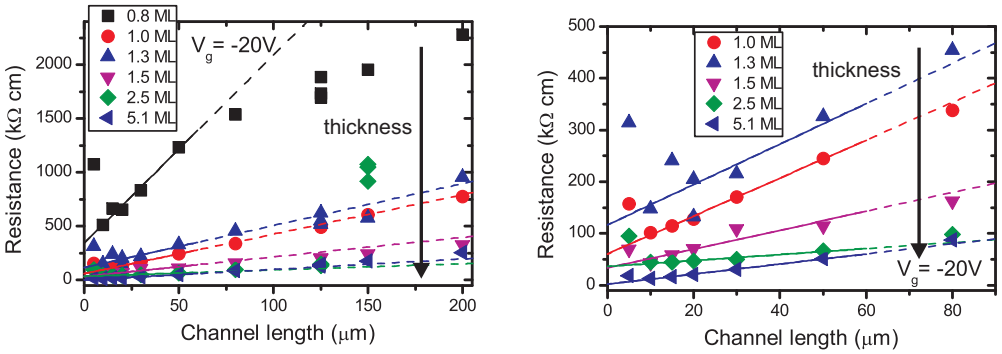

Figure 3.17: Total resistance R_{tot} as function of the channel length L for different channel thickness for the undoped *flat films*. Extrapolating R_{tot} to $L = 0$ gives the contact resistance R_c (see lines). A zoom-in for low L is shown on the right, except for the thinnest channel of 0.8 ML due to the larger resistance compared to the thicker films.

R_{tot} of the TFT with MoO_x contacts for different channel length and thickness is shown in Figure 3.18. R_{tot} varies linearly with L for all channel length between 10 μm and 200 μm. The 5 μm channel could not be measured as the lift-off failed for this

smallest channel leaving no gap between the electrodes. The fit to extract R_c was performed on the values of R_{tot} for L between 10 μm and 80 μm.

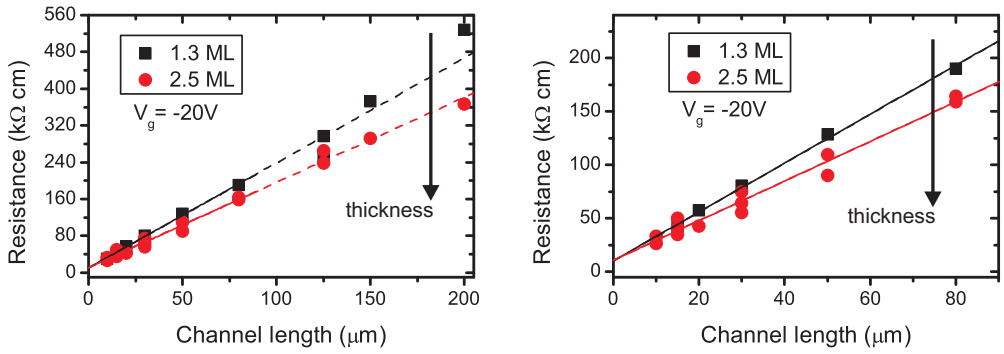

Figure 3.18: Total resistance R_{tot} as function of the channel length L for different channel thickness for the undoped films with MoO_x contacts. Extrapolating R_{tot} to $L = 0$ gives the contact resistance R_c (see lines). A zoom-in for low L is shown on the right.

Figure 3.19 summarizes the contact resistance of the TFTs for the *rough films* and the *flat films* with Au contacts and the TFTs with MoO_x contacts as function of the channel thickness. The error bars indicate the standard variation of R_c obtained from different fits, *i.e.* by taking slightly different range for the fit used to extract R_c. All contact resistance have been normalized by the channel width. The contact resistance of the TFTs with MoO_x contacts is clearly lower than the contact resistance of the *flat films* for channel thickness below 3 ML, while it is comparable for a channel thickness of 5 ML. The contact resistance of the *rough films* is comparable or even lower than of the TFTs with MoO_x contacts, however, the error bar of the contact resistance measurements of the *rough films* is relatively large due to the difficult fitting explained above and might thus be underestimated. Low contact resistance for MoO_x electrodes have been reported in literature [101–105]. Also the insertion of a MoO_x doped pentacene layer between electrode and pentacene semiconductor leads to a low contact resistance [106–108]. This low R_c is a consequence of the effective energy alignment between the transition-metal oxide MoO_x and the molecules [109]. The general observed trend of a reduction of R_c with increasing channel thickness in TFTs with Au electrodes can be attributed to an increased pentacene coverage of the edge of the Au electrodes [26]. This trend was not observed for TFTs with MoO_x electrodes. In contrast to TFTs with Au electrodes, an increase of the channel thickness does not increase the contact area between the pentacene channel and the MoO_x electrode as the pentacene grows in a continuous film across the electrode edge. This improved morphology might also partially cause the observed low contact resistance for the TFTs with MoO_x electrodes.

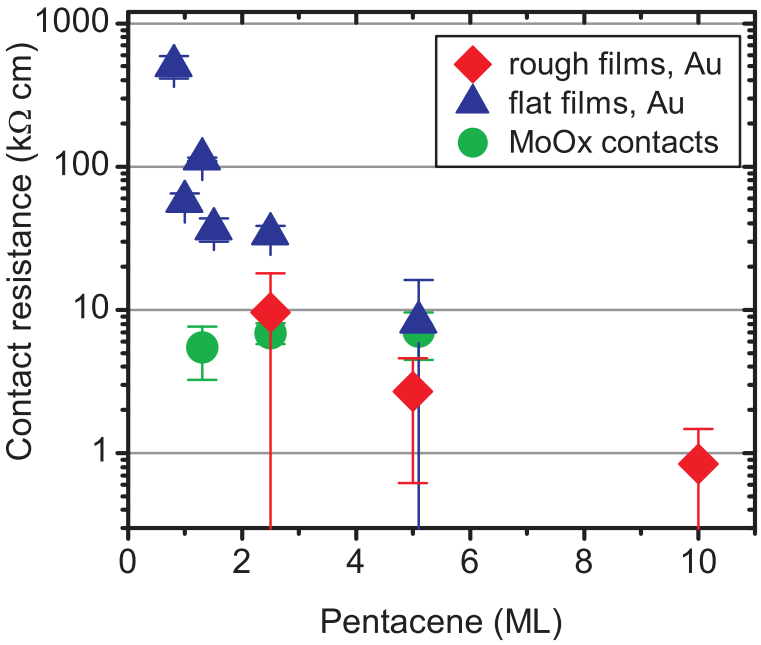

Figure 3.19: Contact resistance R_c of undoped pentacene TFTs for different channel thickness and films, *i.e.* the *rough films* (red diamonds) and the *flat films* (blue triangles) with Au electrodes, and the films with MoO_x contacts (green circles).

3.4.2 Mobility

Figure 3.20 summarizes the mobility of the TFTs of the *rough films* and the *flat films* with Au electrodes and the TFTs with MoO_x contacts. The mobility was extracted using equation 2.3 for a channel length of 60 μm for the *rough films* and for $L = 50$ μm for the *flat films* and the TFTs with MoO_x electrodes (see Figure 3.20(a)). Equation 2.10 was used to extract the contact free mobility (see Figure 3.20(b)). We can see that the mobilities of the different TFTs are comparable. The film morphology seems therefore not to have a substantial influence on the mobility. An initial increase of the mobility with channel thickness can be observed which seems to saturate around $3-5$ ML (best observed for the *flat films*). Generally the contact-free mobility μ_{cf} is larger than the mobility μ_{TFT} extracted directly from the transfer curve. This is not the case for the TFTs with MoO_x electrodes, probably due to the low contact resistance which does therefore less affect the extracted TFT mobility. It is worth to note here that the extracted mobility correspond to the field effect mobility and not to the intrinsic mobility which might be substantially larger: Measurements on field-effect transistors on single-crystal pentacene implied that the intrinsic mobility is in the range of tens of cm^2/Vs, two orders of magnitude larger than the measured mobility, as the number of free charges was only in the order of $\sim 0.4\%$ of the total number of injected carriers [110].

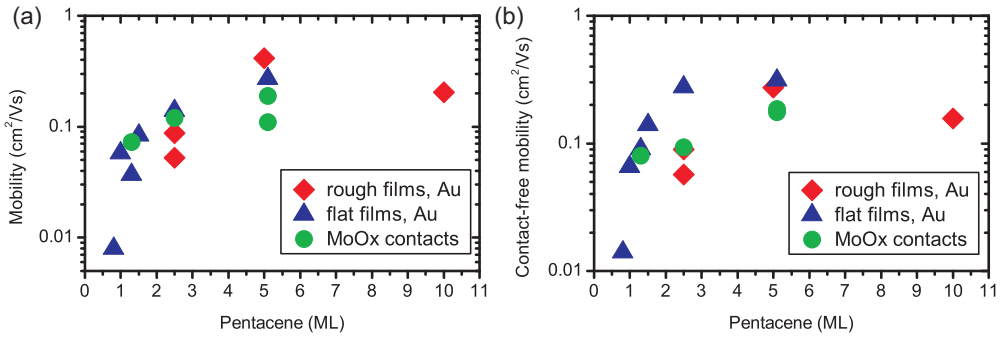

Figure 3.20: (a) Mobility μ_{TFT} and (b) contact free mobility μ_{cf} of undoped pentacene TFT for different channel thickness and different films, *i.e.* the *rough films* (red diamonds) and the *flat films* (blue triangles) with Au electrodes, and the films with MoO_x contacts (green circles). The mobility μ_{TFT} was measured for a channel length L of 60 μm for the *rough films* and for $L = 50$ μm for the *flat films* and those with MoO_x electrodes.

3.5 Summary and Conclusions

We could show that by adapting the evaporation parameters controlled pentacene film growth can be achieved. Thin and smooth pentacene films were obtained where the pentacene grows in a layer-by-layer growth mode at least up to the second or third monolayer. In TFTs with MoO_x instead of Au contacts, the morphology at the contact edge could be further improved where the pentacene now forms a continuous film in the channel, on the electrodes and across the electrode edge. Additionally MoO_x contacts also provide low contact resistances. In these TFTs with MoO_x electrodes with the corresponding high quality pentacene films, the completion of the first few monolayers could even be detected in transport measurements. The results show the influence of the evaporation parameters as well as the choice of the electrode material on the pentacene film morphology.

CHAPTER 4

Surface doping on thin pentacene TFTs

In this chapter we will discuss the surface doping with a variety of molecules on pentacene TFTs with a channel thickness of only 2.5 MLs. It has been shown that in pentacene TFT the current saturates at pentacene channel thickness in the range of 2–7 MLs [52–54], from which follows that the charge transport occurs in the first few MLs next to the gate oxide interface. Our pentacene TFTs have therefore a channel thickness in the range of the observed dimension for the charge transport layer. Figure 4.1 shows the transfer and the output characteristics of such an intrinsic pentacene TFT with a channel thickness of 2.5 ML. The measured threshold voltage was ~ -1 V and the mobility was ~ 0.05 cm^2/Vs. In this chapter we will investigate how the output and mainly the transfer curves are modified when the pentacene TFT is surface doped with different molecules.

The results of this chapter have been published in: Tatjana Hählen, Claudio Vanoni, Christian Wäckerlin, Thomas A. Jung and Soichiro Tsujino. Surface doping in pentacene thin-film transistors with few monolayer thick channels. *Applied Physics Letters*, **101**, 3, 033305–033305–4 (2012). DOI:doi:10.1063/1.4737214

4.1 Principle of surface doping

In this chapter we will discuss the surface doping of pentacene TFTs with different molecules. Here the dopants are not incorporated into the crystal as for standard inorganic semiconductor doping but the dopants are placed on the surface of the semiconductor. Surface doping therefore differs from the bulk doping where the organic

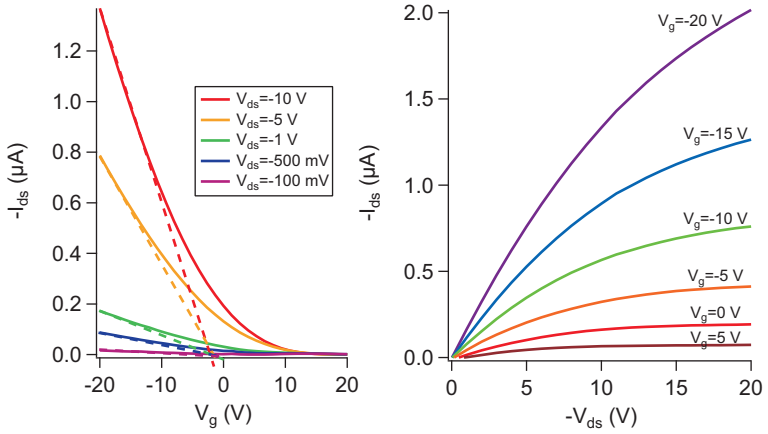

Figure 4.1: (a) transfer and (b) output characteristics of an undoped pentacene TFT with a channel thickness of 2.5 ML. The channel length is 60 μm.

semiconductor and the dopant molecules are co-deposited. Surface doping has the advantage that no modification of the crystal structure is needed. Surface doping has been mostly applied on hydrogen terminated diamond [36, 37, 112], but also on graphene [43], carbon nanotubes [42, 44], silicon [41] and germanium [40] nanowires, 2-methylpropene chemisorbed Si(100)(2×1) [113], and organic semiconductors using functionalized self-assembled monolayers (SAMs) [94, 114]. A nice review of surface doping on semiconductors can be found in Ref. [35].

For surface doping of the here presented organic TFTs, first the pentacene as a channel material is deposited to complete the pentacene TFT and is subsequently surface doped by deposition of a submonolayer film of the dopant molecules on the channel surface (see Figure 4.2). This method allows to study the influence of different surface doping concentration on one single sample by gradually increasing the coverage by the dopant molecules. Surface doping can also be applied with a variety of dopant molecules as the pentacene morphology will not be altered as it might occur with bulk doping due to the incorporation of the dopant molecules. The small channel thickness of the here studied pentacene TFT of only 2.5 ML is expected to be important for effective surface doping. A thin pentacene channel ensures that the dopant molecules are in proximity to the first few monolayers at the gate oxide surface interface where the carrier transport occurs. A study on the correlation of surface doping efficiency and the channel thickness will be discussed in chapter 6.

We studied surface doping of pentacene TFT with the following molecules: 2,3,5,6-tetrafluoro-7,7,8,8-tetracyanoquinodimethane (F_4TCNQ), manganese(III)-tetraphenylporphyrin-chloride (MnTPPCl), cobalt(II)-tetraphenylporphyrin (CoTPP), and fullerene (C_{60}) (Fig. 4.3). F_4TCNQ is known to be a strong electron acceptor due to its low lying lowest unoccupied molecular orbital (LUMO) at -5.2 eV. Doping of pentacene with F_4TCNQ has been applied in a number of experiments,

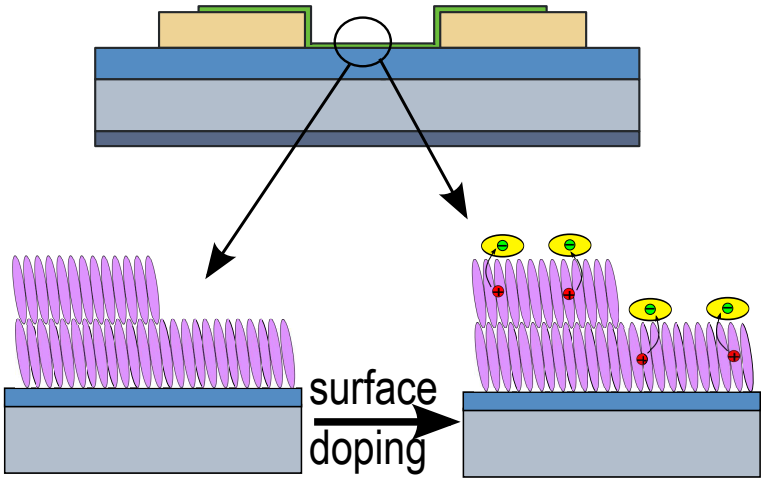

Figure 4.2: Illustration of surface doping: First the channel material, pentacene, is deposited (left) and subsequent surface doping is performed by deposition of submonolayer of dopant molecules (right).

mainly to increase the carrier concentration or to reduce the contact resistance [21, 26–29, 46, 115].

The surface coverage of these doping molecules expressed in ML depends on the size and the packing of the molecules. Assuming the least packed case (*i.e.* with the dopants lying flat), we estimated that the doping coverage was less than a complete monolayer for concentrations below $\sim$0.6 nm^{-2} of MnTPPCl and CoTPP and below $\sim$1 nm^{-2} of F_4TCNQ and C_{60}. The surface doping concentration was estimated from the pentacene thickness, the number of pentacene molecules in the monolayer per unit area in the thin film phase [70], and the molecular weight ratio of the dopant and pentacene as the frequency shift measured by the quartz crystal microbalance is proportional to the deposited mass.

4.2 Change of threshold voltage upon surface doping

We studied the variation of the output and mainly the transfer characteristics of pentacene TFTs surface doped with the different molecules presented above. An increase or decrease of the charge carrier density induced by surface doping will reflect in a shift of the transfer curve towards positive or negative gate voltages, respectively. This shift of the transfer curve with respect to the undoped pentacene TFT is monitored by the threshold voltage and its variation upon surface doping. The threshold voltage shift $\Delta V_{g,th}$, as stated in section 2.1.1, is proportional to the number of doping induced charge carriers. Thus the threshold shift indicates the occurrence of doping and its efficiency. The sign of the threshold shift gives us information about the nature of the doping *i.e.* an increase or decrease of the charge carrier density.

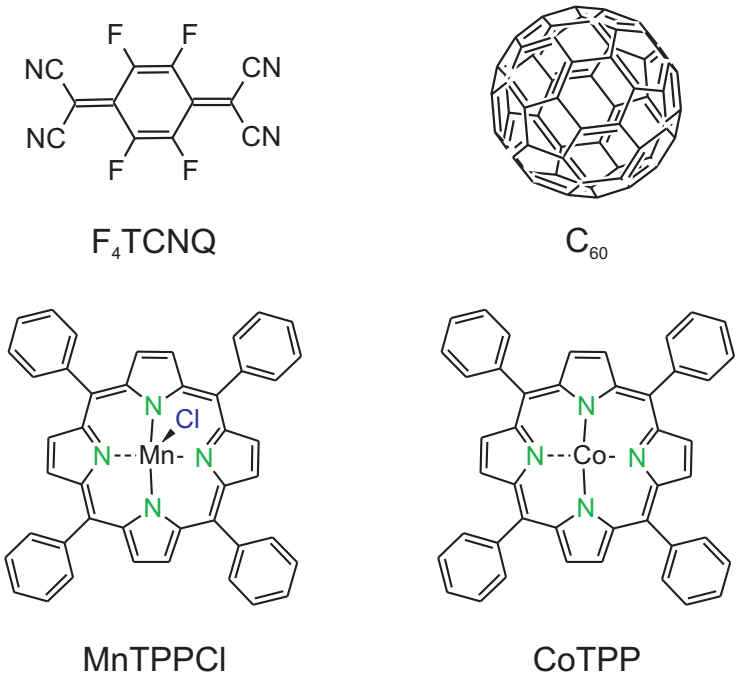

Figure 4.3: Scheme of the molecules used for surface doping.

Figure 4.4 shows the evolution of the output and transfer characteristics of a pentacene TFT with increasing F_4TCNQ surface doping concentration. These data were measured at a fixed V_g of -20 V for the output characteristics and at a V_{ds} of -5 V for the transfer characteristics. The channel length of this TFT was 60 μm, the channel width was 400 μm and the channel thickness was 2.5 ML. The output and transfer characteristics of the undoped pentacene TFT were depicted in Figure 4.1. Increasing the F_4TCNQ surface doping concentration increases the drain-source current I_{ds} in the output characteristics for the applied V_g of -20 V as indicated by the arrow in Figure 4.4(a). More importantly surface doping with increasing coverage of F_4TCNQ shifted the transfer curves towards positive gate voltages (indicated by the arrow in Figure 4.4(b)) in agreement with the acceptor doping of F_4TCNQ *i.e.* an increase of the charge carrier density. Similar shift of the transfer curves has been observed by Vanoni *et al.* [26] for pentacene TFTs which have been bulk doped with F_4TCNQ by coevaporation of pentacene and F_4TCNQ.

Surface doping with MnTPPCl has opposite effects on the output and transfer characteristics compared to surface doping with F_4TCNQ as illustrated in Figure 4.5 for the same V_g, V_{ds} and channel length as for the F_4TCNQ doped TFT. Increasing the MnTPPCl surface doping concentration decreased the drain-source current I_{ds} in the output characteristics for the applied V_g of -20 V (see Figure 4.5). The transfer curves were shifted towards negative gate voltages with increasing MnTPPCl surface doping as indicated by the arrow in Figure 4.5(b). The negative shift of the transfer curves

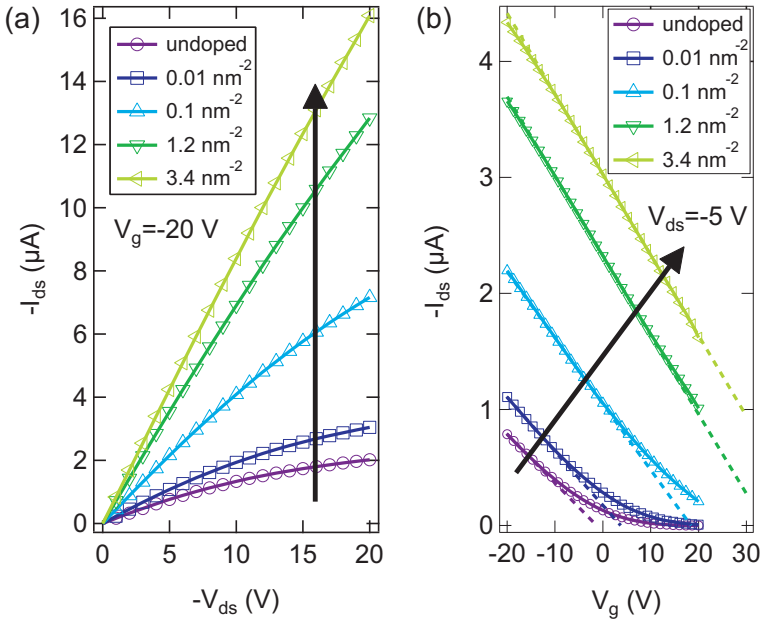

Figure 4.4: (a) output and (b) transfer characteristics of 2.5 ML pentacene TFT with increasing F_4TCNQ surface doping concentration (as indicated by the arrow). F_4TCNQ surface doping leads to increased I_{ds} for a given V_g and shifts the transfer curves towards positive voltages.

indicates a decrease of the hole concentration in the TFT channel.

For a better quantification of the shifts of the transfer curves induced by F_4TCNQ and MnTPPCl surface doping, the evolution of the threshold voltage $V_{g,th}$ for increasing surface doping concentration of F_4TCNQ and MnTPPCl, respectively, is illustrated in Fig. 4.6. The threshold voltage $V_{g,th}$ is extracted in the linear regime according to equation 2.1 by taking the intercept between the fit to the transfer curve (see lines in Fig. 4.4(b) and Fig. 4.5) and the V_g-axis. The corresponding results obtained for CoTPP and C_{60} surface doping are also presented in Fig. 4.6.

For F_4TCNQ concentrations $p_{\text{molecules}}$ below ~0.1 nm^{-2}, $V_{g,th}$ increased proportionally with the increase of $p_{\text{molecules}}$ and then gradually saturated at higher surface doping concentrations. According to equation 2.6, we can determine from the threshold voltage shift $\Delta V_{g,th}$ the charge carrier concentration p_{doping} induced by the doping. The ratio between the doping induced charge carriers p_{doping} and the F_4TCNQ concentration $n_{\text{molecules}}$ gives us the number of induced charges per dopant molecule *i.e.* the doping efficiency η.

$$\eta = \frac{p_{\text{doping}}}{n_{\text{molecules}}} = \frac{C_{ox}\Delta V_{g,th}}{e}\frac{1}{n_{\text{molecules}}} \tag{4.1}$$

For surface doping concentrations below ~0.1 nm^{-2}, where the shift $\Delta V_{g,th}$ increases proportionally to the F_4TCNQ surface doping concentration (illustrated by the straight line in Fig. 4.6), the surface doping efficiency η amounts to ~0.25. Similar the threshold voltage $V_{g,th}$ varies linearly with the MnTPPCl surface doping concentrations for

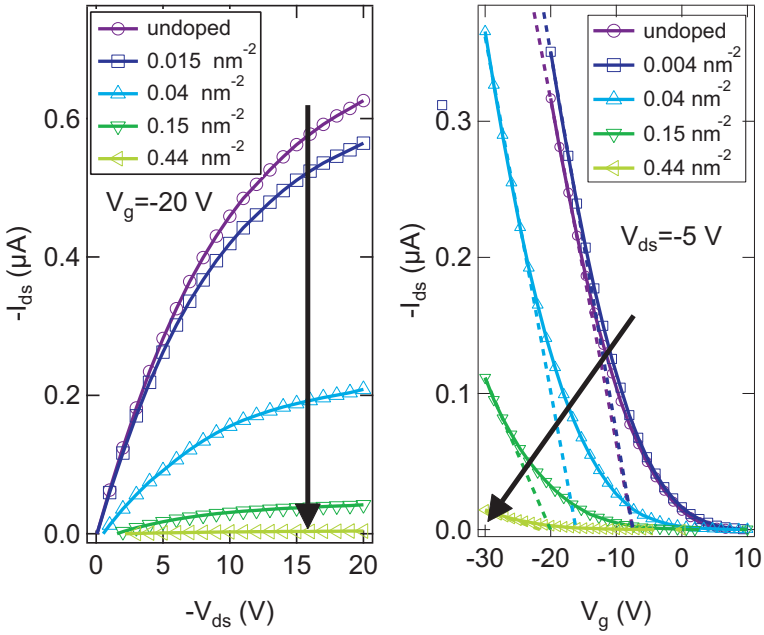

Figure 4.5: (a) output and (b) transfer characteristics of 2.5 ML pentacene TFT with increasing MnTPPCl surface doping concentration (as indicated by the arrow). MnTPPCl surface doping leads to decreased I_{ds} for a given V_g and shifts the transfer curves towards negative voltages.

concentrations below $\sim$0.05 nm^{-2} as indicated by the straight line in Figure 4.6. Interestingly the doping efficiency for MnTPPCl surface doping was found to be in the same order of magnitude as for the F_4TCNQ surface doping (Fig. 4.6). At higher MnTPPCl surface doping concentrations $V_{g,th}$ gradually saturated. We note that the activation ratio for a F_4TCNQ acceptor molecule to supply a hole into pentacene is equal to $\sim \exp(-E_a/(k_BT))$, where $E_a = 0.14$ eV is the energy of the acceptor level of F_4TCNQ with respect to the center of the pentacene HOMO in the density of states (Ref. [27]), k_B is the Boltzmann constant, and T is the temperature. This activation ratio is equal to 4×10^{-3} and therefore a factor of $\sim$60 lower than the observed surface doping efficiency η.

No significant $V_{g,th}$ shift was observed when instead of MnTPPCl a second and similar porphyrin molecule, CoTPP, or an n-type semiconductor C_{60} [116] were used for surface doping, Fig. 4.6. A recent study by Noever *et al.* on pentacene TFT in a top-contact geometry with subsequent deposition of C_{60} showed that at a coverage of about 6 ML of C_{60} ($\sim 6\,\mathrm{nm}^{-2}$) both a small shift of the threshold voltage by 2.1 V as well as the onset of electron conduction in the C_{60} layer could be observed [117]. This effect was observed at a larger coverage of C_{60} than the maximum amount of $\sim$ 1.5 nm^{-2} of C_{60} deposited during surface doping (see Figure 4.6).

As a follow up of these successful experiments, where we showed that the surface doping can be highly efficient to modify the performance of organic semiconductor devices

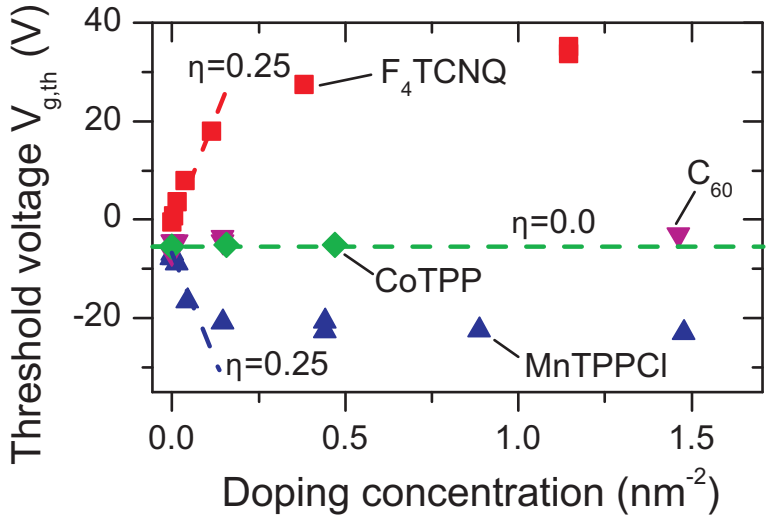

Figure 4.6: Evolution of threshold voltage $V_{g,th}$ of pentacene TFT upon surface doping with the molecules F_4TCNQ, MnTPPCl, C_{60} and CoTPP.

in the nanoscale, we investigated the effect of NO and NH_3 on transport measurement in TFTs. This was motivated by the observation in our group that coordination of metallo porphyrins or phthalocyanines with NO or NH_3 can modify the substrate induced molecular magnetic moments and the magnetic exchange interaction between molecule and substrate [118–121] (see also Appendix A). The results of these, non-conclusive, transport experiments are briefly described in Appendix B.

4.3 Surface doping effect on mobility

Also from the slope of the above linear fit to the transfer curve (see Fig. 4.4(b) and Fig. 4.5(b)), we found that the field-effect mobility was $(4.3 \pm 0.9) \times 10^{-2}\,\mathrm{cm}^2/(\mathrm{Vs})$ for pristine pentacene TFTs. To investigate the effect of surface doping on the mobility, the slope was taken at comparable source-drain current I_{ds} for all surface doping concentrations. This way the mobility is measured at comparable gate voltage V_g compared to the threshold voltage $V_{g,th}$. This is important as the transfer curve varies not completely linear with V_g as seen in the deviation from the linear fit in Figure 4.4(b) and Figure 4.5. From this carefully defined mobility we found that surface doping with F_4TCNQ or MnTPPCl did not substantially change the mobility. This shows that the change of the film quality by the surface doping was minimal.

4.4 Scanning electron microscopy

Figure 4.7 shows scanning electron microscopy (SEM) figures of 2.5 ML thick pentacene films on SiO_2 in its pristine state (a) and surface doped with F_4TCNQ(b), MnTPPCl

(c), CoTPP (d) and C_{60} (e). The SEM pictures were taken in the channel of the above presented surface doped TFTs. The pentacene films surface doped with F_4TCNQ and with CoTPP are not distinguishable from the pristine pentacene films. This can mean that either the dopants are homogeneously distributed over the pentacene film or that the dopants provide only little contrast and those even clusters can not be recognized by SEM. For pentacene surface doped with MnTPPCl we observed dark edges along the borders of the pentacene islands and a few dark dots distributed over the surface, mostly on the uncovered (?) SiO_2. It seems therefore that MnTPPCl preferentially aggregates at the edges of the pentacene islands. These different observations of the pentacene films surface doped with CoTPP and MnTPPCL underline the differences of these two molecules as observed in the surface doping transport measurements. On the pentacene film surface doped with C_{60} also dark dots, mostly on the uncovered SiO_2 surface, can be observed. Along the terraces of the pentacene islands we can observe series of bright dots. C_{60} seems thus to aggregate on the edges of the monolayer steps in the pentacene film.

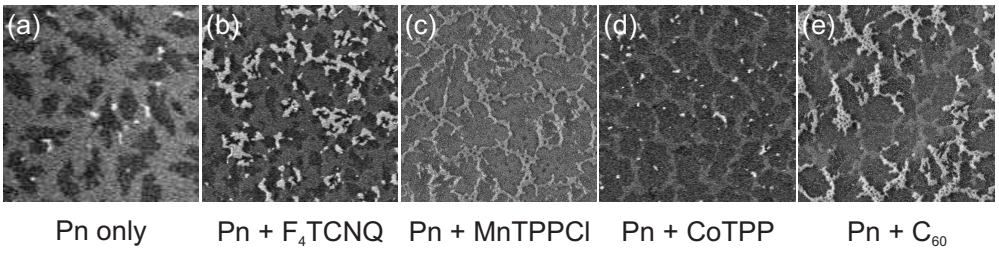

Figure 4.7: SEM images of the 2.5 ML pentacene (Pn) films with dimensions of 5 by 5 μm. For F_4TCNQ (b) and CoTPP (d) doping the dopant molecules are not observed by SEM and there is no substantial difference with respect to the undoped Pn film (a). For MnTPPCl doped Pn (c) dark edges at the boarders of the Pn islands as well as dark dots on the uncovered (?) SiO_2 area could be observed. These dots also appear with C_{60} doping (e) but with bright dots at the edge of the monolayer steps.

4.5 Stacked surface doping

As a side experiment we deposited F_4TCNQ on a 2.5 ML pentacene TFT (*rough film*) which has previously already been surface doped with MnTPPCl. In Figure 4.8(a) the evolution of the threshold voltage $V_{g,th}$ with initial increasing MnTPPCl surface doping and subsequent F_4TCNQ deposition can be observed. The evolution of $V_{g,th}$ upon MnTPPCl doping is similar to the results of a second sample presented in Fig. 4.6. The final MnTPPCl coverage corresponds to 1.5 nm^{-2} which is beyond the surface doping concentration of MnTPPCl for which $V_{g,th}$ saturates. Subsequent deposition of F_4TCNQ induces a shift of $V_{g,th}$ towards positive values, comparable to the results shown in Fig. 4.6 on initially undoped pentacene TFT. For the F_4TCNQ surface doping

concentration of 0.6 nm^{-2} $V_{g,th}$ increased beyond the value of $V_{g,th}$ measured for the undoped pentacene TFT. The decreased charge carrier density by MnTPPCl surface doping could thus be again increased by F_4TCNQ surface doping.

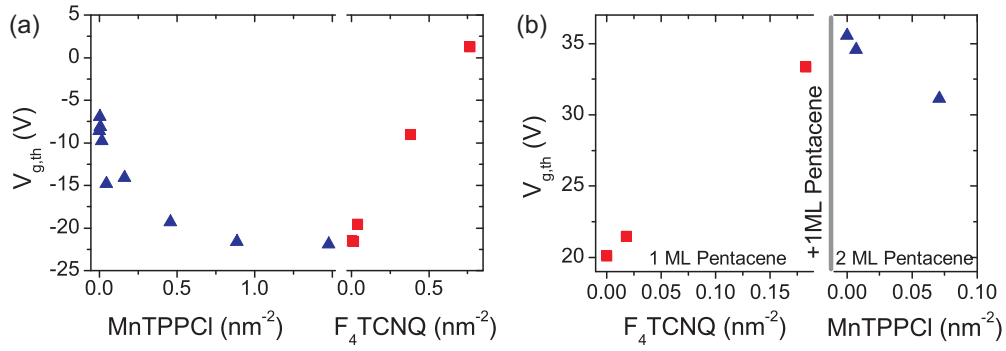

Figure 4.8: Evolution of threshold voltage $V_{g,th}$ for the following experiments: (a) A pentacene TFT with a channel thickness of 2.5 ML is surface doped with an increasing amount of MnTPPCl and subsequently surface doped with F_4TCNQ. The point for zero F_4TCNQ surface concentration corresponds to the point of 1.5 nm^{-2} MnTPPCl surface doping. (b) A pentacene TFT with a channel thickness of 1 ML is surface doped with F_4TCNQ up to a concentration of 0.18 nm^{-2}, then a second monolayer of pentacene is deposited and subsequently doped with MnTPPCl.

In a second experiment a 1 ML pentacene TFT was first surface doped with F_4TCNQ before a second monolayer of pentacene is deposited. Subsequently the TFT is surface doped with MnTPPCl. Figure 4.9 shows SEM and AFM image of the pentacene film on SiO_2. The sample was prepared in the serie of the *flat films*, however, the morphology is more island-like as for the *rough films*. Island-growth could be caused by increased surface contaminations due to a longer transfer time between O_2-plasma and sample loading. The evolution of the threshold voltage for the different stages of surface doping is depicted in Fig. 4.8(b). $V_{g,th}$ increases with increasing F_4TCNQ surface doping concentration. The final F_4TCNQ coverage was 0.18 nm^{-2}. Subsequent deposition of a second monolayer slightly increased $V_{g,th}$. The reason for this increase could be further unintentional F_4TCNQ doping, but was not further studied. MnTPPCl surface doping of this stacked pentacene TFT decreased $V_{g,th}$ similar to MnTPPCl surface doping on undoped pentacene TFT (Fig. 4.6). Therefore the initial increase of the charge carrier density by F_4TCNQ surface doping could be again reduced by MnTPPCl surface doping. The initial large value of $V_{g,th}$ of the undoped TFT may be caused by unintentional F_4TCNQ doping or by surface contamination due to the longer transfer time. This large positive $V_{g,th}$ should not alter the observed result of an increase of $V_{g,th}$ with F_4TCNQ surface doping and again a decrease of $V_{g,th}$ with subsequent MnTPPCl surface doping.

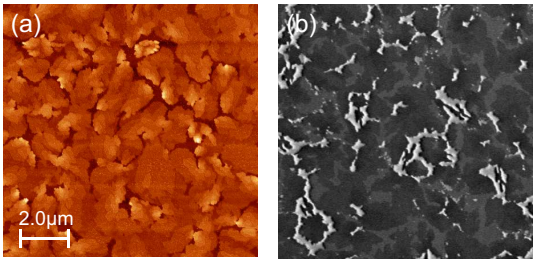

Figure 4.9: (a) AFM and (b) SEM figure showing the morphology of pentacene(1 ML)/ F_4TCNQ(0.18 nm^{-2})/pentacene(1 ML)/MnTPPCl(0.07 nm^{-2}) presented in Figure 4.8(b)

4.6 Summary and conclusions

Surface doping was demonstrated to by highly efficient to modify the charge carrier concentration in pentacene TFTs. Depending on the nature of the guest molecule both an increase and a decrease of the charge carrier concentration can be obtained. Furthermore a surface doping induced increase (decrease) of the carrier concentration can be again decreased (increase) by addition of a second surface dopant having the opposite doping effect to the first dopant molecule. Interestingly only surface doping with one of the two, similar, porphyrins showed a change in the carrier concentration. This result indicates that the detailed molecular structure is important and will be further investigated in Chapter 5 by photoelectron spectroscopy.

CHAPTER 5

Photoelectron spectroscopy to investigate the doping mechanism

In chapter 4 the surface doping of pentacene TFTs with different molecules was studied by transport measurements where positive (negative) shift of the threshold voltage indicates the increase (decrease) of the charge carrier density. In this chapter the transport measurements are compared with photoelectron spectroscopy studies on surface doped pentacene to get further insight into the doping mechanism. Especially the occurrence of a charge transfer between surface dopants and pentacene is investigated.

The results of this chapter have been published in the following publication and the corresponding supplementary material: Tatjana Hählen, Claudio Vanoni, Christian Wäckerlin, Thomas A. Jung and Soichiro Tsujino. Surface doping in pentacene thin-film transistors with few monolayer thick channels. *Applied Physics Letters*, **101**, 3, 033305–033305–4 (2012). DOI:doi:10.1063/1.4737214

5.1 Comparison of molecular orbitals of pentacene and dopants

The F_4TCNQ molecule is known to be a strong electron acceptor and to therefore undergo a charge transfer with pentacene. The mechanism of the charge transfer can be well understood by considering the energy levels of the molecular orbitals for both molecules. The highest occupied molecular orbital (HOMO) of pentacene is situated at $-5.0\,\mathrm{eV}$ and the lowest unoccupied molecular orbital (LUMO) at $-2.8\,\mathrm{eV}$ [20]. For F_4TCNQ the respective orbitals are at $-8.3\,\mathrm{eV}$ and at $-5.2\,\mathrm{eV}$ [122]. The LUMO level of F_4TCNQ is therefore at lower energy than the HOMO level of pentacene, which favors

an electron transfer from the HOMO level of pentacene to the LUMO level of F_4TCNQ. This electron transfer is manifested in the previously shown transfer measurement by a shift of the threshold voltage towards positive voltage due to an increase of the hole concentration in pentacene. The acceptor level, manifested as a modified density of states (DOS) in bulk-doped pentacene TFT, is, however, situated 140 meV above the HOMO level of pentacene [27].

In contrast, it is not apparent from the above HOMO/LUMO considerations why a negative threshold voltage shift was observed for MnTPPCl but not for the similar porphyrin CoTPP (see Chapter 4): the HOMO of CoTPP at −6.5 eV and the LUMO at −3.4 eV [123] suggest that no charge transfer between pentacene and CoTPP is possible, which is in agreement with the absence of any shift of the threshold voltage. The HOMO level of MnTPPCl was found to be at −5.91 eV (see section 5.3.1), which is similar to the HOMO level of CoTPP. The transfer of an electron from MnTPPCl HOMO to pentacene LUMO, expected from the observed negative threshold voltage shift, is therefore difficult. It is therefore even less apparent why only surface doping with one of the porphyrins leads to a negative threshold voltage shift. This issue is now further investigated by X-ray and UV photoelectron spectroscopy.

5.2 X-ray photoelectron spectroscopy

To elucidate the occurrence or non-occurence of a charge transfer between pentacene and MnTPPCl, we complemented the transport measurements by X-ray photoelectron spectroscopy (XPS) of pentacene films doped with MnTPPCl or, as a reference, F_4TCNQ. These were done for pentacene films deposited on Au(111) single-crystal substrates with pentacene thickness comparable to the 2.5 ML on SiO_2. Although the pentacene molecular stacking and film morphology of the pentacene films on Au(111) [22, 124, 125] differs from the pentacene TFT channels deposited on the SiO_2 [66, 68], we expect XPS to give a qualitative indication for the presence or absence of the charge transfer between pentacene and the molecular dopants.

5.2.1 XPS of F_4TCNQ doped pentacene

To investigate the charge transfer between pentacene and F_4TCNQ we first compared a monolayer of F_4TCNQ with a multilayer film of F_4TCNQ on Au(111) (Fig. 5.1(a-d)). It can be observed that F_4TCNQ/Au(111) in the monolayer undergoes charge transfer with Au(111) as evidenced by the strongly modified C1s peak shape (b) with respect to the multilayer (d) and in the N1s signal (a) which is shifted towards lower binding energy compared to the multilayer (c) (c.f. also Ref. [126]). In the multilayer of F_4TCNQ (c+d) the first monolayer undergoing charge transfer with Au(111) is still

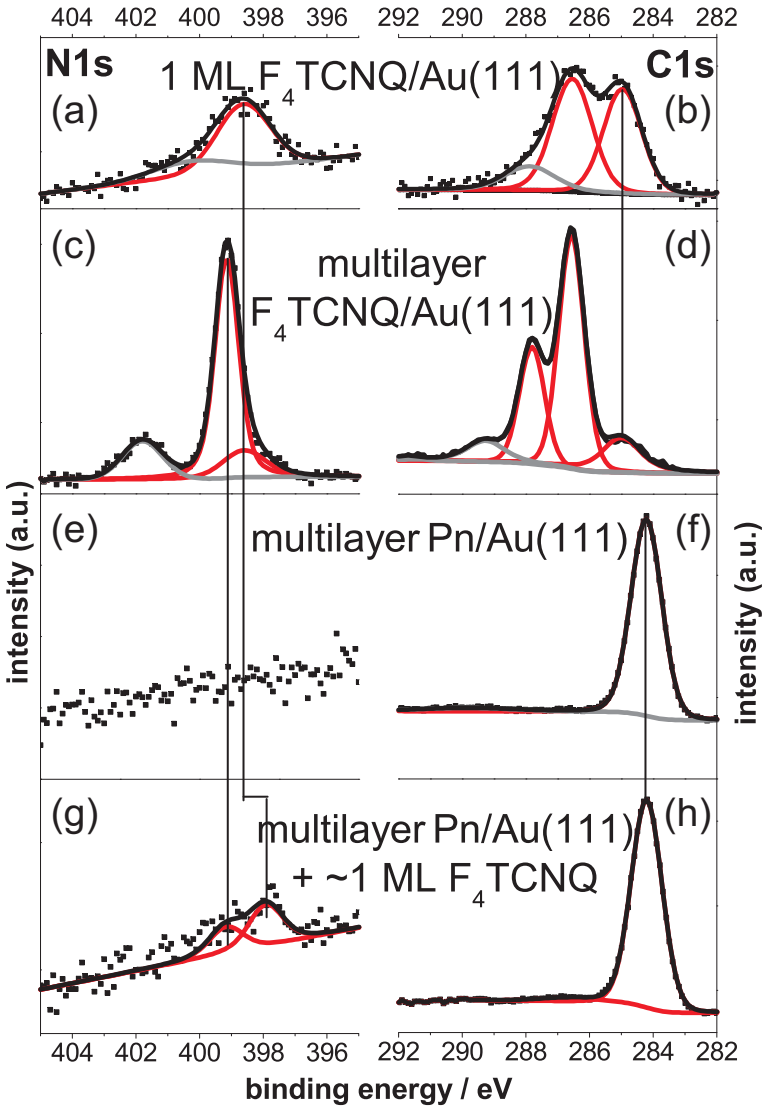

Figure 5.1: N1s and C1s XPS on monolayer and multilayer of F_4TCNQ, multilayer of pentacene (Pn) and multilayer of pentacene with a monolayer of F_4TCNQ on top.

probed by XPS due to the island-like growth of F_4TCNQ on Au(111) (shoulders at lower binding energies in C1s and N1s). The C1s peaks at 286.5 eV and 287.8 eV (d) and the N1s peak at 399.1 eV (c) are ascribed to neutral F_4TCNQ. The signals at higher binding energy are energy loss features (e.g. $\pi \rightarrow \pi^*$ transitions, peak fits in gray color). The multilayer of pentacene (f) yields a single C1s signal at 284.2 eV and a small energy loss feature at higher binding energy. In case of the pentacene multilayer with an additional monolayer of F_4TCNQ evaporated on top (g+h), the signal at low binding energy in the N1s spectra is ascribed to F_4TCNQ which has undergone charge transfer with pentacene. Notably, the binding energy in this case is even lower than for the monolayer of F_4TCNQ on Au(111). The second peak in the N1s spectrum belongs (presumably) to excess F_4TCNQ which has not undergone charge transfer with

pentacene.

The charge transfer of F_4TCNQ with pentacene is therefore observed in our XPS experiments (Figure 5.1) as a peak of the N1s core-level signal at lower binding energies, evidencing the presence of negatively charged F_4TCNQ.

5.2.2 XPS of MnTPPCl doped pentacene

To observe the occurence or the absence of a potential charge transfer between MnTPPCl and pentacene, we have taken XPS spectra on a multilayer of MnTPPCl and on $\sim 1:1$ molar mixture of MnTPPCl and pentacene obtained by co-evaporation. We find that the Mn2p core-level remains unmodified in the MnTPPCl + pentacene mixture (c.f. Figure 5.2). Furthermore, the Cl and N signals of the MnTPPCl multilayer (Cl2p3/2: 197.7 eV; N1s: 399.1 eV) and of the MnTPPCl + pentacene mixture (Cl2p3/2: 197.7 eV; N1s: 399.1 eV) are also found at the same binding energies. The absence of a chemical shift for Mn2p, Cl2p and N1s core levels, strongly suggests that the Mn(III)TPPCl does not undergo charge transfer or chemical reaction with pentacene. This is in contrast to the case when MnTPPCl is evaporated on certain bare metal surfaces. For example, MnTPPCl deposited on Co becomes Mn(II)TPP by losing its Cl ligand, as evidenced by the X-ray absorption spectroscopy (XAS) observation of Mn^{2+} instead of Mn^{3+} and the chemical shift of the Cl2p core level. [127]

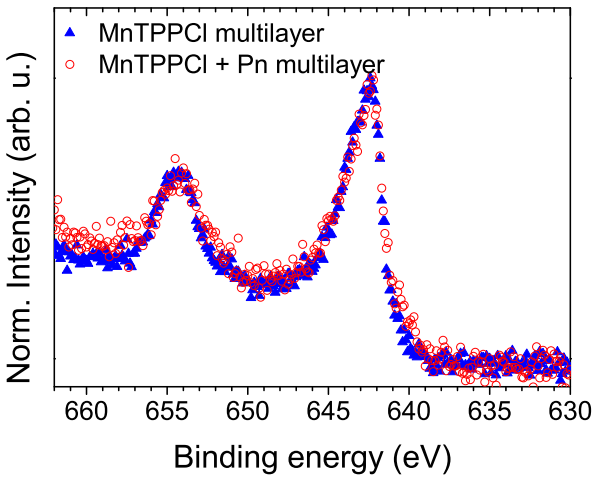

Figure 5.2: Mn2p XP spectra of a multilayer of MnTPPCl/Au(111) and a $\sim 1:1$ molar mixture of MnTPPCl and pentacene (Pn). The Mn2p binding energy and peak shape remains unmodified.

5.3 UV photoelectron spectroscopy

UV photoelectron spectroscopy (UPS) is performed both to determine the HOMO level of MnTPPCl and to investigate the work function of pentacene before and after surface doping.

5.3.1 HOMO level of MnTPPCl

Since we are not aware of UPS data and especially data on the HOMO level of MnTPPCl in the literature, we present UV photoemission spectra (UPS) of a multilayer (50 ML) of MnTPPCl/Au(111) in Figure 5.3. Of particular interest is the position of the on-set of the MnTPPCl HOMO, which is found at 1.72 eV below the Fermi level E_F. The work function is 4.19 eV, as determined by the difference between the secondary electron cutoff (E_{sec}) and the photon energy $h\nu$ of 21.218 eV (He I line). This results in a HOMO level position at 5.91 eV with respect to the vacuum level E_{vac}.

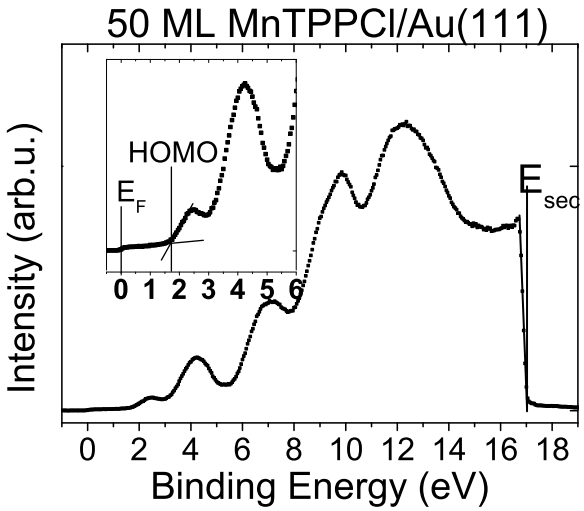

Figure 5.3: UP spectra of a 50 ML MnTPPCl on Au(111). The work function (difference between the secondary electron cutoff (E_{sec}) and the photon energy) is 4.19 eV. The MnTPPCl HOMO onset (see inset) is found at 1.72 eV binding energy (*i.e.* with respect to the Fermi level E_F). This results in a HOMO level position at 5.91 eV (with respect to the vacuum level E_{vac})

5.3.2 Shifted work function after surface doping

We have investigated the effects of surface doping with $\sim$ 1 ML F_4TCNQ, MnTPPCl and CoTPP onto the work function of a multilayer of pentacene on Au(111) (Figure 5.4). The thickness of the pentacene multilayer was comparable to the 2.5 ML of pentacene on SiO_2 in the transport measurement in Chapter 4. The surface doping of $\sim$ 1 ML corresponds to a doping concentration of $\sim$ 0.75 nm^{-2} for F_4TCNQ and of $\sim$ 0.45 nm^{-2}

for the porphyrins MnTPPCl and CoTPP, where the 1 ML refers to the case where the molecules lay flat.

The work function is defined by the position of the secondary-electron cutoff with respect to the initial kinetic energy of the photoelectrons (the photon energy), see also above in section 5.3.1. It yields information on potential charge transfer between the molecular ad-layer and the supporting pentacene multilayer due to formation of an additional electric dipole influencing the vacuum-level at the surface. Also, the presence of ordered molecular electric dipole moments leads to a modification of the work function, c.f. Ishii *et al.* [128] for a detailed discussion.

The work function of the pristine pentacene multilayer is determined to be 4.64 eV (see Figure 5.4). Surface doping with $\sim$ 1 ML F_4TCNQ is found to increase the work function by 590 meV, which is fully consistent with the expected formation of a dipole moment due to a charge transfer from pentacene to F_4TCNQ. For $\sim$ 1 ML MnTPPCl surface doping, a reduction of the work function by 240 meV is observed. Addition of $\sim$ 1 ML CoTPP to the pentacene multilayer does not result in a visible modification of the work function. It is interesting to note that upon F_4TCNQ and MnTPPCl doping the ratio between the work function shifts ($\sim$2.46) is comparable to the ratio of the maximum shifts of $V_{g,th}$ ($\sim$2.4). The unchanged work function in case of CoTPP surface doping excludes charge transfer and is fully consistent with the transport measurements where no shift in $V_{g,th}$ is observed. In case of MnTPPCl, where the above energy level considerations and XPS data do not support a charge transfer with pentacene, the observed work function shift seems not to have its origin in a charge transfer, as in the case of F_4TCNQ doping, but in other dipole formation *e.g.* from the dipole moment of the MnTPPCl molecule (see discussion below).

5.4 Conclusions from photoelectron spectroscopy

From the XPS data of the F_4TCNQ doped pentacene, we observed the emergence of a peak of the nitrogen core level at low binding energies, providing evidence for charge transfer between F_4TCNQ and pentacene. Also from UPS measurement we could observe a increase of the work function which is in agreement with a the formation of a surface dipole through charge transfer between pentacene and F_4TCNQ. However, the XPS data of the MnTPPCl-doped pentacene exhibited no chemical shift for Mn2p, Cl2p and N1s core levels, indicating the absence of the charge transfer and chemical reaction between MnTPPCl and pentacene. This even though a "doping effect" in terms of a negative shift of $V_{g,th}$ could be observed. UPS measurements of surface doped pentacene revealed a reduction of the work function, indicating thus the formation of a surface dipole with opposite sign compared to F_4TCNQ surface doping. The similar porphyrin

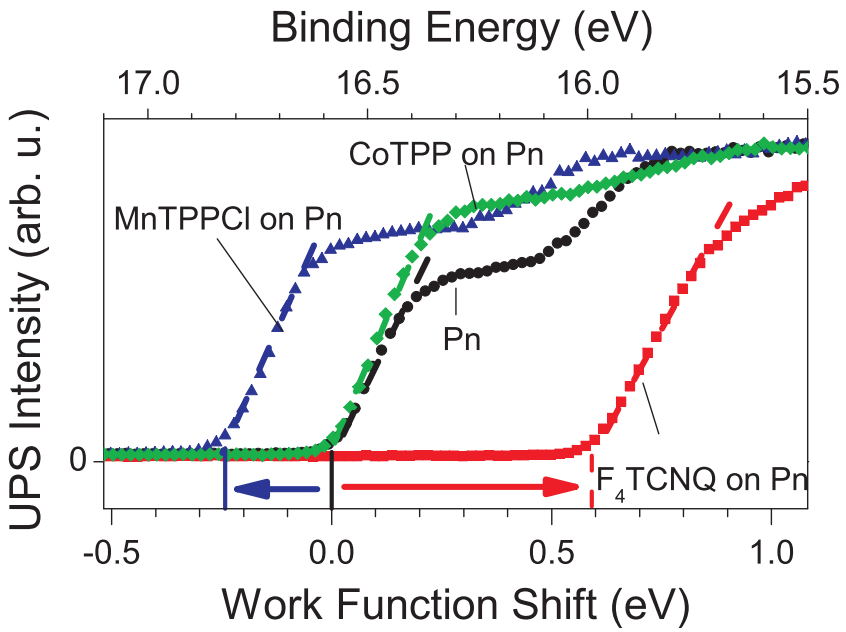

Figure 5.4: Work function changes deduced from UV photoelectron spectra (UPS) of multilayers of pentacene on Au(111) with subsequently sublimed monolayers of F_4TCNQ, MnTPPCl and CoTPP. The work function of the pentacene multilayer (black) is determined to be 4.64 eV. The energy scale is displayed as binding energy and as work function shift relative to the value of the pentacene multilayer. Surface doping with ~ 1 ML F_4TCNQ (red) is found to increase the work function by 590 meV. For ~ 1 ML MnTPPCl (blue) surface doping, a reduction of the work function by 240 meV is observed. Addition of ~ 1 ML CoTPP (green) does not result in a visible modification of the work function.

CoTPP did not show any shift of the work function upon surface doping as it didn't show any shift of $V_{g,th}$. We therefore tentatively ascribe the origin of the apparent n-type doping of MnTPPCl in absence of charge transfer to the molecular dipole moment and its ordering on the pentacene. Such an ordering of the molecular dipole moments of MnTPPCl could explain the observed shift of the work function. Notably, CoTPP does not possess a molecular dipole moment due to the absence of the axial Cl ligand.

CHAPTER 6

Dimension of surface doping induced charge transfer layer

Different from the doping of inorganic semiconductors, the length scale attributed to the charge transfer between the molecular dopant and the pentacene host matrix is likely to be limited to less than a few monolayers because of the weak van der Waals forces governing the inter-molecular coupling in comparison to the covalent bonding in inorganic semiconductors. To provide deeper insight into the length scale of such inter-molecular charge transfer, we studied the surface-doping of the field-induced electrical transport of few MLs-thick pentacene TFTs. Accordingly this chapter presents a study of the charge transfer length between F_4TCNQ guest molecules and a few-ML-thick pentacene films.

6.1 Sharp decay of surface doping efficiency with increased channel thickness

In Chapter 4 we investigated the effect of surface doping on the transfer characteristics, namely on the threshold voltage. In this Section we investigate how the surface doping efficiency depends on the TFT channel thickness. The TFTs presented in this Section correspond to the *flat films* already presented in Chapter 3 which, due to the layer-by-layer growth, are suitable for this study. Figure 6.1 shows the transfer characteristics of pentacene TFTs with a channel thickness between 0.8 ML and 2.5 ML with increasing F_4TCNQ doping concentration up to 0.5 nm^{-2}. As described in Chapter 4 it can again be observed that an increasing F_4TCNQ surface doping concentration induces a shift of the transfer curve towards positive gate voltages. This shift is strongest for the thinnest

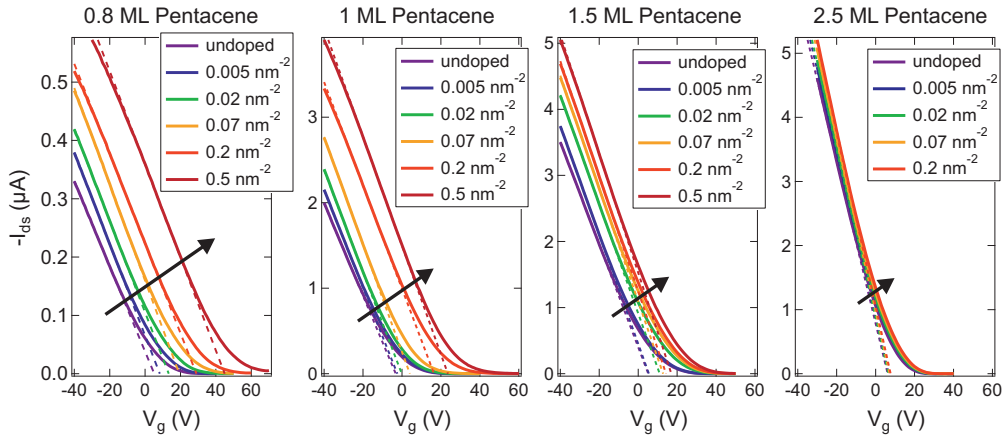

Figure 6.1: Transfer curves of pentacene TFT with the *flat films* for different surface doping concentrations and channel thickness. The applied source-drain voltage V_{ds} is -5 V and the channel length is 50 μm.

pentacene film of 0.8 ML and diminished with increasing channel thickness. The shift of the transfer curve for the 1.5 ML is only about half of the shift of the 0.8 ML film. The TFT with a channel thickness of 2.5 ML pentacene shows almost no shift of the transfer curve upon surface doping. Similar the surface doping induced increase of the current I_{ds} in the output characteristics is diminished with increasing channel thickness (see Fig. 6.2).

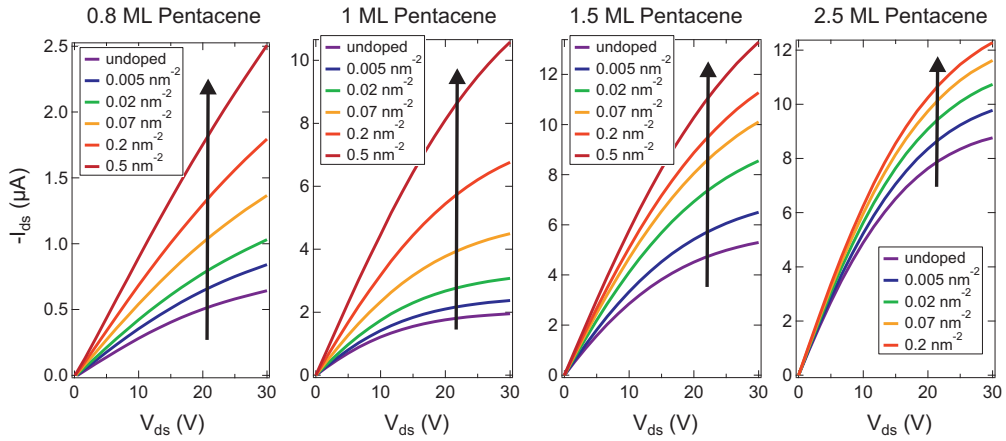

Figure 6.2: Output curves of pentacene TFT with the *flat films* for different surface doping concentrations and channel thickness. The applied gate voltage V_g is -20 V and the channel length is 50 μm.

For a better illustration of the induced shift of the transfer curve, Figure 6.3 summarizes the shift of the threshold voltage $\Delta V_{g,th}$ for the TFTs with different channel thickness and increasing surface doping concentration. It can be clearly seen that the induced shift $\Delta V_{g,th}$ increases with increasing doping concentration but is reduced for a given doping concentration when the channel thickness is increased. The TFTs with a

channel thickness of 2.5 ML and 5.1 ML show almost no shift upon surface doping even for the highest deposited surface doping concentration of 0.54 nm^{-2}.

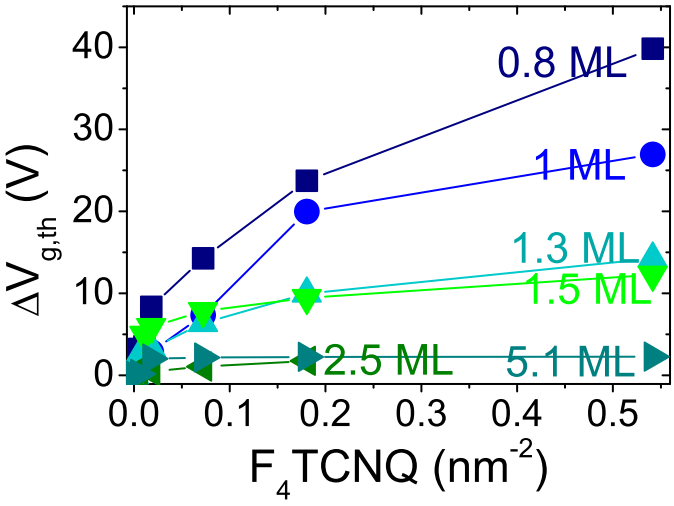

Figure 6.3: Evolution of threshold voltage shift $\Delta V_{g,th}$ as a function of the surface doping concentration for TFTs with the *flat films*.

Figure 6.4 summarizes the relation between $\Delta V_{g,th}$ and the pentacene thickness for the above presented *flat films* and for the TFTs equipped with MoO_x electrodes described in Chapter 3 when both were surface-doped by F_4TCNQ with a concentration of 0.18 nm^{-2}. The shift $\Delta V_{g,th}$ is according to equation 2.6 proportional to the amount of induced charge carriers in the pentacene channel contribution to the charge transport and thus indicates the efficiency of the surface doping. No significant difference in the measured threshold voltage shifts was observed for the TFTs with their channel lengths between 50 and 125 μm. We observed that $\Delta V_{g,th}$ of the *flat films* with the channel thickness of 0.8 ML is 26.2 ± 2.5 V and that $\Delta V_{g,th}$ decreased to 2.75 ± 1 V with the increase of the channel thickness to 2.5 ML. From this sharp decrease of the doping efficiency, we conclude that the transferred charges from the sub-monolayer F_4TCNQ to the pentacene film are limited within $\sim$ 1 ML at the surface of the pentacene film. This confinement for the doping induced holes within the one monolayer pentacene film in contact with the dopant is also confirmed by the measurements on pentacene TFTs with similar film morphology as the *flat films* but equipped with the MoO_x instead of the Au electrodes; essentially no shift of $V_{g,th}$ was observed for the 2.5 ML film whereas $V_{g,th}$ shifted by 20.6 V for the 1.3 ML film and a F_4TCNQ surface doping concentration of 0.18 nm^{-2}. The shifts $\Delta V_{g,th}$ measured for TFTs with MoO_x contacts overlap therefore well with those TFTs with the *flat films* equipped with Au contacts.

The surface doping range of 1 ML is comparable to results from photoelectron spectroscopy measurements on CF_3-SAM/Au(111) with increasing CuPc coverage where

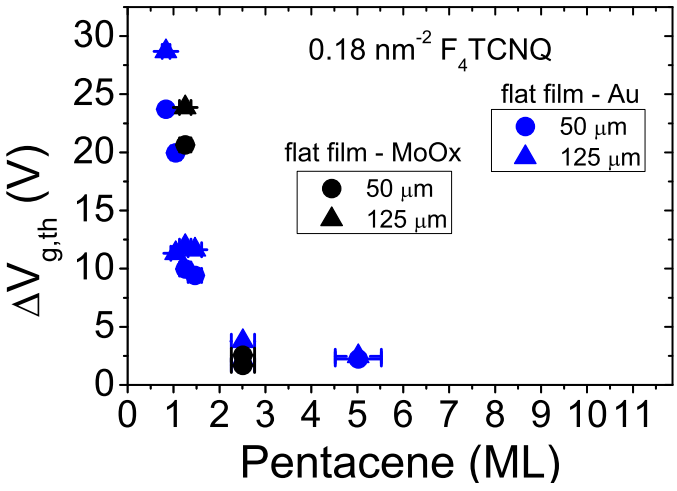

Figure 6.4: Evolution of the surface doping efficiency expressed in the threshold voltage shift $\Delta V_{g,th}$ as function of the channel thickness of pentacene TFT. The F_4TCNQ surface doping concentration is 0.18 nm^{-2}.

CF_3-SAM acts as the dopant and CuPc is the organic semiconductor [114]. These results found the thickness of the doping region to be 30 Å, which corresponds to about 2.3 ML of CuPc with the molecules being in an upright position (standing).

6.2 Influence of morphology on surface doping efficiency

The results above were presented for TFTs with the *flat films* equipped with Au electrodes and for TFTs equipped with the MoO_x electrodes. In both TFFs the pentacene films show layer by layer growth at least up to the second monolayer (see Chapter 3) which corresponds to the range within which the sharp decay of the surface doping efficiency was observed. The TFTs with the *rough films* were, however, the first ones to be produced and thus the surface doping efficiency as a function of the channel thickness has been first studied for those *rough films*. Figure 6.5 shows the transfer curves and Figure 6.6 the output characteristics of the pentacene TFTs with the *rough films* for different channel thickness and F_4TCNQ surface doping concentrations. Figure 6.7 summarizes $\Delta V_{g,th}$ for channel thickness between 2.5 ML and 10 ML and for different F_4TCNQ surface doping concentration. The results for the 2.5 ML pentacene TFT correspond to those already presented in Figure 4.6. Comparable to results from the *flat films*, the shift $\Delta V_{g,th}$ is largest for the thinnest pentacene film (here 2.5 ML) and $\Delta V_{g,th}$ drops by more than a factor of two upon increasing the channel thickness to 5 ML for a surface doping concentration of $\sim 0.4\,nm^{-2}$ F_4TCNQ. However, non-zero shift $\Delta V_{g,th}$ are observed for the 5 ML and even the 10 ML films after surface doping and $\Delta V_{g,th}$ is comparable for both thickness.

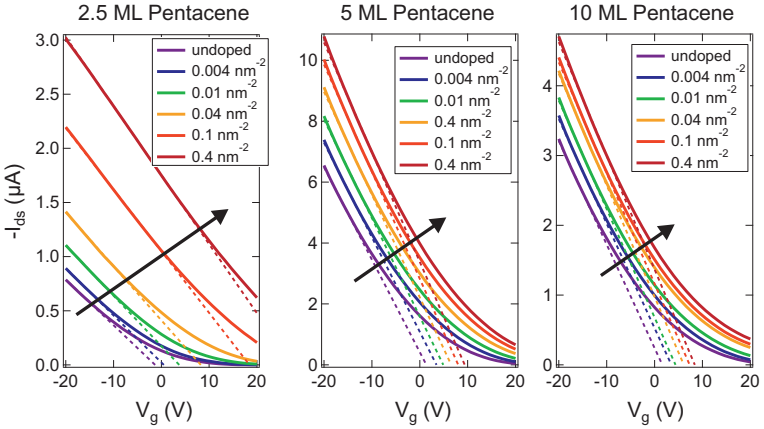

Figure 6.5: Transfer curves of pentacene TFT with the *rough films* for different surface doping concentrations and channel thickness. The applied source-drain voltage V_{ds} is -5 V and the channel length is 60 μm.

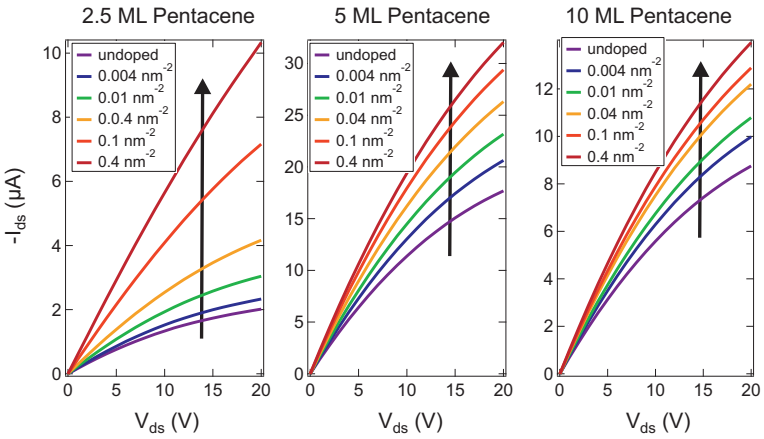

Figure 6.6: Output curves of pentacene TFT with the *rough films* for different surface doping concentrations and channel thickness. The applied gate voltage V_g is -20 V and the channel length is 60 μm.

Figure 6.8 shows the evolution of $\Delta V_{g,th}$ for the *rough films* together with the results from the above presented TFTs with *flat films* and the TFTs equipped with MoO_x contacts at a surface doping concentration of 0.18 nm^{-2}. The $\Delta V_{g,th}$ values of the *rough films* at a surface doping concentration of 0.18 nm^{-2} have been calculated by performing a linear interpolation between the next lowest and highest concentration for which $\Delta V_{g,th}$ has been measured (see Figure 6.7) and its spread is shown as error bars in Figure 6.8. $\Delta V_{g,th}$ of the 2.5 ML *rough film* is comparable to the values of the 0.8 ML *flat films* and the 1.2 ML in TFTs with MoO_x electrodes. For the $5-10$ ML-thick *rough films* $\Delta V_{g,th}$ still reached more than 5 V at the F_4TCNQ concentration of 0.18 nm^{-2} and $\sim$ 10 V at saturating doping concentration of $\sim$ 1 nm^{-2}. These values are substantially larger than the observed $\Delta V_{g,th}$ of the 2.3 ML-thick *flat films*. We consider that this fact is caused by the diffusibility of the F_4TCNQ and the spatial

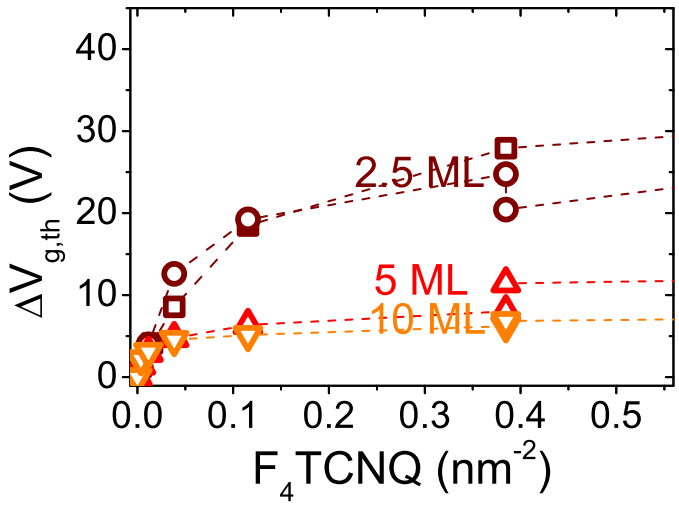

Figure 6.7: Evolution of threshold voltage shift $\Delta V_{g,th}$ as a function of the surface doping concentration for pentacene TFT with *rough films*.

thickness variation of the pentacene channel. In fact, SEM and AFM inspection of these *rough films* (see Figure 3.6) showed a strong non-uniformity of the films; ensembles of $\sim$0.5 μm-scale grains were clearly visible. In particular, at some grain boundaries, the AFM measurement showed zones with pentacene thickness of $0-2$ ML to which the F_4TCNQ dopant molecules can migrate and thereby influence the charge carriers. This interpretation is consistent with the experiment on TFTs with the *flat films* and on TFTs equipped with MoO_x electrodes.

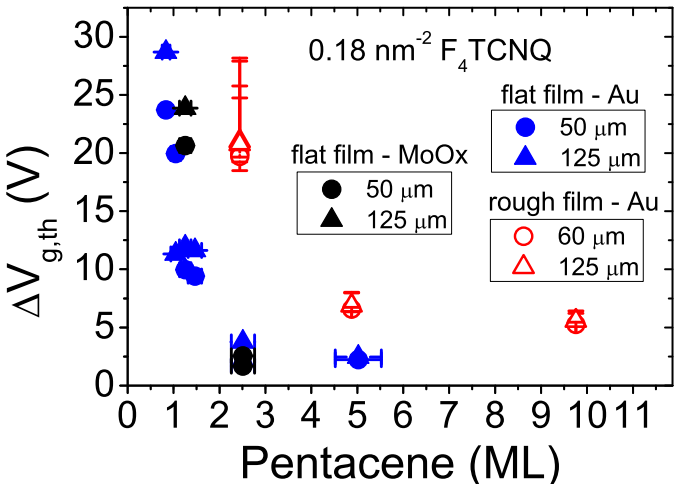

Figure 6.8: Evolution of the surface doping efficiency expressed in the threshold voltage shift $\Delta V_{g,th}$ as function of the channel thickness of pentacene TFT. The surface doping concentration is 0.18 nm^{-2}.

This result highlights the importance of the film morphology affecting charge transfer

and carrier generation in organic semiconductors. The surface roughness (in particular its absence) of the organic semiconductor directly affects the interpretation of literature reported experiments on the spatial confinement of the field-induced carriers at the insulator-semiconductor interface of organic TFTs [53, 129, 130] as well as on the doping induced creation of holes at the interface between fluorinated self-assembled monolayer and organic semiconductor layers [30, 94, 114].

6.3 Effect of surface doping on the contact resistance

Next we discuss the effect of both the surface doping and the channel thickness on the contact resistance. In Figure 6.9, we summarized the variation of the contact resistance with the increase of the surface doping concentration for TFTs with the channel thickness of 0.8 ML (blue squares), 1 ML (green circles), and 1.5 ML (red triangles), respectively. The values were normalized to the maximum value of the undoped case for each thickness. We observed that the contact resistance decreased with increasing surface doping concentration. The magnitude of the contact resistance decrease was however in the order of $10-50\%$ for all these films, in contrast to the bulk-doping case, in which the contact resistance of 6 ML-film decreased more than an order of magnitude [26] (see Figure 6.10). The diminishing fraction of the doping-induced contact resistance decrease with the increase of the pentacene channel thickness is in agreement with the above observed decrease of the doping efficiency with increased channel thickness.

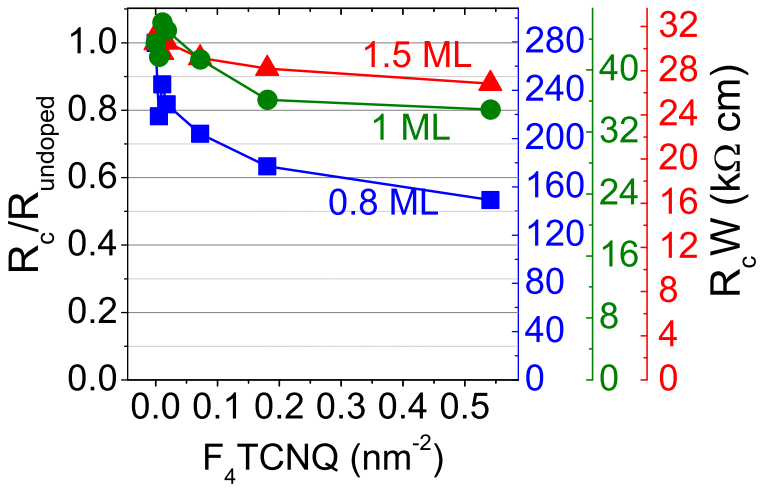

Figure 6.9: Contact resistance R_c vs. surface doping concentration for pentacene TFTs with the channel thickness of 0.8 ML (blue squares), 1 ML (green circles), and 1.5 ML (red triangles) with the abscissa in the respective color on the right. The reduction of the contact resistance by doping amounts to a factor of two for the thinnest film of 0.8 ML pentacene and diminishes for thicker films, as seen on the left abscissa representing the normalized contact resistances by the respective undoped one.

The rather small decrease of the contact resistance with surface doping compared to the more than one order of magnitude decrease for pentacene TFTs bulk doped with F_4TCNQ [26] could be understood by two possible explanations; First R_c of the 1 ML and 1.5 ML *flat films* in its pristine state were ~ 3 times lower than the R_c measured by Vanoni *et al.* [26] and those of the TFTs with MoO_x were even comparable to the R_c of the bulk doped TFTs (see Figure 6.10). It is thus possible that due to the already lower R_c not much further improvement can be achieved by doping. Second it is possible that the contact resistance reduction by doping requires that the dopant molecules reside in close proximity to the contact metal surface. This means that mere charge transfer from F_4TCNQ to pentacene seems insufficient to reduce the injection barrier height unless the dopant molecule directly resides on the contact metal surface.

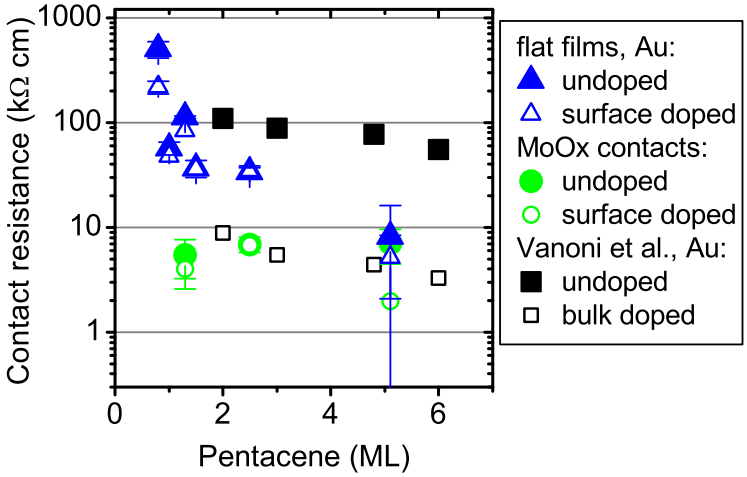

Figure 6.10: Contact resistance R_c for different channel thickness and for both TFTs with *flat films* equipped with Au electrodes (blue triangles) and TFTs equipped with MoO_x contacts (green circles). The large filled symbols correspond to the R_c measured on undoped TFTs and the small empty symbols to the TFTs surface doped by 0.54 nm^{-2} F_4TCNQ (0.18 nm^{-2} F_4TCNQ for the 2.5 ML *flat film*). For comparison the R_c from Vanoni *et al.* [26] are shown for undoped TFTs (filled black squares) and the TFTs bulk doped with 1.5 mol% F_4TCNQ (empty black squares).

Further investigation e.g. by scanning tunneling microscopy and spectroscopy will be needed to elucidate the microscopic nature of these processes. Also from temperature dependent transport measurement the barrier height for the hole injection at the pentacene-electrode interface can be measured to investigate a possible reduction of the barrier height induced by surface doping as well as to compare the barrier height with those of Vanoni *et al.* [27].

6.4 Confinement of charges: comparison with calculations

In this section we compare the above presented results on the strong dependence of the surface doping efficiency on the channel thickness with calculations.

6.4.1 Calculations based on bulk pentacene

Starting from the Poisson equation (equation 6.1) we want to calculate the charge distribution in pentacene TFTs in order to estimate the width of the gate induced accumulation layer and of the F_4TCNQ surface doping induced charge transfer region.

$$\frac{\mathrm{d}^2V}{\mathrm{d}x^2} = -\frac{e\rho}{\epsilon_0\epsilon_r} \tag{6.1}$$

where: V – electric potential, *i.e.* the position of the pentacene HOMO level,
x – the axis normal to the insulator-semiconductor, respectively the dopant-semiconductor interface,
ρ – the density of charge carriers ,
e – the elementary charge ,
ϵ_0 – the vacuum permittivity, and
$\epsilon_r = 4$ – the relative dielectric constant of pentacene.

The electrical potential is defined to be zero for x at infinity. Thus the zero potential correspond to the position of the HOMO level in the bulk infinitely away from the surface (see also Figure 6.11) and the semiconductor is supposed to be of infinite thickness.

Following the arguments of Refs. [100, 131] we can calculate the electric field F_x as

$$F_x = \left[\left(\frac{2}{\epsilon_0\epsilon_r}\right)\left|\int_0^V e\rho(V')\mathrm{d}V'\right|\right]^{1/2} \tag{6.2}$$

and the potential distribution as function of the distance x follows from

$$x = \int_V^{V_0} \frac{\mathrm{d}V'}{F_x(V')} \tag{6.3}$$

where: V_0 – surface potential of the semiconductor at the interface.

For gate induced charge carriers (see Figure 6.11(a)) the gate voltage is related to the total induced charge carriers per unit area Q_{ind} due to charge neutrality and supposing flat band condition as

$$-V_gC_{ox} = Q_{\text{gate ind.}} = \epsilon_0\epsilon_r F_x(0) \tag{6.4}$$

where: C_{ox} – gate capacitance, and

$F_x(0) = F_x(V = V_0)$ – the electric field at the semiconductor-insulator interface.

From those equations it is thus possible to calculate the potential $V(x)$ and the density of hole $\rho(x)$ at different distances from the semiconductor-insulator interface for a given applied gate voltage V_g.

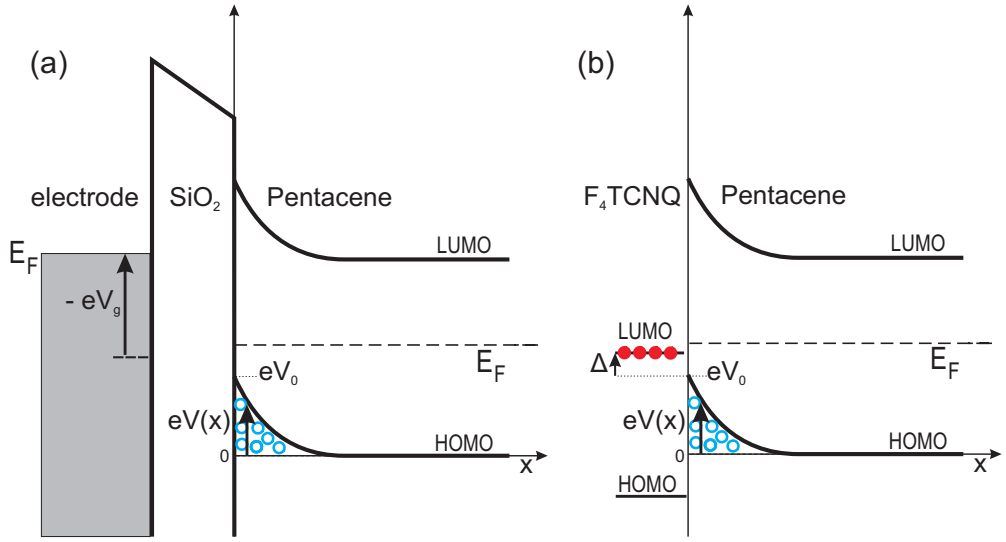

Figure 6.11: Illustration of the induced band bending and subsequent charge accumulation (a) at the pentacene-insulator interface due to an applied negative gate voltage V_g or (b) at the pentacene-dopant interface due to a charge transfer.

For surface doped pentacene we need to have charge neutrality between the doping induced charge carriers and the ionized dopants (see Figure 6.11(b)). Here we can follow the arguments of Ristein *et al.* [37, 112] who performed similar calculations for surface doped diamond. For an averaged areal density of dopant molecules $n_{\text{molecules}}$, the number of electrons in the molecule's LUMO level is given by Fermi-Dirac statistics as

$$n(V_0) = n_{\text{molecules}} \frac{1}{\mathrm{e}^{\frac{\Delta + eV_0 - E_F}{k_B T}} + 1} \tag{6.5}$$

where: V_0 – the surface potential of pentacene *i.e.* the Pentacene HOMO level at the semiconductor-dopant interface,
Δ – the energy difference between the LUMO level of the dopant and the HOMO level of pentacene,
E_F – the Fermi level,
k_B – the Boltzmann constant, and
T – the temperature.

Therefore equation 6.4 in case of surface doping modifies to

$$n_{\text{molecules}} \frac{1}{\mathrm{e}^{\frac{\Delta + eV_0 - E_F}{k_B T}} + 1} = Q_{\text{doping ind.}} = \epsilon_0 \epsilon_r F_x(0). \tag{6.6}$$

The value of Δ is -0.2 eV when considering the difference between the LUMO level of F_4TCNQ and the HOMO level of pentacene (see Chapter 5) and 0.138 eV when considering the position of the acceptor states observed in the density of states of pentacene bulk doped with F_4TCNQ [27].

To adapt the calculations to pentacene we use a gaussian density of states (DOS) with an exponential tail into the band gap [132, 133]. This is different from the above citations where a DOS based on the effective mass approximation ($D(E) \propto \sqrt{E_V - E}$) has been used. The gaussian DOS $D_{\text{Gauss}}(E)$ can be described as

$$D_{\text{Gauss}}(E) = \frac{N_V}{\sqrt{2\pi}\sigma} \mathrm{e}^{-\left(\frac{E - E_V}{\sqrt{2}\sigma}\right)^2} \tag{6.7}$$

where: N_V – the total density of states,
$E_V = eV$ – the center of the Gaussian, *i.e.* the position of the HOMO level, and
σ – the Gaussian width (variance)

and the exponential tail $D_{exp}(E)$ as

$$D_{exp}(E) = \begin{cases} N_0 \mathrm{e}^{-\frac{E - E_V}{k_B T_0}}, & \text{if } (E - E_V) \geq 0 \\ 0, & \text{otherwise} \end{cases} \tag{6.8}$$

where: N_0 – the trap density, and
T_0 – an effective temperature.

N_V is set to the density of pentacene molecules (see also Refs. [49, 132]) which corresponds to 2.9×10^{21} cm^{-3} [70] and σ was set to 0.035 eV, which fits relatively well the DOS reported by Vanoni *et al.* [27]. T_0 is 1330 K as stated by Vanoni [49] and N_0 was taken as 3.6×10^{18} eV^{-1}cm^{-3} which is one order of magnitude smaller than the cited value by Vanoni but fits the reported DOS much better. The Fermi energy was set to 1 eV, which correspond to the mid-gap position. The exact position of the Fermi level has however minor influence on the results and using the Boltzmann approximation instead of the Fermi distribution and $D(E) \propto \sqrt{E_V - E}$ for the DOS, the Fermi level falls out of the calculations (see Refs. [112, 129]). The calculations were performed with Mathematica [134] (see Appendix B for the Mathematica code).

Figure 6.12 shows the evolution of the potential V, the carrier density ρ and the integrated carrier density in each monolayer for increasing distance from the semiconductor-insulator interface and for an applied gate voltage of -10 V and -30 V respectively. It can be observed, that the carrier density decreases by about one order of magnitude within the first ML. Calculating the thickness of the accumulation layer as stated by Horowitz; "a layer of uniform charge density that would contain the same amount of charge than that obtained by integrating the charge distribution" [129] *i.e.* $(\int_x^\infty \rho(x)\mathrm{d}x)/\rho(x=0)$, we get a thickness of the accumulation layer of 0.82 nm and 0.29 nm for V_g of -10 V and -30 V respectively, which is below the thickness of 1 ML (1.5 nm).

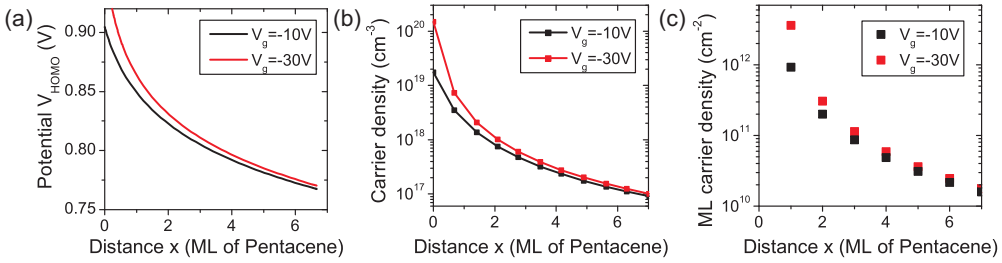

Figure 6.12: (a) Calculated evolution of the potential, (b) the carrier density and (c) the carrier density in each monolayer in undoped pentacene with distance x from the semiconductor-insulator interface for an applied gate voltage V_g of -10 V (black) and -30 V (red) respectively.

In Figure 6.13 we summarize the potential V, the carrier density ρ and the integrated carrier density in each monolayer for different positions from the semiconductor-dopant interface, *i.e.* the surface, with a F_4TCNQ surface doping concentration of 0.18 nm^{-2} both for $\Delta = -0.2$ eV and $\Delta = 0.138$ eV. For both values of Δ we see that the carrier density decreases by at least one order of magnitude within the first monolayer from the surface. The thickness of the accumulation, or rather of the charge transfer region, is found, according to the above definition, to be 0.15 nm and 0.63 nm for $\Delta = -0.2$ eV and $\Delta = 0.138$ eV respectively. Those values are comparable to the accumulation layer induced by a gate voltage and are again below the thickness of 1 ML.

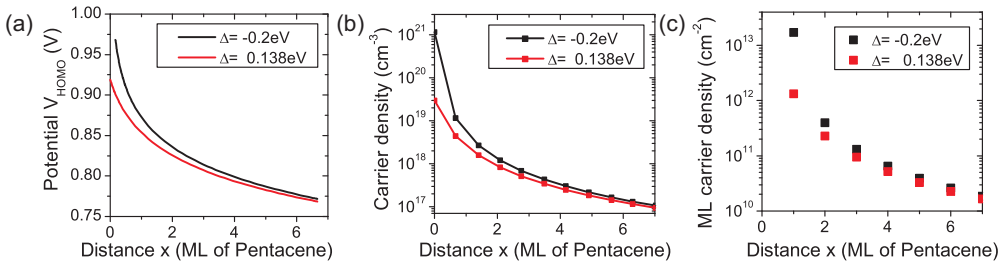

Figure 6.13: (a) Evolution of the potential, (b) the carrier density and (c) the carrier density in each monolayer in pentacene with distance x from the semiconductor surface, calculated for an F_4TCNQ surface doping concentration of 0.18 nm^{-2} and with $\Delta = -0.2$ eV (black) and $\Delta = 0.138$ eV (red) respectively.

The monolayer carrier density in the respective first four monolayers from the surface and for different surface doping concentrations is displayed in Figure 6.14. It can be observed, that at low doping concentrations the carrier density strongly increases with increasing doping concentrations and saturates at larger surface doping concentrations. This is in agreement with the observed threshold voltage shifts for increasing doping concentrations (see Figures 4.6, 6.3 and 6.7).

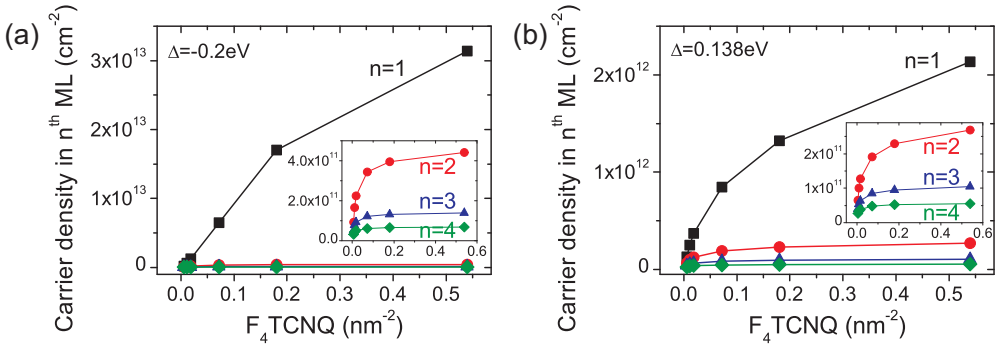

Figure 6.14: Calculated carrier density in the 1st ML (black squares), 2nd ML (red circles), 3rd ML (blue triangles) and 4th ML (green diamonds) from the pentacene-dopant interface for different F_4TCNQ doping concentrations and for (a) $\Delta = -0.2$ eV and (b) $\Delta = 0.138$ eV. The insets show a zoom-in for n^{th} monolayer with $n \geq 2$.

In Figure 6.15 we calculate the gate voltage V_g to apply to induce the same total areal charge density as induced by surface doping with 0.18 nm^{-2} F_4TCNQ *i.e.* by charge transfer (CT). These gate voltages can be compared to the experimentally measured surface doping induced gate voltage shifts. The largest experimentally measured threshold shift for a surface doping concentration of 0.18 nm^{-2} was 26.2 ± 2.5 V, corresponding to the 0.8 ML thick channels. This value is between the V_g values calculated with $\Delta = -0.2$ eV and $\Delta = 0.138$ eV. The calculated V_g might be larger than the effectively measured threshold voltage shift as not all induced charge carriers will contribute to the charge transport. However, the results for $\Delta = 0.138$ eV, corresponding to the position of the additional peak observed in the DOS [27], describe better the experimental results.

6.4.2 Pentacene as a stack of dielectric layers

An alternative calculation is presented by Horowitz [129] where the semiconductor is treated like a stack of dielectric layers of thickness $d = 1.5$ nm, *i.e.* the monolayers: The (areal) charge density in the ith layer is σ_i and by applying the Gauss law at layer i we get

$$V_{i-1} - V_i = \sigma_i \frac{d}{\epsilon_0 \epsilon_r} \tag{6.9}$$

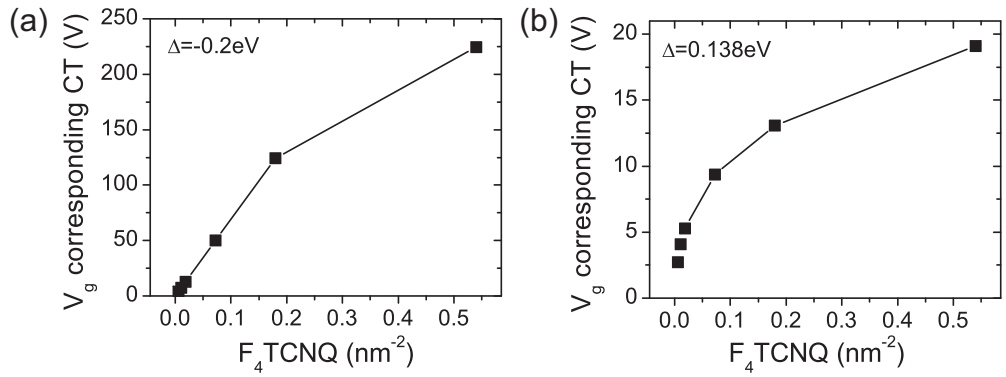

Figure 6.15: Gate voltage V_g which would be needed to apply to induce the same number of charge carriers as by charge transfer with 0.18 nm^{-2} F_4TCNQ surface doping.

where V_0 – the surface potential at the semiconductor-insulator respectively the semiconductor-dopant interface,
V_i – the potential at the interface between the ith and the $i+1$th monolayer, and
σ_i – the (areal) charge density in the ith layer.

σ_i follows from the above described DOS for $E_V = eV_i$ as

$$\sigma_i = \int_{-\infty}^{\infty} \frac{1}{\mathrm{e}^{\frac{E_F - E}{k_B T}} + 1} \left(D_{\mathrm{Gauss}}(E) + D_{exp}(E) \right) \Big|_{E_V = eV_i} . \tag{6.10}$$

Charge neutrality gives

$$\sum_{i=1}^{n} \sigma_i = V_g C_{ox} \tag{6.11}$$

respectively for surface doping

$$\sum_{i=1}^{n} \sigma_i = n_{\mathrm{molecules}} \frac{1}{\mathrm{e}^{\frac{\Delta + eV_0 - E_F}{k_B T}} + 1} \tag{6.12}$$

where n is the total number of monolayers and V_n is set to zero, so that the complete potential falls off within the monolayer. From these equations the charge density and potential for each layer can be numerically calculated (see also Appendix D for the detailed calculations).

Figure 6.16 shows the carrier density in the different monolayers for an applied gate voltage V_g of -10 V and -30 V respectively. The total thickness of pentacene corresponds to 3 MLs ($n = 3$). For $V_g = -30$ V clearly most of the charge carriers are in the first monolayer. This decay is less pronounced but still visible for $V_g = -10$ V. This dependence on the gate voltage is also observed in Ref. [129]. Monte-Carlo simulations in Ref. [135] show comparable results for the charge carrier density with distance from

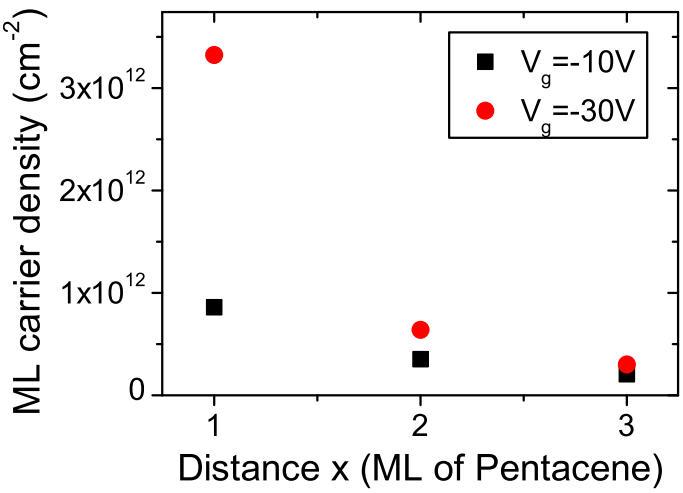

Figure 6.16: Carrier density in each ML in undoped pentacene with increasing distance x from the semiconductor-insulator interface for a gate voltage V_g of -10 V (black) and -30 V (red) respectively. The total semiconductor pentacene thickness corresponds to 3 MLs.

the insulator.

In Figure 6.17 the carrier density in the different pentacene monolayers next to the surface is shown for a F_4TCNQ surface doping concentration of 0.18 nm^{-2}. The total pentacene thickness is 3 MLs. No matter which value is chosen for Δ, most of the induced charge carriers reside in the first monolayer next to the surface. The decrease of charge carrier density with increasing pentacene thickness is shaper than found for the continuous calculations presented in Figure 6.13(c). Figure 6.18 illustrates the carrier density in the monolayer furthest away from the surface-doping interface for increasing surface doping concentration and for a total thickness of the pentacene of 1 ML, 2 ML and 3 ML. The result does not significantly differ from the carrier distribution in the different monolayers of the 3 ML thin pentacene as presented in Figure 6.17. We see again at low surface doping concentration a strong increase in the carrier density with increasing surface doping concentration and a saturation at larger surface doping concentration as in Figure 6.14.

6.5 Summary and conclusion

In summary, we studied the charge transfer between the molecular dopant F_4TCNQ and a highly smooth pentacene film of different thickness. Our result, the sharp decrease of the doping efficiency upon increasing the channel thickness to $\sim$ 2 MLs, indicates that the doping induced holes are confined within the one monolayer pentacene film in contact with the dopant. Additionally the sharp drop-off of the surface doping efficiency

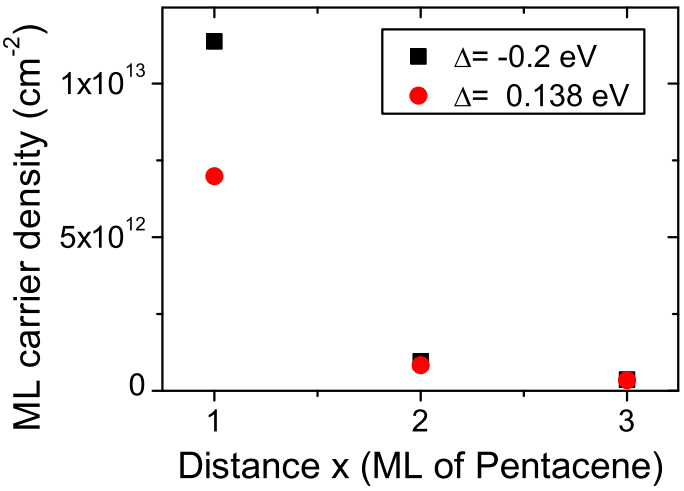

Figure 6.17: Carrier density in each ML with increasing distance x from the pentacene-dopant interface for a F_4TCNQ doping concentration of 0.18 nm^{-2}. Calculated for $\Delta = -0.2$ eV (black) and (b) $\Delta = 0.138$ eV (red) under the assumption that the pentacene consists of a stack of dielectric layers. The total semiconductor pentacene thickness corresponds to 3 MLs.

with increasing channel thickness indicates that the F_4TCNQ molecules remain on top or within the top monolayer of the pentacene film and do not interdiffuse through the different monolayers. Such interdiffusion of F_4TCNQ through the organic layers have been observed in the organic semiconductor 4,4'-bis(N-carbazolyl)biphenyl (CBP) [136]. Interdiffusion would lead to a slower decrease of the doping efficiency. The confinement of the doping induced holes within the top monolayer is confirmed by calculations both for continuous calculations on bulk pentacene and on discrete stacks of pentacene layers. This result also implies that for pentacene TFT with channel thickness above 2 MLs the doping induced charge carriers in the top pentacene monolayer do not contribute to the charge transport and that therefore the charge transport is essentially confined to the first $1-2$ MLs next to the pentacene-insulator interface. This confinement of the charge carrier at the pentacene-insulator interface, *i.e.* the accumulation thickness, is confirmed by the above calculations. Shehu *et al.* reported such confinement in the first $1-2$ ML also in transport measurements of pentacene TFTs when pentacene is deposited at low rates of 0.1 ML/min [54], which is comparable to the evaporation rate of $0.05-0.09$ ML/min for the *flat films* and the film in TFTs with MoO_x electrodes. These results imply that we have confinement of the gate induced charge carriers within the first monolayer next to the pentacene-SiO_2 interface and confinement of the surface doping induced charge carries in the top monolayer in contact with the dopants. If the electrodes provide no contact to the top monolayer, the current will flow essentially in the first monolayer and the doping induced charge carriers will not contribute to the current. Only when the channel thickness is below 2 MLs the charge density in the first

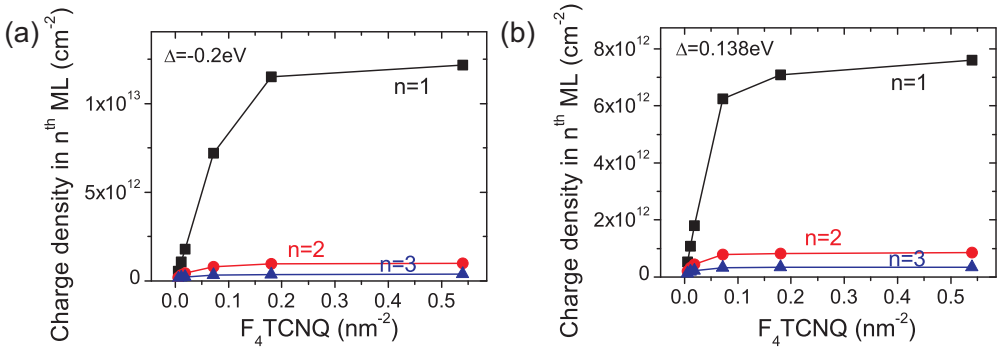

Figure 6.18: Carrier density in the lowest monolayer when surface doped with F_4TCNQ for a total pentacene thickness of 1 ML, 2 ML and 3 ML respectively. Calculated for (a) $\Delta = -0.2$ eV and (b) $\Delta = 0.138$ eV under the assumption that the pentacene consists of a stack of dielectric layers.

monolayer is sufficiently increased by the dopants to contribute to the current and thus to observe a shift of the threshold voltage $V_{g,th}$. However the current in pentacene TFTs with MoO_x electrodes was only observed to saturate at a thickness of ∼5 MLs and no saturations was observed for TFTs with Au electrodes (see Section 3.3). Whereas the non-saturation for TFTs with Au electrodes can be understood by an increasing coverage of the electrode edge with increasing pentacene film thickness and thus a lowering of the contact resistance, this should not be an issue for the MoO_x electrodes where the pentacene forms a continuous film across the electrode edge (see Section 3.2.2). The results of the current for increasing channel thickness even indicate that most of the charge transport occurs within the second monolayer away from the SiO_2 interface. From calculations the first monolayer would be expected to be most important for the charge transport, however, traps at the SiO_2 interface can both reduce the mobility and the amount of free charge carriers which again both can lead to a decrease of the charge transport in the first monolayer. A possible explanation of this discrepancy of the second monolayer being most important for the charge transport but not sensitive to surface doping, could be a less efficient charge transfer between pentacene and F_4TCNQ for larger thickness due to a possible different conformational alignment between pentacene and F_4TCNQ. However Abe *et al.* reported an increased conductance in pentacene TFTs with the top contact geometry and a channel thickness of ∼30 ML when depositing F_4TCNQ on top of the channel [28]. Therefore, the discrepancy between the observed sharp decrease of the surface doping efficiency and the saturation of the current not before 5 ML indicates that the interpretation of literature reported experiments on the spatial confinement of the field-induced carriers at the insulator-semiconductor interface of organic TFTs [52–54, 99] have to be considered with care.

CHAPTER 7

Summary and Outlook

In this thesis the deposition of guest molecules to the surface of pentacene thin film transistors (TFTs) has been employed to control the charge carrier density and to investigate the length scale of the doping induced charge transfer. For this study pentacene TFTs with channel thickness of only a few monolayers (MLs) have been successfully fabricated and characterized *in-situ* in vacuum. These thin devices enable to study and to manipulate the charge density directly in the layer where the charge transport occurs which corresponds to the first few monolayers next to the dielectric interface. The modification of the charge carrier density by simple addition of guest molecules provides a tool to investigate the charge transfer mechanism between organic semiconductors and the guest molecules.

The basis for investigating the charge transport and the effect of guest molecules in TFTs with such thin channels is controlled film growth. Smooth pentacene films on SiO_2 were achieved with a layer-by-layer growth at least up to the second monolayer when the pentacene film is deposited at low evaporation rates and the outgassed molecules are kept in vacuum during sample loading. Despite the layer-by-layer growth of pentacene on SiO_2 in the TFT channel, no continuous pentacene film growth was obtained across the edge of the Au bottom-contacts. An improved pentacene film morphology at the edge of the contact electrodes was achieved by replacing the Au electrodes with MoO_x. A simple fabrication method was applied to produce MoO_x electrodes: Mo contacts are deposited and the surface is subsequently oxidized by an O_2-plasma. Whereas with Au electrodes the contact between the pentacene film in the channel and the electrode is only bridged by elongated pentacene islands, the pentacene grows continuously across the MoO_x

electrode edge. This difference in the morphology is presumably the consequence of the different film growth on Au with respect to SiO_2 and MoO_x: the pentacene molecules are standing in an upright position on SiO_2 and on MoO_x in the so-called thin film phase whereas they are lying flat on Au. Pentacene TFTs with MoO_x contacts showed also, in comparison to TFTs with Au contacts, low contact resistance. The contact resistance values were comparable to the ones measured in F_4TCNQ doped pentacene TFTs where pentacene has been co-evaporated with the strong electron acceptor F_4TCNQ [26]. The layer-by-layer growth in pentacene TFTs with MoO_x contacts was clearly detected in the evolution of the source-drain current for increasing channel thickness: After the onset of the current at a nominal channel thickness of 0.7 ML, inflection points at completion of the first, the second and the third monolayer were observed. These inflection points directly reflect the high quality of the pentacene film and are a consequence of layer-by-layer growth and the different monolayers acting as independent channels for the charge transport due to the much lower coupling of the molecules across the monolayers than within the same monolayer.

Surface doping by the addition of guest molecules on top of the channel surface has been applied to pentacene TFTs with a channel thickness of 2.5 ML using the guest molecules F_4TCNQ, MnTPPCl, CoTPP and C_{60}. Surface doping with the acceptor molecule F_4TCNQ was shown to be highly efficient to increase the hole concentration in the pentacene TFT, manifested by a shift of the transfer curves towards positive gate voltage. Doping with F_4TCNQ is thus possible without the incorporation of the dopants into the pentacene matrix. Surface doping with MnTPPCl decreased the hole density and acted thus opposite to F_4TCNQ. The guest molecules CoTPP and C_{60} did not modify the transport characteristics of the pentacene TFT. It is an interesting finding that despite the similar electronic structure of the two porphyrins MnTPPCl and CoTPP, only surface doping with MnTPPCl had an influence on the transport characteristics. The observed doping effect of MnTPPCl is tentatively associated to its dipole moment, due to the absence of any evidence for a charge transfer between pentacene and MnTPPCl in X-ray photoelectron spectroscopy (XPS) measurements. Notably, such a dipole moment is absent in CoTPP. In contrast to MnTPPCl, XPS measurements showed that a charge transfer occurs between pentacene and F_4TCNQ which leads to an increase of the hole density in the pentacene channel. The mobility was not significantly altered by surface doping which shows that the change of the pentacene film quality with surface doping is minimal. This property makes surface doping a suitable tool to investigate the doping capabilities of various guest molecules. This is in contrast to the case of bulk doping, by co-evaporation of the organic semiconductor and the guest molecules, the guest molecules change the molecular arrangement within the organic semiconductor. Such rearrangements are expected to affect the transport properties even without the occurrence of a doping induced modification of the charge carrier

density. These experiments therefore showed that the surface doping can be highly efficient to modify the performance of organic semiconductor devices in the nanoscale. The fact that the detailed molecular structure crucially determines the doping effect highlights the enormous potential of realizing functional organic semiconductor devices engineered by chemical tuning of guest molecules.

Whereas surface doping is highly efficient to modify the charge carrier density in the pentacene channel, its effect on the contact resistance is minor. The contact resistance decreased by a maximum of 50% after F_4TCNQ surface doping of a pentacene TFT with a channel thickness of only 0.8 ML. For channel thickness of 1 ML and above the decrease is less than 20%. This effect is much smaller than the reduction by more than one order of magnitude as observed in pentacene TFT bulk doped with F_4TCNQ [26]. This may indicate that the dopants have to be at the interface between the contacts and the organic semiconductor to efficiently reduce the contact resistance. However, lower contact resistances were measured for the pristine TFTs, especially for the TFT with MoO_x contacts, compared to the pristine TFTs of the bulk doping study. This might indicate that the charge injection from the contacts to the pentacene channel in the here presented TFTs is already efficient and little further reduction of the contact resistance can be achieved by doping. Here, the barrier height, which can be extracted from temperature dependent transport measurements, would provide further information: is the observed smaller contact resistance with MoO_x compared to Au electrodes due to a better morphology or due to a better energy alignment and is the slightly reduced contact resistance by surface doping the effect of a lowered injection barrier.

The method of surface doping also allows to study the length scale of the charge transfer between the dopants and the organic semiconductor. As discussed in the introduction, the models describing the doping process in inorganic semiconductors are not necessarily valid for organic semiconductors due to the van der Waals interaction in comparison to the covalent bonding. The doping induced charge carriers are therefore expected to be more localized to the dopants. This length scale was investigated by varying the channel thickness in F_4TCNQ surface doped pentacene TFTs where the above stated layer-by-layer growth of the pentacene is the basis for such a study. The surface doping efficiency strongly drops when increasing the channel thickness from 1 to 2 monolayers and is only marginal for a channel thickness of 2.5 monolayers and above. These results demonstrate that the surface doping induced charge carriers are essentially localized to the top pentacene monolayer at the surface. Additionally these results indicate that the F_4TCNQ molecules remain at the surface and do not diffuse through the pentacene monolayers. Notably, a slower decrease of the surface doping efficiency was observed when the pentacene film grew in islands. In these rough films a still finite surface doping efficiency is measured for channel thickness of 10 ML due to $0-2$ ML regions within which surface doping can be effective. This indicates the impor-

tance of the film morphology for such studies. Calculations starting from the Poisson equation and assuming a gaussian density of states with exponential tail, indicate that both the surface doping and gate voltage induced charge carriers are confined within the first monolayer next to the surface and to the dielectric interface, respectively. Notably, the source-drain current was only observed to saturate at a channel thickness of 5 monolayers for TFTs with MoOx electrodes and no saturation was observed up to this thickness for TFTs with Au contacts. The non-saturation for TFTs with Au contacts can be partially understood by a decreasing contact resistance due to an increasing coverage at the Au-electrode edge. Further the measurements of the source-drain current for increasing channel thickness indicate that most of the charge transport occurs in the second monolayer from the dielectric / organic semiconductor interface. Notably, traps at the SiO_2 interface can reduce the mobility and free charge carrier density in the first monolayer and therefore make the second monolayer most important for the charge transport. These results are in discrepancy with the observed sharp decay of the surface doping efficiency after the first monolayer. Possible explanation for this discrepancy could be a less efficient charge transfer between F_4TCNQ and pentacene due to a possibly different molecular arrangement between organic semiconductor and the dopants deposited on two or more monolayer thick pentacene films with respect to one monolayer thick films. Otherwise the interpretation of a confinement of the field induced charge carrier within the first few monolayers based on measurements of the current versus channel thickness might be reconsidered. The occurrence of a variation of the charge transfer efficiency between F_4TCNQ and pentacene as function of the underlying pentacene film thickness could be investigated by photoelectron spectroscopy as a surface sensitive method.

By the controlled pentacene film growth both in the channel and at the MoO_x contact edge, as developed in this PhD work, and also based on the low contact resistance, it would be interesting to study charge transport in TFTs with channel lengths in the order of 1 μm which is smaller than the average pentacene grain size. The lack of grain boundaries in such small channels might give rise to higher mobilities. The here discussed surface doping both provides an alternative way for doping of organic semiconductors as well as a tool to study the processes underlying the doping in organic semiconductors. The presented results, especially the localization of the surface doping induced charge carriers to the top surface layer, are of importance to the design of doped organic semiconductor devices. For chemical sensors based on organic TFTs, in particular where the analyte is in contact with the sensor only at its surface, the sensitivity might also depend on the thickness of the active sensor material. The here gained knowledge of surface doping in organic TFTs with channel thickness in the limit of a few monolayers and the, by some of my colleagues and with my contribution, studied influence of external ligands on the magnetic exchange interaction of transition-metal

complexes on ferromagnetic substrates, might also be of importance for future spintronic devices. In such devices the dopant/ligand might modify not only the charge but also the spin current.

APPENDIX A

Beamtime experiments on "On-surface magnetochemistry"

Some of my colleagues in the research group investigate the magnetic exchange interaction of paramagnetic transition-metal complexes, *e.g.* metallo-porphyrins and -phthalocyanines (Pc), on ferromagnetic substrates. To explore the electronic and magnetic properties in such systems, element specific X-ray absorption spectroscopy (XAS) and X-ray magnetic circular dichroism (XMCD) [137] measurements are performed at the Surface/Interface: Microscopy (SIM) beamline of the Swiss Light Source (SLS) [138]. Such beamtime experiments involve the preparation of well characterized multi-layer samples (typically during the day) before experiments with synchrotron photons can be performed at the beamline (typically during the night). This kind of research depends on the whole team interacting with each other. In parallel to the main research topic of my PhD thesis I regularly contributed to the sample preparation and characterisation during such beamtime sessions, typically about three to four times a year for about 10 days.

In this coordinated effort, I was mostly responsible for the sample preparation which includes in a first step the cleaning of the single crystal substrate by Argon sputtering and thermal annealing. In a second preparation step, a ferromagnetic film, usually Co or Ni, has been deposited by e-beam evaporation. As an alternative to clean ferromagnetic substrates, oxygen reconstructed ferromagnetic films are sometimes used for the characteristic modification of the exchange coupling they bring along [127]. The last step in the sample preparation involves the deposition of one or more types of molecules by sequential or co-deposition. After each step the sample is controlled by XPS for its cleanliness, the thickness of the metal film, the presence and quality of the oxygen

induced surface reconstruction (if applicable), and the molecular coverage as well as for the correct stoichiometry. The samples are then transferred to the XMCD endstation at the SLS-SIM beamline with a vacuum suitcase [118, 127].

Here typically my colleagues have performed photoabsorption and X-ray magnetic dichroism experiments which focused at the relative magnetization of the spins of the metallic center atom of the molecular complex and the different substrates. By dosing gaseous ligands like NO and NH_3 magneto-chemical reactions were used to modify the spin system. In complex series of experiments conclusions on these spin systems as well as on their exchange coupling to the substrate could be drawn. Thereby I have contributed to a significant number of research – on paramagnetic molecular semiconductors – which nicely complemented to the core topic of my PhD work in Organic Electronics.

Specifically, by NO dosing, the spin of CoTPP/Ni got quenched and the spin of FeTPP/Ni and MnTPP/Co got significantly modified *i.e.* from ferromagnetic to antiferromagnetic alignment to the substrate magnetization in the latter case. NH_3 dosing of MnPc/Co reduced the exchange coupling strength [119]. A self-assembled molecular spin array has been demonstrated by co-evaporation of perfluorinated iron-phthalocyanine ($FeF_{16}Pc$) and MnPc on oxygen reconstructed Co. In the initial state the spins in $FeF_{16}Pc$ and MnPc are antiferromagnetically aligned with the substrate corresponding to a so-called *ON/ON* state. Dosing of NH_3 quenches the spin in $FeF_{16}Pc$ while modifying the spin of MnPc which corresponds to a so called *OFF/ON'* state. The initial *ON/ON* state can be restored by thermal desorption of NH_3. The spin states could therefore be controlled by the ligand coordination reaction, selectively switching off half of the spins in the chessboard lattice [120]. Besides switching the spin off with external ligands such as NO or NH_3, we also demonstrated that in NiPc on Co the initial spin-off state could be switched to spin-on by the external ligand NH_3 [121]. A magnetic moment can not only be induced for porphyrins and phthalocyanines, but we could also demonstrate that a magnetic moment is induced in a non-planar and non-aromatic Co(II)-complex adsorbed on a ferromagnetic Ni substrate [139]. Notably these results were among the first to compare the well established magneto-chemistry as it is known from liquid or gas chemistry with the ‘on-surface’ analogue. This comparison revealed characteristic differences between those ligands, which are well established by chemical sciences as *e.g.* NO, NH_3, and the surface substrate which also takes the role of a ligand here and sometimes acts in good agreement but also in complex modification of what has been expected.

APPENDIX B

Gas exposure of pentacene thin film transistors

Following the successful surface doping with different molecules, the interest emerged to see the effect of gases such as NO and NH_3 on phthalocyanine (Pc) or porphyrin in transport measurements. In our group the magnetochemistry of different metallo-porphyrin and -phthalocyanine monolayers on magnetic substrates was studied. Coordination of the metallo-porphyrins or -phthalocyanines with NO or NH_3 can modify the substrate induced molecular magnetic moments and the magnetic exchange interaction between molecule and substrate [118–121] (see also short summary above in Appendix A). We wanted therefore to investigate the effect of NO and NH_3 on transport measurements in thin films measured via the thin film transistor set-up as it has been described in the main part of this thesis. We fabricated TFTs with CoPc, MnPc and NiPc as the active channel material. Mobilities in such TFTs were in the order of $10^{-5} - 10^{-3}$ cm^2/Vs, much lower than in pentacene TFT. NO dosing did not induce any shift of the threshold voltage for these devices. The mobility of CoPc TFT remained constant up to the maximum NO dosing of 10^6 Langmuir (16min 40sec at 1.4×10^{-3} mbar). The mobility (conductance) of MnPc decreased with increasing NO dosing and dropped to almost zero at a dose of 5×10^5 Langmuir (8min 20sec at 1.4×10^{-3} mbar). Dosing 5×10^4 Langmuir of NO (8min 20sec at 1.4×10^{-4} mbar) on NiPc TFT decreased the mobility by about a factor of two. This decrease of the mobility (or conductance) is rather surprising as there are reports about an increase in conductance in NO gas sensors based on metallo-phthalocyanine chemiresistors (among them also NiPc) upon NO dosing [140–142]. An increased conductance would be expected due to the generation of holes created by the adsorbed oxidizing molecules [140]. By measuring NiPc TFT in NH_3 atmosphere at 10^{-4} mbar, we observed a decreased mobility by about a factor

of three. The threshold voltage shifted from −14 V to −22 V. Additionally we found that F_4TCNQ surface doping shifts also the threshold voltage of CoPc and NiPc TFTs towards positive voltage. No conductive device could be obtained with the porphyrin CoTPP. We therefore dosed NO on a pentacene TFT surface doped with MnTPPCl. The NO dosing did not shift the threshold voltage. The mobility seemed to increase slightly but only in the order of 10%.

APPENDIX C

Runsheets

n°	Processes	Description
A	Thermal oxidation	Provide 150 nm of thermal oxide
B	PAD Photolithography	Patterning of metallic pads
C	Metallization	Deposition of metallic pads
D	Backside metallization	Backside metallization for gate
E	Wafer sawing	Saw wafer in 7x7 mm pieces
F	OPENING Photolithography	Open windows on resist over channel+pads
G	Plasma cleaning	Clean the channel surface
H	Wire bonding	Gluing of the chip on the chip carrier + wire-bonding
I	Deposition of molecules	In-situ deposition and characterization

A: Thermal oxidation

	Process	Conditions	Parameters
0. Wafer cleaning and oxide removal			
0.1	Piranha etch	solution	2 H_2SO_4 : 1 H_2O_2
		time	10 min.
		temperature	90°C
0.2	water flushing		
0.3	oxide removal	solution	5% HF
		time	1 min.
0.4	water flushing		
0.5	drying	with nitrogen	
1. Dry thermal oxidation			
1.1	Dry thermal oxidation	temperature	1050°C
		time (under O_2)	150min

B: PAD Photolithography

	Process	Conditions	Parameters
1	Wafer cleaning	Ac, IP, spin drying	
2	Pre-bake	temp - time	160°C - 60 s
3	Primer	primer	TI prime
		rpm - krpm/s	4000 - 1
		time	60 s
4	Softbake	temp - time	120°C - 1 min
5	spin coating	resist	LOR5B
		rpm - krpm/s	3000 - 1
		time	60 s
6	Softbake	temp - time	160°C - 5 min
7	spin coating	resist	S1813
		rpm - krpm/s	4000 - 3
		time	30 s
8	Softbake	temp - time	115°C - 90 sek
9	Align mask		
10	Exposure	mode	soft-contact
		time	11 s
11	Development	developer	MF-24A
		time	25s
12	Water flushing		
13	Spin drying		

C: PAD metallization

	Process	Conditions	Parameters
0. Resist residues			
0.1	O_2-plasma	O_2-plasma	10sccm O_2; 100W; 100 mTorr; 300 K
		time	30 sec
1.a Metall deposition (Au) - Balzers BAK 600			
1.1	sticking layer	metal	Ti
	(without rotation)	thickness	10 nm
		rate	1 A/sec
1.2	contact layer	metal	Au
	(with rotation)	thickness	100 nm
		rate	4 A/sec
1.b Metall deposition (Mo) - sputter-deposition Nordiko			
1.1	contact layer	metal	Mo
		thickness	100 nm (measured: 70 nm)
		Ar pressure	2 mtorr
		plasma	320 V, 1.5 A
		time	7 min 45 sec
2. Lift-off			
2.1	Lift-off	remover	NMP
2.2	Water flushing		
2.3	Spin drying	spin drying	

D: Backside metallization

	Process	Conditions	Parameters
1. Frontside Protection			
1.1	spin coating	resist	s1828
		rpm - krpm/s	3000 - 4
		time	30 s
1.2	Softbake	temp - time	110°C - 90 s
1.3	Backside exposure	mode	no mask
		time	30 - 60 sec
1.4	Development	time	60 s
1.5	Water flushing		
1.6	Spin drying		
2. Oxide removal			
2.1	Oxide removal	BOE	
		time	3min
3. Backside metallization - Balzers BAK 600			
3.1	Al metallization	metal	Al
		thickness	250 nm
		rate	7 A/sec
3.2	Ti metallization	metal	Ti
		thickness	50 nm
		rate	1-2 A/sec

Do not remove the resist (protection for sawing)

F. OPENING Photolithography : in PROCESS LAB

	Process	Conditions	Paremeters
1	chip cleaning	Remover, water flush, N_2	
2	spin coating	resist	LOR5B
		rpm - krpm/s	3000 - 1
		time	60 s
3	Softbake	temp - time	170°C - 60 s
4	spin coating	resist	S1828
		rpm - krpm/s	3000 - 4
		time	30 s
5	Softbake	temp - time	95°C - 6 min
6	Backside Exposure	no mask	
		time	60 s
7	Edge Exposure	mask with 6x6 mm pieces	
		time	6-10 min
8	Align mask : OPENING		
9	Exposure	mode	
		time	20 s
10	Development	time	30 s
11	Water flushing and N2 drying		

G. Plasma cleaning

1	O_2-plasma	O_2-flow	10sccm O_2
		power	100 W
		pressure	100 mTorr
		temperature	300 K
		time	60 sec

APPENDIX D

Calculations - Details

D.1 Calculations on bulk pentacene

Here the Mathematica code used for the calculations on bulk pentacene based on the Poisson equations is presented. The results of these calculations are discussed in Section 6.4.1.

D.1.1 Gate induced charge carriers

The following Mathematica code is for an applied gate voltage V_g of -10 V. The same code was applied for $V_g = -30$, with the corresponding parameter changed to -30 V.

$$\mathbf{DOSgauss[Vx\_, N\_, Vv\_, sigma\_]:=}\frac{\mathbf{NExp}\left[-\left(\frac{\mathbf{Vx-Vv}}{\sqrt{\mathbf{2}}\ \mathbf{sigma}}\right)^{\mathbf{2}}\right]}{\frac{\sqrt{\mathbf{2}\pi}\ \mathbf{sigma}\ \mathbf{1.602176565}}{\mathbf{10^{19}}}}$$

$$\mathbf{fermi4[Vn\_, Vf\_]:=1/(Exp[-(Vn-Vf)/0.0265]+1)}$$

$$\mathbf{DOSexp2(Vx\_, N\_, T0\_, Vv\_):=}\frac{\mathbf{N}\exp\left(-\frac{\mathbf{Vx-Vv}}{\frac{\mathbf{8.61733T0}}{\mathbf{10^5}}}\right)}{\frac{\mathbf{8.617331.60218T0}}{\mathbf{10^5 10^{19}}}}\mathbf{/;Vx-Vv\geq 0}$$

$$\mathbf{DOSexp2[Vx\_, N\_, T0\_, Vv\_]:=0/;(Vx-Vv)<0}$$

$$\mathbf{Ngauss = 2.9*\hat{}27}$$

$$\mathbf{T0 = 1330}$$

Nexp = 3.6*^24

sigma = 0.07

eps = 4 * 8.854 * 10^ - 12

Vg = 10

Ci = 2.3000 * 10^ - 4

q = 1.602176565 × 10^ - 19

**efield[Vs_?NumericQ]:=Sqrt[2/eps * q*NIntegrate[fermi4[x, Ef]*
(DOSgauss[x, NN, V, ss] + DOSexp2[x, Nexp, T0, V]) * q/.
{Ef → 1, NN → Ngauss, ss → 0.5sigma}, {V, 0, Vs}, {x, −Infinity, V}]]**

sol = FindRoot[Ci * Vg/eps == efield[Vs], {Vs, 0.9}]

{Vs → 0.904678}

Vss = Vs/.sol

0.904678

inv[f_, s_, x0_]:=Function[{t}, s/.FindRoot[f − t, {s, x0}]]

potential2 = inv[NIntegrate[1/efield[VV], {VV, Vx, Vss}], Vx, 0.9]

Plot[potential2[x], {x, 0, 1*^-8}]

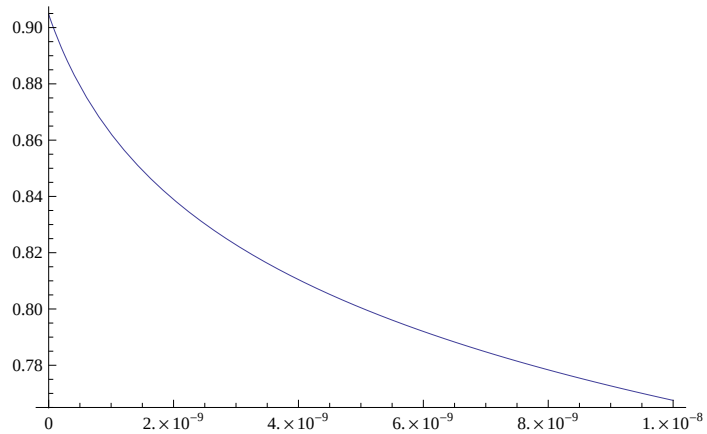

```
densityV[V_?NumericQ]:=NIntegrate[fermi4[vv, 1]*
(DOSgauss[vv, Ngauss, V, 0.5sigma] + DOSexp2[vv, Nexp, T0]) * q,
{vv, -Infinity, V}]

density[x_?NumericQ]:=NIntegrate[fermi4[vv, 1]*
(DOSgauss[vv, Ngauss, vvv, 0.5sigma] + DOSexp2[vv, Nexp, T0]) * q,
{vv, -Infinity, vvv}]/.{vvv->potential2[x]}

LogPlot[density[x], {x, 0, 20*^-9}, PlotPoints → 20, MaxRecursion → 0]
```

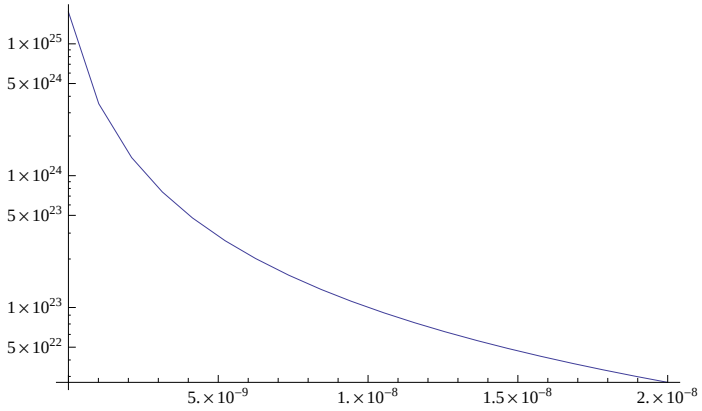


```
ListLogPlot[Table[{x, eps/q*
(efield[potential2[x * 1.5*^-9]] - efield[potential2[(x + 1) * 1.5*^-9]])},
{x, 0, 20}]](*difference of integrated carrier density from infinity
to xth resp. (x + 1)th monolayer -> total carrier density in xth ML *)
```

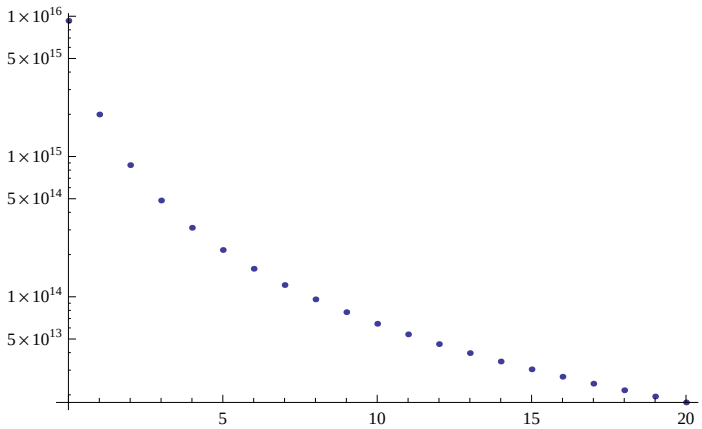

NIntegrate[densityV[V]/efield[V], {V, 0, Vss}]/density[0]

(*total integrated carrier density over carrier density at the surface (x = 0) −> thickness of the accumulation layer*)

8.228186041857557*^-10

Ci∗Vg/q/density[0]

(*total induced carrier density over carrier density at the surface (x = 0) −> thickness of the accumulation layer*)

8.228176490960225*^-10

D.1.2 Doping induced charge carriers

The following Mathematica code is for doping induced charge carriers and an energy difference Δ, between the LUMO level of the dopant and the HOMO of pentacene, of 0.138 eV. The same code was applied for $\Delta = -0.2$ eV, with the corresponding parameter changed to -0.2 eV.

$$\mathbf{DOSgauss[Vx\_, N\_, Vv\_, sigma\_]:=}\frac{\mathbf{NExp}\left[-\left(\frac{\mathbf{Vx-Vv}}{\sqrt{2}\ \mathbf{sigma}}\right)^{2}\right]}{\frac{\sqrt{2\pi}\ \mathbf{sigma}\ 1.602176565}{10^{19}}}$$

$$\mathbf{fermi4[Vn\_, Vf\_]:=1/(Exp[-(Vn - Vf)/0.0265] + 1)}$$

$$\mathbf{DOSexp2(Vx\_, N\_, T0\_, Vv\_):=}\frac{\mathbf{N}\exp\left(-\frac{\mathbf{Vx-Vv}}{\frac{\mathbf{8.61733T0}}{10^{5}}}\right)}{\frac{\mathbf{8.617331.60218T0}}{\mathbf{10^{5}10^{19}}}}\mathbf{/;Vx - Vv \geq 0}$$

$$\mathbf{DOSexp2[Vx\_, N\_, T0\_, Vv\_]:=0/;(Vx - Vv) < 0}$$

$$\mathbf{Ngauss = 2.9*\hat{}27}$$

$$\mathbf{T0 = 1330}$$

$$\mathbf{Nexp = 3.6*\hat{}24}$$

$$\mathbf{sigma = 0.07}$$

$$\mathbf{eps = 4 * 8.854 * 10\hat{} - 12}$$

$$\mathbf{q = 1.602176565 \times 10\hat{} - 19}$$

Ci = 2.3000 * 10^ - 4

nA = 1.8*^17

D2 = 0.138

**efield[Vs_?NumericQ]:=Sqrt[2/eps * q*NIntegrate[fermi4[x, Ef]*
(DOSgauss[x, NN, V, ss] + DOSexp2[x, Nexp, T0, V]) * q/.
{Ef → 1,NN→ Ngauss,ss→0.5sigma}, {V, 0, Vs},{x, −Infinity, V}]]**

sol = FindRoot[nA * q * (1 − fermi4[Vs + D2, 1])/eps == efield[Vs], {Vs, 0.9}]
{Vs → 0.919009}

Vss = Vs/.sol
0.919009

conc = {0.03, 0.06, 0.1, 0.4, 1, 3}

**Vslist = Table[FindRoot[k * nA * q * (1 − fermi4[Vs + D2, 1])/eps
==efield[Vs], {Vs, 0.9}],{k, conc}]**
{{Vs → 0.835859}, {Vs → 0.857231}, {Vs → 0.870544}, {Vs → 0.901062},
{Vs → 0.919009}, {Vs → 0.939582}}

**potentialb[x_?NumericQ, Vs_?NumericQ]:=
Vx/.FindRoot[NIntegrate[1/efield[VV], {VV, Vx, Vs}] == x, {Vx, 0.9}]**

inv[f_, s_, x0_]:=Function[{t}, s/.FindRoot[f − t, {s, x0}]]

potential2 = inv[NIntegrate[1/efield[VV], {VV, Vx, Vss}], Vx, 0.9]

Plot[potential2[x], {x, 0, 1*^-8}]

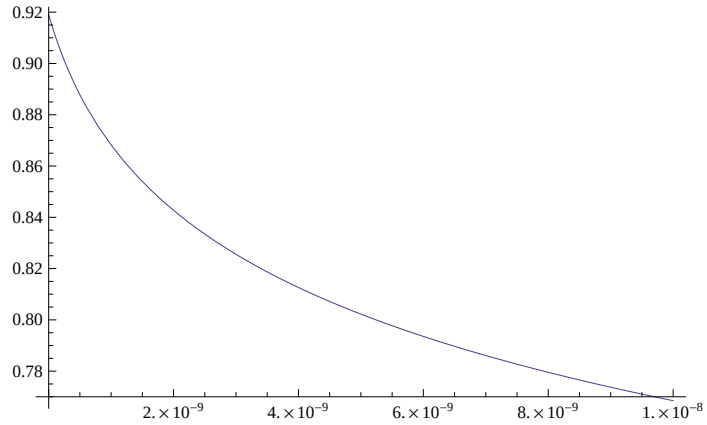

densityV[V_?NumericQ]:=NIntegrate[fermi4[vv, 1]∗

(DOSgauss[vv, Ngauss, V, 0.5sigma] + DOSexp2[vv, Nexp, T0]) ∗ q,

{vv, −Infinity, V}]

density[x_?NumericQ]:=NIntegrate[fermi4[vv, 1]∗

(DOSgauss[vv, Ngauss, potential2[x], 0.5sigma] + DOSexp2[vv, Nexp, T0]) ∗ q,

{vv, −Infinity, potential2[x]}]

LogPlot[density[x], {x, 0, 20*^-9}, PlotPoints → 20, MaxRecursion → 0]

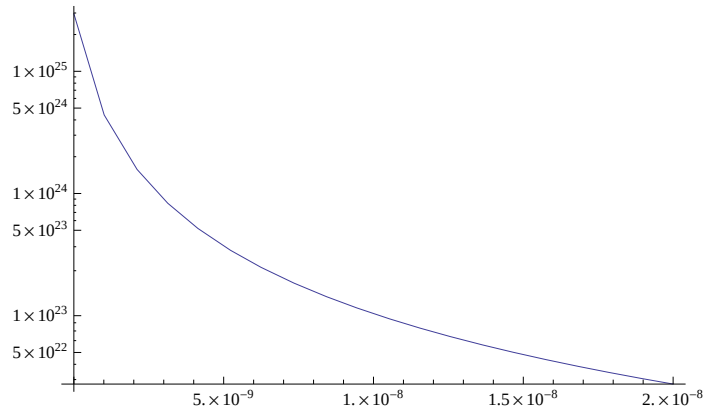

ListLogPlot[Table[

{x, eps/q ∗ (efield[potential2[x ∗ 1.5*^-9]] − efield[potential2[(x + 1) ∗ 1.5*^-9]])},

{x, 0, 20}]](*difference of integrated carrier density from infinity

to xth resp. (x + 1)th monolayer − > total carrier density in xth ML *)

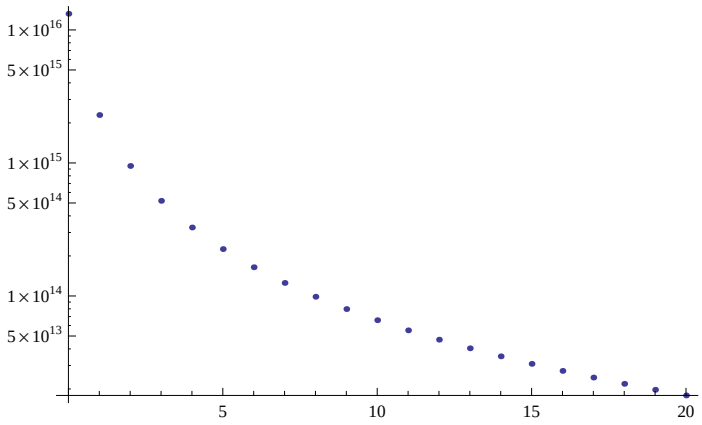

ListPlot[Table[Transpose[{conc,Table[

eps/q ∗ (efield[potentialb[x ∗ 1.5*^-9, Vs]]−

efield[potentialb[(x + 1) ∗ 1.5*^-9, Vs]]), {Vs, Vs/.Vslist}]}], {x, 0, 3}]]

(*evolution of charge density in 1st, 2nd,

3rd and 4th monolayer for different doping concentrations *)

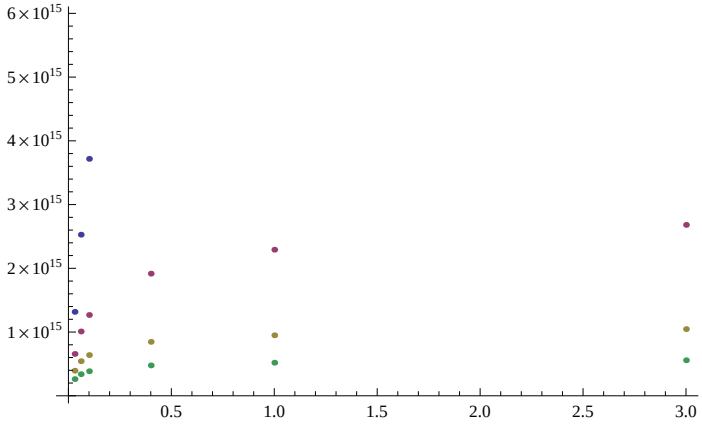

ListPlot[Transpose[

{conc, conc ∗ q ∗ nA ∗ (1 − fermi4[Evaluate[Vs/.Vslist] + D2, 1])/Ci}]]

(*gate voltage to apply to get same charge density per area as with surface doping *)

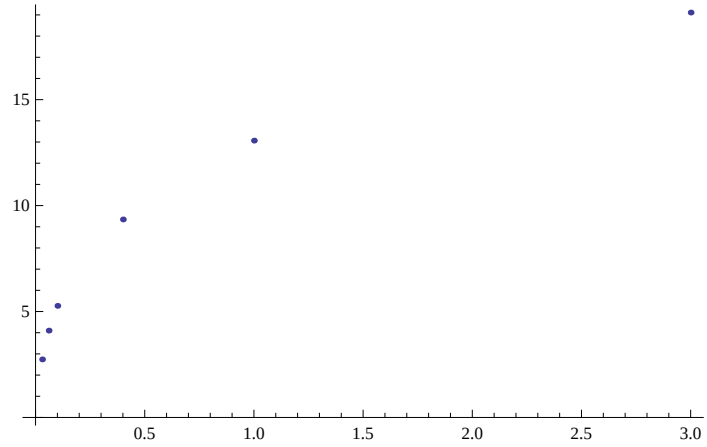

NIntegrate[densityV[V]/efield[V], {V, 0, Vss}]/density[0]

(*total area density over surface charge density gives thickness of accumulation layer, eg x * (surface − density) = (total density per area)*)

6.333264271533345*^-10

nA * (1 − fermi4[Vss + D2, 1])/density[0]

(* same as above but different way to calculate *)

6.333257572874303*^-10

eps/q * efield[Vss]/density[0]

(* same as above but different way to calculate *)

6.333257572874361*^-10

D.2 Calculations on pentacene as a stack of dielectric layers

Here the Mathematica code used for the calculations on pentacene as a stack of dielectric layers is presented. The results of these calculations are discussed in Section 6.4.2.

$$\mathbf{DOSgauss[Vx\_, N\_, Vv\_, sigma\_]:=}\frac{\mathbf{NExp}\left[-\left(\frac{\mathbf{Vx-Vv}}{\sqrt{\mathbf{2}}\mathbf{sigma}}\right)^{\mathbf{2}}\right]}{\frac{\sqrt{\mathbf{2}\pi}\mathbf{sigma1.602176565}}{\mathbf{10^{19}}}}$$

$$\mathbf{DOSexp2(Vx\_, N\_, T0\_, Vv\_):=}\frac{\mathbf{N}\exp\left(-\frac{\mathbf{Vx-Vv}}{\frac{\mathbf{8.61733T0}}{\mathbf{10^5}}}\right)}{\frac{\mathbf{8.617331.60218T0}}{\mathbf{10^5 10^{19}}}}\mathbf{/;Vx-Vv\geq 0}$$

DOSexp2[Vx_, N_, T0_, Vv_]:=0/;(Vx − Vv) < 0

fermi4[Vn_, Vf_]:=1/(Exp[−(Vn − Vf)/0.0265] + 1)

Ngauss = 2.9*^27

T0 = 1330

Nexp = 3.6*^24

sigma = 0.07

eps = 4 ∗ 8.854 ∗ 10^ − 12

Vg = 10

Ci = 2.3000 ∗ 10^ − 4

q = 1.602176565 × 10^ − 19

d = 1.5*^-9

kT = 0.0265

nA = 1.8*^17(*1.8nm^ − 2, 1HzF4TCNQ*)

D2 = 0.138

For $\Delta = 0.138$ eV, changed accordingly for $\Delta = -0.2$ eV

conc = {0.03, 0.06, 0.1, 0.4, 1, 3}

densityExpEf[V_?NumericQ, eff_?NumericQ]:=NIntegrate[fermi4[vv, eff]∗
(DOSgauss[vv, Ngauss, V, 0.5sigma] + DOSexp2[vv, Nexp, T0, V])∗
q,{vv, −Infinity, V}, MaxRecursion → 15]

For a total thickness of 3 monolayers, charge carriers induced by surface doping:

listD2 =Table[FindRoot[
{V0 − V1 == s1 ∗ d/eps, V1 − V2 == s2 ∗ d/eps, V2 − V3 == s3 ∗ d/eps,

s1 + s2 + s3 == k * nA * q * (1 − fermi4[V0 + D2, eef]),

s1==q * densityExpEf[V1, eef],

s2==q * densityExpEf[V2, eef], s3==q * densityExpEf[V3, eef], V3 == 0},

{{s1, 0.0023}, {s2, 6.3*^-9}, {s3, 6.3*^-9}, {V1, 0.09}, {V2, 0.09},

{V0, 0.09}, {V3, 0.09}, {eef, 0.76}}], {k, conc}]

{{s1 → 0.000405424, s2 → 0.00026531, s3 → 0.000194442, V1 → 0.0194722, V2 → 0.00823533, V0 → 0.0366434, V3 → 0., eef → 0.715561}, { s1 → 0.000974779, s2 → 0.000464196, s3 → 0.000291376, V1 → 0.0320013, V2 → 0.0123409, V0 → 0.0732868, V3 → 0., eef → 0.704842}, { s1 → 0.00186403, s2 → 0.000654682, s3 → 0.000365205, V1 → 0.043196, V2 → 0.0154678, V0 → 0.122145, V3 → 0., eef → 0.698857}, { s1 → 0.00926414, s2 → 0.00125216, s3 → 0.000533644, V1 → 0.0756357, V2 → 0.0226018, V0 → 0.468007, V3 → 0., eef → 0.688807}, { s1 → 0.0112145, s2 → 0.0013327, s3 → 0.00055176, V1 → 0.079814, V2 → 0.0233691, V0 → 0.55479, V3 → 0., eef → 0.687922}, { s1 → 0.0120818, s2 → 0.00136454, s3 → 0.000558705, V1 → 0.0814566, V2 → 0.0236632, V0 → 0.593166, V3 → 0., eef → 0.687591}}

For a total thickness of 2 monolayers, charge carriers induced by surface doping:

listD2M2 =

Table[FindRoot[{V0 − V1 == s1 * d/eps, V1 − V2 == s2 * d/eps,

s1 + s2 == k * nA * q * (1 − fermi4[V0 + D2, eef]), s1==q * densityExpEf[V1, eef],

s2==q * densityExpEf[V2, eef], V2 == 0},

{{s1, 0.0023}, {s2, 6.3*^-9}, {V1, 0.09}, {V2, 0.09}, {V0, 0.09}, {eef, 0.76}}],

{k, conc}]

{{s1 → 0.000541915, s2 → 0.00032326, V1 → 0.0136913, V2 → 0., V0 → 0.0366434, eef → 0.70209}, { s1 → 0.00120719, s2 → 0.000523165, V1 → 0.022158, V2 → 0., V0 → 0.0732868, eef → 0.689332}, { s1 → 0.00217845, s2 → 0.000705465, V1 → 0.0298791, V2 → 0., V0 → 0.122145, eef → 0.68141}, { s1 → 0.00952797, s2 → 0.0012639, V1 → 0.0535308, V2 → 0., V0 → 0.457076, eef → 0.665958}, { s1 → 0.0112568, s2 → 0.0013343, V1 → 0.0565128, V2 →

0., V0 → 0.533278, eef → 0.664521}, { s1 → 0.0121091, s2 → 0.00136551, V1 → 0.0578344, V2 → 0., V0 → 0.5707, eef → 0.663909}}

For a total thickness of 1 monolayer, charge carriers induced by surface doping:

listD2M1 =Table[**FindRoot**[{

V0 − V1 == s1 ∗ d/eps, s1 == k ∗ nA ∗ q ∗ (1 − fermi4[**V0 + D2, eef**]),

s1==q ∗ densityExpEf[**V1, eef**], **V1 == 0**},

{{**s1, 0.0023**}, {**V1, 0.09**}, {**V0, 0.09**}, {**eef, 0.76**}}], {**k, conc**}]

{{s1 → 0.000865175, V1 → 0., V0 → 0.0366434, eef → 0.676002}, { s1 → 0.00173035, V1 → 0., V0 → 0.0732868, eef → 0.657633}, { s1 → 0.00288392, V1 → 0., V0 → 0.122145, eef → 0.644097}, { s1 → 0.00999934, V1 → 0., V0 → 0.42351, eef → 0.611147}, { s1 → 0.011361, V1 → 0., V0 → 0.48118, eef → 0.607764}, { s1 → 0.0121797, V1 → 0., V0 → 0.515855, eef → 0.60592}}

For an applied gate voltage of $V_g = -10V$ and a total thickness of 3 monolayers:

FindRoot[{**V0 − V1 == s1 ∗ d/eps, V1 − V2 == s2 ∗ d/eps**,

V2 − V3 == s3 ∗ d/eps,**s1 + s2 + s3 == Ci ∗ (10 − V0)**,

s1==q ∗ densityExpEf[**V1, eef**],**s2==q ∗ densityExpEf**[**V2, eef**],

s3==q ∗ densityExpEf[**V3, eef**], **V3 == 0**},

{{**s1, 0.0023**}, {**s2, 6.3*^-9**}, {**s3, 6.3*^-9**}, {**V1, 0.09**}, {**V2, 0.09**},

{**V0, 0.09**}, {**V3, 0.09**}, {**eef, 0.76**}}]

{s1 → 0.00138379, s2 → 0.000562757, s3 → 0.000331263, V1 → 0.0378651, V2 → 0.0140302, V0 → 0.0964738, V3 → 0., eef → 0.701442}

For an applied gate voltage of $V_g = -30V$ and a total thickness of 3 monolayers:

FindRoot[{**V0 − V1 == s1 ∗ d/eps, V1 − V2 == s2 ∗ d/eps**,

V2 − V3 == s3 ∗ d/eps,**s1 + s2 + s3 == Ci ∗ (30 − V0)**,

s1==q ∗ densityExpEf[**V1, eef**],**s2==q ∗ densityExpEf**[**V2, eef**],

s3==q ∗ densityExpEf[**V3, eef**], **V3 == 0**},

{{**s1, 0.0023**}, {**s2, 6.3*^-9**}, {**s3, 6.3*^-9**}, {**V1, 0.09**}, {**V2, 0.09**},

{**V0, 0.09**}, {**V3, 0.09**}, {**eef, 0.76**}}]

$\{s1 \to 0.00532621,\ s2 \to 0.00102871,\ s3 \to 0.000478506,\ V1 \to 0.0638364,\ V2 \to 0.0202665,\ V0 \to 0.289421,\ V3 \to 0.,\ eef \to 0.691697\}$

Bibliography

[1] Stephen R. Forrest. The path to ubiquitous and low-cost organic electronic appliances on plastic. *Nature*, **428**, 6986, 911–918 (2004). DOI:10.1038/nature02498.

[2] William S. Wong and Alberto Salleo. *Flexible Electronics - Materials and Applications*. Springer (2009). ISBN 9780387743639.

[3] Kenji Nomura, Hiromichi Ohta, Akihiro Takagi, Toshio Kamiya, Masahiro Hirano and Hideo Hosono. Room-temperature fabrication of transparent flexible thin-film transistors using amorphous oxide semiconductors. *Nature*, **432**, 7016, 488–492 (2004). DOI:10.1038/nature03090.

[4] Jin-Seong Park, Tae-Woong Kim, Denis Stryakhilev, Jae-Sup Lee, Sung-Guk An, Yong-Shin Pyo, Dong-Bum Lee, Yeon Gon Mo, Dong-Un Jin and Ho Kyoon Chung. Flexible full color organic light-emitting diode display on polyimide plastic substrate driven by amorphous indium gallium zinc oxide thin-film transistors. *Applied Physics Letters*, **95**, 1, 013503 (2009). DOI:doi:10.1063/1.3159832.

[5] Yung-Hui Yeh, Chun-Cheng Cheng, Benjamin Chih-Ming Lai, Chyi-Ming Leu and Yung-Lung Tseng. Flexible hybrid substrates of roll-to-roll manufacturing for flexible display application. *Journal of the Society for Information Display*, **21**, 1, 34–40 (2013). DOI:10.1002/jsid.140.

[6] Sony. OTFT-Driven OLED Display that can be Rolled up onto a Pen. *CX-NEWS*, **62** (2010). Published online: http://www.sony.net/Products/SC-HP/cx_news/vol62/pdf/sideview62.pdf.

[7] A. Tsumura, H. Koezuka and T. Ando. Macromolecular electronic device: Field-effect transistor with a polythiophene thin film. *Applied Physics Letters*, **49**, 18, 1210 (1986). DOI:doi:10.1063/1.97417.

[8] Christopher R. Newman, C. Daniel Frisbie, Demetrio A. da Silva Filho, Jean-Luc Brédas, Paul C. Ewbank and Kent R. Mann. Introduction to organic thin film transistors and design of n-channel organic semiconductors. *Chemistry of Materials*, **16**, 23, 4436–4451 (2004). DOI:10.1021/cm049391x.

[9] Howard E. Katz, Zhenan Bao and Sylvain L. Gilat. Synthetic chemistry for ultrapure, processable, and high-mobility organic transistor semiconductors. *Accounts of Chemical Research*, **34**, 5, 359–369 (2001). DOI:10.1021/ar990114j.

[10] Hagen Klauk. Organic thin-film transistors. *Chemical Society Reviews*, **39**, 7, 2643–2666 (2010). DOI:10.1039/B909902F.

[11] Simon M. Sze. *Physics of Semiconductor Devices*. John Wiley & Sons, New York, 2nd edition (1981). ISBN 0471056618.

[12] Zhenan Bao and Jason Locklin. *Organic Field-Effect Transistors*. CRC Press, Boca Raton, FL (2007). ISBN 9781420008012.

[13] Oana D. Jurchescu, Jacob Baas and Thomas T. M. Palstra. Effect of impurities on the mobility of single crystal pentacene. *Applied Physics Letters*, **84**, 16, 3061 (2004). DOI:doi:10.1063/1.1704874.

[14] Denis Fichou. Structural order in conjugated oligothiophenes and its implications on opto-electronic devices. *Journal of Materials Chemistry*, **10**, 3, 571–588 (2000). DOI:10.1039/A908312J.

[15] Ioannis Kymissis. *Organic Field Effect Transistors - Theory, Fabrication and Characterization*. Springer (2009). ISBN 9780387921341.

[16] B. Lüssem, M. Riede and K. Leo. Doping of organic semiconductors. *physica status solidi (a)*, **210**, 1, 9–43 (2013). DOI:10.1002/pssa.201228310.

[17] K. Walzer, B. Maennig, M. Pfeiffer and K. Leo. Highly efficient organic devices based on electrically doped transport layers. *Chemical Reviews*, **107**, 4, 1233–1271 (2007). DOI:10.1021/cr050156n.

[18] Keng-Hoong Yim, Gregory L. Whiting, Craig E. Murphy, Jonathan J. M. Halls, Jeremy H. Burroughes, Richard H. Friend and Ji-Seon Kim. Controlling electrical properties of conjugated polymers via a solution-based p-type doping. *Advanced Materials*, **20**, 17, 3319–3324 (2008). DOI:10.1002/adma.200800735.

[19] Hagen Klauk, Günter Schmid, Wolfgang Radlik, Werner Weber, Lisong Zhou, Chris D Sheraw, Jonathan A Nichols and Thomas N Jackson. Contact resistance in organic thin film transistors. *Solid-State Electronics*, **47**, 2, 297–301 (2003). DOI:10.1016/S0038-1101(02)00210-1.

[20] Antoine Kahn, Norbert Koch and Weiying Gao. Electronic structure and electrical properties of interfaces between metals and π-conjugated molecular films. *Journal of Polymer Science Part B: Polymer Physics*, **41**, 21, 2529–2548 (2003). DOI:10.1002/polb.10642.

[21] Takeo Minari, Tetsuhiko Miyadera, Kazuhito Tsukagoshi, Yoshinobu Aoyagi and Hiromi Ito. Charge injection process in organic field-effect transistors. *Applied Physics Letters*, **91**, 5, 053508 (2007). DOI:10.1063/1.2759987.

[22] Raoul Schroeder, Leszek A. Majewski and Martin Grell. Improving organic transistor performance with Schottky contacts. *Applied Physics Letters*, **84**, 6, 1004 (2004). DOI:10.1063/1.1645993.

[23] F. Fujimori, K. Shigeto, T. Hamano, T. Minari, T. Miyadera, K. Tsukagoshi and Y. Aoyagi. Current transport in short channel top-contact pentacene field-effect transistors investigated with the selective molecular doping technique. *Applied Physics Letters*, **90**, 19, 193507 (2007). DOI:doi:10.1063/1.2737418.

[24] Shree Prakash Tiwari, William J. Potscavage Jr., Tissa Sajoto, Stephen Barlow, Seth R. Marder and Bernard Kippelen. Pentacene organic field-effect transistors with doped electrode-semiconductor contacts. *Organic Electronics*, **11**, 5, 860–863 (2010). DOI:10.1016/j.orgel.2010.01.029.

[25] Jun Li, Xiao-Wen Zhang, Liang Zhang, Khizar-ul-Haq, Xue-Yin Jiang, Wen-Qing Zhu and Zhi-Lin Zhang. Improving organic transistor performance through contact-area-limited doping. *Solid State Communications*, **149**, 41–42, 1826–1830 (2009). DOI:10.1016/j.ssc.2009.07.006.

[26] Claudio Vanoni, Soichiro Tsujino and Thomas A. Jung. Reduction of the contact resistance by doping in pentacene few monolayers thin film transistors and self-assembled nanocrystals. *Applied Physics Letters*, **90**, 19, 193119 (2007). DOI:10.1063/1.2738382.

[27] Claudio Vanoni, Thomas A. Jung and Soichiro Tsujino. Temperature dependent charge-injection at the metal-organic semiconductor interface and density of states in pristine and doped pentacene. *Applied Physics Letters*, **94**, 25, 253306 (2009). DOI:10.1063/1.3159835.

[28] Y. Abe, T. Hasegawa, Y. Takahashi, T. Yamada and Y. Tokura. Control of threshold voltage in pentacene thin-film transistors using carrier doping at the charge-transfer interface with organic acceptors. *Applied Physics Letters*, **87**, 15, 153506 (2005). DOI:10.1063/1.2099540.

[29] Yusuke Wakatsuki, Kei Noda, Yasuo Wada, Toru Toyabe and Kazumi Matsushige. Molecular doping effect in bottom-gate, bottom-contact pentacene thin-film transistors. *Journal of Applied Physics*, **110**, 5, 054505 (2011). DOI:10.1063/1.3627240.

[30] S. Kobayashi, T. Nishikawa, T. Takenobu, S. Mori, T. Shimoda, T. Mitani, H. Shimotani, N. Yoshimoto, S. Ogawa and Y. Iwasa. Control of carrier density by self-assembled monolayers in organic field-effect transistors. *Nature Materials*, **3**, 5, 317–322 (2004). DOI:10.1038/nmat1105.

[31] Yunseok Jang, Jeong Ho Cho, Do Hwan Kim, Yeong Don Park, Minkyu Hwang and Kilwon Cho. Effects of the permanent dipoles of self-assembled monolayer-treated insulator surfaces on the field-effect mobility of a pentacene thin-film transistor. *Applied Physics Letters*, **90**, 13, 132104–132104–3 (2007). DOI:doi:10.1063/1.2457776.

[32] K. P Pernstich, S. Haas, D. Oberhoff, C. Goldmann, D. J Gundlach, B. Batlogg, A. N Rashid and G. Schitter. Threshold voltage shift in organic field effect transistors by dipole monolayers on the gate insulator. *Journal of Applied Physics*, **96**, 11, 6431 (2004). DOI:doi:10.1063/1.1810205.

[33] T. Ojima, M. Koto, M. Itoh and T. Imamura. Control of field-effect transistor threshold voltages by insertion of self-assembled monolayers. *Journal of Applied Physics*, **113**, 3, 034501–034501–6 (2013). DOI:doi:10.1063/1.4775785.

[34] Jürgen Ristein. Surface transfer doping of semiconductors. *Science*, **313**, 5790, 1057 –1058 (2006). DOI:10.1126/science.1127589.

[35] Wei Chen, Dongchen Qi, Xingyu Gao and Andrew Thye Shen Wee. Surface transfer doping of semiconductors. *Progress in Surface Science*, **84**, 9-10, 279–321 (2009). DOI:10.1016/j.progsurf.2009.06.002.

[36] P. Strobel, M. Riedel, J. Ristein and L. Ley. Surface transfer doping of diamond. *Nature*, **430**, 6998, 439–441 (2004). DOI:10.1038/nature02751.

[37] Jürgen Ristein. Surface science of diamond: Familiar and amazing. *Surface Science*, **600**, 18, 3677–3689 (2006). DOI:10.1016/j.susc.2006.01.087.

[38] D. P. Langley, Y. Smets, C. B. Stark, M. T. Edmonds, A. Tadich, K. J. Rietwyk, A. Schenk, M. Wanke, Q.-H. Wu, P. J. Barnard, L. Ley and C. I. Pakes. Surface transfer doping of diamond with a molecular heterojunction. *Applied Physics Letters*, **100**, 3, 032103–032103–4 (2012). DOI:doi:10.1063/1.3676445.

[39] Pengpeng Zhang, Emma Tevaarwerk, Byoung-Nam Park, Donald E. Savage, George K. Celler, Irena Knezevic, Paul G. Evans, Mark A. Eriksson and Max G. Lagally. Electronic transport in nanometre-scale silicon-on-insulator membranes. *Nature*, **439**, 7077, 703–706 (2006). DOI:10.1038/nature04501.

[40] Lin-Bao Luo, Tsz-Wai Ng, Hao Tang, Feng-Xia Liang, Yu-Cheng Dong, Jian-Sheng Jie, Chun-Yan Wu, Li Wang, Zhi-Feng Zhu, Yong-Qiang Yu and Qiang Li. Surface charge transfer doping of germanium nanowires by MoO3 deposition. *RSC Advances*, **2**, 8, 3361–3366 (2012). DOI:10.1039/C2RA01269C.

[41] G. D. Yuan, Y. B. Zhou, C. S. Guo, W. J. Zhang, Y. B. Tang, Y. Q. Li, Z. H. Chen, Z. B. He, X. J. Zhang, P. F. Wang, I. Bello, R. Q. Zhang, C. S. Lee and S. T. Lee. Tunable electrical properties of silicon nanowires via surface-ambient chemistry. *ACS Nano*, **4**, 6, 3045–3052 (2010). DOI:10.1021/nn1001613.

[42] Philip G. Collins, Keith Bradley, Masa Ishigami and A. Zettl. Extreme oxygen sensitivity of electronic properties of carbon nanotubes. *Science*, **287**, 5459, 1801 –1804 (2000). DOI:10.1126/science.287.5459.1801.

[43] Wei Chen, Shi Chen, Dong Chen Qi, Xing Yu Gao and Andrew Thye Shen Wee. Surface transfer p-type doping of epitaxial graphene. *J. Am. Chem. Soc.*, **129**, 34, 10418–10422 (2007). DOI:10.1021/ja071658g.

[44] Jing Kong, Nathan R. Franklin, Chongwu Zhou, Michael G. Chapline, Shu Peng, Kyeongjae Cho and Hongjie Dai. Nanotube molecular wires as chemical sensors. *Science*, **287**, 5453, 622 –625 (2000). DOI:10.1126/science.287.5453.622.

[45] Brian A. Gregg, Si-Guang Chen and Russell A. Cormier. Coulomb forces and doping in organic semiconductors. *Chem. Mater.*, **16**, 23, 4586–4599 (2004). DOI:10.1021/cm049625c.

[46] Ingo Salzmann, Georg Heimel, Steffen Duhm, Martin Oehzelt, Patrick Pingel, Benjamin M. George, Alexander Schnegg, Klaus Lips,

Ralf-Peter Blum, Antje Vollmer and Norbert Koch. Intermolecular hybridization governs molecular electrical doping. *Physical Review Letters*, **108**, 3, 035502 (2012). DOI:10.1103/PhysRevLett.108.035502.

[47] Alexander Mityashin, Yoann Olivier, Tanguy Van Regemorter, Cedric Rolin, Stijn Verlaak, Nicolas G Martinelli, David Beljonne, Jérôme Cornil, Jan Genoe and Paul Heremans. Unraveling the mechanism of molecular doping in organic semiconductors. *Advanced Materials*, **24**, 12, 1535–1539 (2012). DOI:10.1002/adma.201104269.

[48] Sieu Ha and Antoine Kahn. Isolated molecular dopants in pentacene observed by scanning tunneling microscopy. *Physical Review B*, **80**, 19 (2009). DOI:10.1103/PhysRevB.80.195410.

[49] Claudio Vanoni. *Electronic transport, field effect and doping in pentacene nanorods and monolayer thin film prepared by combination of nano-fabrication and self-assembly*. PhD thesis, University of Basel (2006). DOI:10.5451/unibas-004662789.

[50] C.d. Dimitrakopoulos and P.r.l. Malenfant. Organic thin film transistors for large area electronics. *Advanced Materials*, **14**, 2, 99–117 (2002). DOI:10.1002/1521-4095(20020116)14:2<99::AID-ADMA99>3.0.CO;2-9.

[51] Hagen Klauk, Marcus Halik, Ute Zschieschang, Günter Schmid, Wolfgang Radlik and Werner Weber. High-mobility polymer gate dielectric pentacene thin film transistors. *Journal of Applied Physics*, **92**, 9, 5259 (2002). DOI:doi:10.1063/1.1511826.

[52] Manabu Kiguchi, Manabu Nakayama, Kohei Fujiwara, Keiji Ueno, Toshihiro Shimada and Koichiro Saiki. Accumulation and depletion layer thicknesses in organic field effect transistors. *Japanese Journal of Applied Physics*, **42**, Part 2, No. 12A, L1408–L1410 (2003). DOI:10.1143/JJAP.42.L1408.

[53] R. Ruiz, A. Papadimitratos, A. C. Mayer and G. G. Malliaras. Thickness dependence of mobility in pentacene thin-film transistors. *Advanced Materials*, **17**, 14, 1795–1798 (2005). DOI:10.1002/adma.200402077.

[54] Arian Shehu, Santiago D. Quiroga, Pasquale D'Angelo, Cristiano Albonetti, Francesco Borgatti, Mauro Murgia, Andrea Scorzoni, Pablo Stoliar and Fabio Biscarini. Layered distribution of charge carriers in organic thin film transistors. *Physical Review Letters*, **104**, 24, 246602 (2010). DOI:10.1103/PhysRevLett.104.246602.

[55] Simon M. Sze. *Semiconductor Devices: Physics and Technology*. John Wiley & Sons, Singpore (1985).

[56] Shengwen Luan and Gerold W. Neudeck. An experimental study of the source/drain parasitic resistance effects in amorphous silicon thin film transistors. *Journal of Applied Physics*, **72**, 2, 766–772 (1992). DOI:doi:10.1063/1.351809.

[57] E. J. Meijer, G. H. Gelinck, E. van Veenendaal, B.-H. Huisman, D. M. de Leeuw and T. M. Klapwijk. Scaling behavior and parasitic series resistance in disordered organic field-effect transistors. *Applied Physics Letters*, **82**, 25, 4576–4578 (2003). DOI:doi:10.1063/1.1581389.

[58] Jana Zaumseil, Kirk W. Baldwin and John A. Rogers. Contact resistance in organic transistors that use source and drain electrodes formed by soft contact lamination. *Journal of Applied Physics*, **93**, 10, 6117 (2003). DOI:10.1063/1.1568157.

[59] Peter V. Necliudov, Michael S. Shur, David J. Gundlach and Thomas N. Jackson. Contact resistance extraction in pentacene thin film transistors. *Solid-State Electronics*, **47**, 2, 259–262 (2003). DOI:16/S0038-1101(02)00204-6.

[60] L. D. López-Carreño, G. Benítez, L. Viscido, J. M. Heras, F. Yubero, J. P. Espinós and A. R. González-Elipe. Oxidation of molybdenum surfaces by reactive oxygen plasma and O_2^+ bombardment: an auger and XPS study. *Surface and Interface Analysis*, **26**, 4, 235–241 (1998). DOI:10.1002/(SICI)1096-9918(199804)26:4<235::AID-SIA360>3.0.CO;2-A.

[61] Woong-Kwon Kim, Bang Joo Song, Kihyon Hong, Kisoo Kim and Jong-Lam Lee. Effect of O2-plasma treatment of Mo on the crystal growth mode of pentacene of organic thin-film transistors. *Journal of The Electrochemical Society*, **156**, 8, H674–H678 (2009). DOI:10.1149/1.3153121.

[62] J. C. Vickerman and Ian S. Gilmore. *Surface analysis: the principal techniques*. Wiley & Sons Ill., Chichester, U.K, 2nd ed edition (2009). ISBN 9780470017630.

[63] H. Hertz. Ueber einen Einfluss des ultravioletten Lichtes auf die electrische Entladung. *Annalen der Physik*, **267**, 8, 983–1000 (1887). DOI:10.1002/andp.18872670827.

[64] A. Einstein. Über einen die Erzeugung und Verwandlung des Lichtes betreffenden heuristischen Gesichtspunkt. *Annalen der Physik*, **322**, 6, 132–148 (1905). DOI:10.1002/andp.19053220607.

[65] John E. Anthony. The larger acenes: Versatile organic semiconductors. *Angewandte Chemie International Edition*, **47**, 3, 452–483 (2008). DOI:10.1002/anie.200604045.

[66] I. P. M. Bouchoms, W. A. Schoonveld, J. Vrijmoeth and T. M. Klapwijk. Morphology identification of the thin film phases of vacuum evaporated pentacene on SiO2 substrates. *Synthetic Metals*, **104**, 3, 175–178 (1999). DOI:10.1016/S0379-6779(99)00050-8.

[67] Ricardo Ruiz, Alex C Mayer, George G Malliaras, Bert Nickel, Giacinto Scoles, Alexander Kazimirov, Hyunjung Kim, Randall L Headrick and Zahirul Islam. Structure of pentacene thin films. *Applied Physics Letters*, **85**, 21, 4926–4928 (2004). DOI:doi:10.1063/1.1826229.

[68] C. D. Dimitrakopoulos, A. R. Brown and A. Pomp. Molecular beam deposited thin films of pentacene for organic field effect transistor applications. *Journal of Applied Physics*, **80**, 4, 2501–2508 (1996). DOI:doi:10.1063/1.363032.

[69] Sandra E. Fritz, Stephen M. Martin, C. Daniel Frisbie, Michael D. Ward and Michael F. Toney. Structural characterization of a pentacene monolayer on an amorphous SiO2 substrate with grazing incidence X-ray diffraction. *Journal of the American Chemical Society*, **126**, 13, 4084–4085 (2004). DOI:10.1021/ja049726b.

[70] Hiroyuki Yoshida, Katsuhiko Inaba and Naoki Sato. X-ray diffraction reciprocal space mapping study of the thin film phase of pentacene. *Applied Physics Letters*, **90**, 18, 181930–181930–3 (2007). DOI:doi:10.1063/1.2736193.

[71] P. G. Schroeder, C. B. France, J. B. Park and B. A. Parkinson. Energy level alignment and two-dimensional structure of pentacene on Au(111) surfaces. *Journal of Applied Physics*, **91**, 5, 3010–3014 (2002). DOI:doi:10.1063/1.1445286.

[72] Joo H. Kang and X.-Y. Zhu. Pi-stacked pentacene thin films grown on Au(111). *Applied Physics Letters*, **82**, 19, 3248–3250 (2003). DOI:doi:10.1063/1.1572554.

[73] Daniel Käfer, Lars Ruppel and Gregor Witte. Growth of pentacene on clean and modified gold surfaces. *Physical Review B*, **75**, 8, 085309 (2007). DOI:10.1103/PhysRevB.75.085309.

[74] Sirapat Pratontep, Martin Brinkmann, Frank Nësch and Libero Zuppiroli. Nucleation and growth of ultrathin pentacene films on silicon dioxide: effect of deposition rate and substrate temperature. *Synthetic Metals*, **146**, 3, 387–391 (2004). DOI:10.1016/j.synthmet.2004.08.017.

[75] Hirotomo Yanagisawa, Tsuyoshi Tamaki, Masakazu Nakamura and Kazuhiro Kudo. Structural and electrical characterization of pentacene films on SiO2 grown by molecular beam deposition. *Thin Solid Films*, **464-465**, 398–402 (2004). DOI:10.1016/j.tsf.2004.06.065.

[76] Sirapat Pratontep, Martin Brinkmann, Frank Nüesch and Libero Zuppiroli. Correlated growth in ultrathin pentacene films on silicon oxide: Effect of deposition rate. *Physical Review B*, **69**, 16, 165201 (2004). DOI:10.1103/PhysRevB.69.165201.

[77] F.-J. Meyer zu Heringdorf, M. C. Reuter and R. M. Tromp. The nucleation of pentacene thin films. *Applied Physics A*, **78**, 6, 787–791 (2004). DOI:10.1007/s00339-003-2432-x.

[78] Ricardo Ruiz, Leonard C. Feldman, Richard F. Haglund, Rodney A. McKee, Norbert Koch, Bert A. Nickel, Jens Pflaum, Giacinto Scoles and Antoine Kahn. Growth and morphology of pentacene films on oxide surfaces. In *Materials Research Society Symposium - Proceedings*, volume 708, (pages 415–421) (2002). DOI:10.1557/PROC-708-BB10.54.

[79] Joyce G. Laquindanum, Howard E. Katz, Andrew J. Lovinger and Ananth Dodabalapur. Morphological origin of high mobility in pentacene thin-film transistors. *Chemistry of Materials*, **8**, 11, 2542–2544 (1996). DOI:10.1021/cm9603664.

[80] Sang Chul Lim, Seong Hyun Kim, Jung Hun Lee, Mi Kyung Kim, Do Jin Kim and Taehyoung Zyung. Surface-treatment effects on organic thin-film transistors. *Synthetic Metals*, **148**, 1, 75–79 (2005). DOI:10.1016/j.synthmet.2004.08.034.

[81] Karthik Shankar and Thomas N. Jackson. Morphology and electrical transport in pentacene films on silylated oxide surfaces. *Journal of Materials Research*, **19**, 07, 2003–2007 (2004). DOI:10.1557/JMR.2004.0255.

[82] S. Y. Yang, K. Shin and C. E. Park. The effect of gate-dielectric surface energy on pentacene morphology and organic field-effect transistor characteristics. *Advanced Functional Materials*, **15**, 11, 1806–1814 (2005). DOI:10.1002/adfm.200400486.

[83] D. Knipp, R. A Street, A. Völkel and J. Ho. Pentacene thin film transistors on inorganic dielectrics: Morphology, structural properties, and electronic transport. *Journal of Applied Physics*, **93**, 1, 347–355 (2003). DOI:doi:10.1063/1.1525068.

[84] W.Y. Chou, Y.S. Mai, H.L. Cheng, C.Y. Yeh, C.W. Kuo, F.C. Tang, D.Y. Shu, T.R. Yew and T.C. Wen. Correlation of growth of pentacene films at various gas ambience conditions to organic field-effect transistor characteristics. *Organic Electronics*, **7**, 6, 445–451 (2006). DOI:10.1016/j.orgel.2006.05.007.

[85] Aldo Brillante, Ivano Bilotti, Raffaele Guido Della Valle, Elisabetta Venuti, Alberto Girlando, Matteo Masino, Fabiola Liscio, Silvia Milita, Cristiano Albonetti, Pasquale D'angelo, Arian Shehu and Fabio Biscarini. Structure and dynamics of pentacene on SiO_2: from monolayer to bulk structure. *Physical Review B*, **85**, 19, 195308 (2012). DOI:10.1103/PhysRevB.85.195308.

[86] I. Horcas, R. Fernández, J. M. Gómez-Rodríguez, J. Colchero, J. Gómez-Herrero and A. M. Baro. WSXM: a software for scanning probe microscopy and a tool for nanotechnology. *Review of Scientific Instruments*, **78**, 1, 013705–013705–8 (2007). DOI:doi:10.1063/1.2432410.

[87] I. Kymissis, C.D. Dimitrakopoulos and S. Purushothaman. High-performance bottom electrode organic thin-film transistors. *Electron Devices, IEEE Transactions on*, **48**, 6, 1060 –1064 (2001). DOI:10.1109/16.925226.

[88] Jae Bon Koo, Seong Hyun Kim, Jung Hun Lee, Chan Hoe Ku, Sang Chul Lim and Taehyoung Zyung. The effects of surface treatment on device performance in pentacene-based thin film transistor. *Synthetic Metals*, **156**, 2–4, 99–103 (2006). DOI:10.1016/j.synthmet.2005.10.016.

[89] M. McDowell, I. G Hill, J. E McDermott, S. L Bernasek and J. Schwartz. Improved organic thin-film transistor performance using novel self-assembled monolayers. *Applied Physics Letters*, **88**, 7, 073505–073505–3 (2006). DOI:doi:10.1063/1.2173711.

[90] David J. Gundlach, Chung-Chen S. Kuo, Chris D. Sheraw, Jonathan A. Nichols and Thomas N. Jackson. Improved organic thin film transistor performance using chemically modified gate dielectrics. In *Proceedings of SPIE*, volume 4466, (pages 54–64) (2001). DOI:10.1117/12.451466.

[91] Max Shtein, Jonathan Mapel, Jay B. Benziger and Stephen R. Forrest. Effects of film morphology and gate dielectric surface preparation on the electrical characteristics of organic-vapor-phase-deposited pentacene thin-film transistors. *Applied Physics Letters*, **81**, 2, 268 (2002). DOI:10.1063/1.1491009.

[92] D.J. Gundlach, C.-C. Kuo, S.F. Nelson and T.N. Jackson. Organic thin film transistors with field effect mobility $>2\,\mathrm{cm}^2$/V-s. In *De-*

vice Research Conference Digest, 1999 57th Annual, (pages 164 –165) (1999). DOI:10.1109/DRC.1999.806357.

[93] Helmut Schift, Sina Saxer, Sunggook Park, Celestino Padeste, Uwe Pieles and Jens Gobrecht. Controlled co-evaporation of silanes for nanoimprint stamps. *Nanotechnology*, **16**, 5, S171 (2005). DOI:10.1088/0957-4484/16/5/007.

[94] M. F. Calhoun, J. Sanchez, D. Olaya, M. E. Gershenson and V. Podzorov. Electronic functionalization of the surface of organic semiconductors with self-assembled monolayers. *Nature Materials*, **7**, 1, 84–89 (2008). DOI:10.1038/nmat2059.

[95] Wei-Qiao Deng and William A. Goddard. Predictions of hole mobilities in oligoacene organic semiconductors from quantum mechanical calculations. *The Journal of Physical Chemistry B*, **108**, 25, 8614–8621 (2004). DOI:10.1021/jp0495848.

[96] X. Linda Chen, Andrew J. Lovinger, Zhenan Bao and Joyce Sapjeta. Morphological and transistor studies of organic molecular semiconductors with anisotropic electrical characteristics. *Chemistry of Materials*, **13**, 4, 1341–1348 (2001). DOI:10.1021/cm0008563.

[97] T. Muck, V. Wagner, U. Bass, M. Leufgen, J. Geurts and L.W. Molenkamp. In situ electrical characterization of DH4T field-effect transistors. *Synthetic Metals*, **146**, 3, 317–320 (2004). DOI:10.1016/j.synthmet.2004.08.010.

[98] Fabiola Liscio, Cristiano Albonetti, Katharina Broch, Arian Shehu, Santiago David Quiroga, Laura Ferlauto, Christian Frank, Stefan Kowarik, Roberto Nervo, Alexander Gerlach, Silvia Milita, Frank Schreiber and Fabio Biscarini. Molecular reorganization in organic field-effect transistors and its effect on two-dimensional charge transport pathways. *ACS Nano*, **7**, 2, 1257–1264 (2013). DOI:10.1021/nn304733w.

[99] Shun-Wei Liu, Chih-Chien Lee, Hung-Lin Tai, Je-Min Wen, Jiun-Haw Lee and Chin-Ti Chen. In situ electrical characterization of the thickness dependence of organic field-effect transistors with 1–20 molecular monolayer of pentacene. *ACS Applied Materials & Interfaces*, **2**, 8, 2282–2288 (2010). DOI:10.1021/am1003377.

[100] C. Tanase, E.J. Meijer, P.W.M. Blom and D.M. de Leeuw. Local charge carrier mobility in disordered organic field-effect transistors. *Organic Electronics*, **4**, 1, 33–37 (2003). DOI:10.1016/S1566-1199(03)00006-5.

[101] Daisuke Kumaki, Tokiyoshi Umeda and Shizuo Tokito. Reducing the contact resistance of bottom-contact pentacene thin-film transistors by employing a MoOx carrier injection layer. *Applied Physics Letters*, **92**, 1, 013301–013301–3 (2008). DOI:doi:10.1063/1.2828711.

[102] Jun Li, Hua-Ping Lin, Fang Zhou, Wen-Qing Zhu, Xue-Yin Jiang and Zhi-Lin Zhang. Suppression of bias stress-induced degradation of pentacene-TFT using MoOx interlayer. *Current Applied Physics*, **12**, 1, 280–283 (2012). DOI:10.1016/j.cap.2011.06.020.

[103] Jun Li, Xiao-Wen Zhang, Liang Zhang, Hao Zhang, Xue-Yin Jiang, Khizar ul Haq, Wen-Qing Zhu and Zhi-Lin Zhang. MoOx interlayer to enhance performance of pentacene-TFTs with low-cost copper electrodes. *Synthetic Metals*, **160**, 5-6, 376–379 (2010). DOI:10.1016/j.synthmet.2009.11.008.

[104] Masataka Kano, Takeo Minari and Kazuhito Tsukagoshi. Improvement of subthreshold current transport by contact interface modification in p-type organic field-effect transistors. *Applied Physics Letters*, **94**, 14, 143304–143304–3 (2009). DOI:doi:10.1063/1.3115826.

[105] Chih-Wei Chu, Sheng-Han Li, Chieh-Wei Chen, Vishal Shrotriya and Yang Yang. High-performance organic thin-film transistors with metal oxide/metal bilayer electrode. *Applied Physics Letters*, **87**, 19, 193508–193508–3 (2005). DOI:doi:10.1063/1.2126140.

[106] Zhaokui Wang, Mir Waqas Alam, Yanhui Lou, Shigeki Naka and Hiroyuki Okada. Enhanced carrier injection in pentacene thin-film transistors by inserting a MoO3-doped pentacene layer. *Applied Physics Letters*, **100**, 4, 043302–043302–4 (2012). DOI:doi:10.1063/1.3680249.

[107] Ching-Ting Lee and Hung-Chun Chen. Performance improvement mechanisms of organic thin-film transistors using MoOx-doped pentacene as channel layer. *Organic Electronics*, **12**, 11, 1852–1857 (2011). DOI:10.1016/j.orgel.2011.07.016.

[108] Jun Li, Fan Zhou, Hua-Ping Lin, Xue-Yin Jiang, Wen-Qing Zhu and Zhi-Lin Zhang. Tuning the contact resistance in organic thin-film transistors with an organic–inorganic hybrid interlayer. *Superlattices and Microstructures*, **50**, 2, 191–197 (2011). DOI:10.1016/j.spmi.2011.06.004.

[109] Mark T. Greiner, Michael G. Helander, Wing-Man Tang, Zhi-Bin Wang, Jacky Qiu and Zheng-Hong Lu. Universal energy-level alignment of molecules on metal oxides. *Nature Materials*, **11**, 1, 76–81 (2012). DOI:10.1038/nmat3159.

[110] V. Y. Butko, X. Chi, D. V. Lang and A. P. Ramirez. Field-effect transistor on pentacene single crystal. *Applied Physics Letters*, **83**, 23, 4773 (2003). DOI:10.1063/1.1631736.

[111] Tatjana Hähnlen, Claudio Vanoni, Christian Wäckerlin, Thomas A. Jung and Soichiro Tsujino. Surface doping in pentacene thin-film transistors with few monolayer thick channels. *Applied Physics Letters*, **101**, 3, 033305–033305–4 (2012). DOI:doi:10.1063/1.4737214.

[112] Jürgen Ristein. Surface transfer doping of diamond. *Journal of Physics D: Applied Physics*, **39**, R71–R81 (2006). DOI:10.1088/0022-3727/39/4/R01.

[113] Kozo Mukai and Jun Yoshinobu. Observation of charge transfer states of F4TCNQ on the 2-methylpropene chemisorbed Si(100)(2x1) surface. *Journal of Electron Spectroscopy and Related Phenomena*, **174**, 1-3, 55–58 (2009). DOI:10.1016/j.elspec.2009.04.006.

[114] W. Chen, X. Y. Gao, D. C. Qi, S. Chen, Z. K. Chen and A. T. S. Wee. Surface-transfer doping of organic semiconductors using functionalized self-assembled monolayers. *Advanced Functional Materials*, **17**, 8, 1339–1344 (2007). DOI:10.1002/adfm.200601029.

[115] Kentaro Harada, Mao Sumino, Chihaya Adachi, Saburo Tanaka and Koji Miyazaki. Improved thermoelectric performance of organic thin-film elements utilizing a bilayer structure of pentacene and 2,3,5,6-tetrafluoro-7,7,8,8-tetracyanoquinodimethane (F4-TCNQ). *Applied Physics Letters*, **96**, 25, 253304 (2010). DOI:10.1063/1.3456394.

[116] R. C. Haddon, A. S. Perel, R. C. Morris, T. T. M. Palstra, A. F. Hebard and R. M. Fleming. C60 thin film transistors. *Applied Physics Letters*, **67**, 1, 121–123 (1995). DOI:doi:10.1063/1.115503.

[117] Simon J. Noever, Stefan Fischer and Bert Nickel. Dual channel operation upon n-channel percolation in a pentacene-C60 ambipolar organic thin film transistor. *Advanced Materials*, **25**, 15, 2147–2151 (2013). DOI:10.1002/adma.201203964.

[118] Christian Wäckerlin, Dorota Chylarecka, Armin Kleibert, Kathrin Müller, Cristian Iacovita, Frithjof Nolting, Thomas A. Jung and Nirmalya Ballav. Controlling spins in adsorbed molecules by a chemical switch. *Nature Communications*, **1**, 61 (2010). DOI:10.1038/ncomms1057.

[119] Christian Wäckerlin, Kartick Tarafder, Dorota Siewert, Jan Girovsky, Tatjana Hähnlen, Cristian Iacovita, Armin Kleibert,

Frithjof Nolting, Thomas A. Jung, Peter M. Oppeneer and Nirmalya Ballav. On-surface coordination chemistry of planar molecular spin systems: novel magnetochemical effects induced by axial ligands. *Chemical Science*, **3**, 11, 3154–3160 (2012). DOI:10.1039/C2SC20828H.

[120] Christian Wäckerlin, Jan Nowakowski, Shi-Xia Liu, Michael Jaggi, Dorota Siewert, Jan Girovsky, Aneliia Shchyrba, Tatjana Hählen, Armin Kleibert, Peter M. Oppeneer, Frithjof Nolting, Silvio Decurtins, Thomas A. Jung and Nirmalya Ballav. Two-dimensional supramolecular electron spin arrays. *Advanced Materials*, **25**, 17, 2404–2408 (2013). DOI:10.1002/adma.201204274.

[121] Christian Wäckerlin, Kartick Tarafder, Jan Girovsky, Jan Nowakowski, Tatjana Hählen, Aneliia Shchyrba, Dorota Siewert, Armin Kleibert, Frithjof Nolting, Peter M. Oppeneer, Thomas A. Jung and Nirmalya Ballav. Ammonia coordination introducing a magnetic moment in an on-surface low-spin porphyrin. *Angewandte Chemie International Edition*, **52**, 17, 4568–4571 (2013). DOI:10.1002/anie.201208028.

[122] Weiying Gao and Antoine Kahn. Controlled p-doping of zinc phthalocyanine by coevaporation with tetrafluorotetracyanoquinodimethane: A direct and inverse photoemission study. *Applied Physics Letters*, **79**, 4040 (2001). DOI:10.1063/1.1424067.

[123] L. Scudiero, Dan E. Barlow, Ursula Mazur and K. W. Hipps. Scanning tunneling microscopy, orbital-mediated tunneling spectroscopy, and ultraviolet photoelectron spectroscopy of metal(II) tetraphenylporphyrins deposited from vapor. *J. Am. Chem. Soc.*, **123**, 17, 4073–4080 (2001). DOI:10.1021/ja0100726.

[124] S Kang, Y Yi, C Kim, S Cho, M Noh, K Jeong and C Whang. Energy level diagrams of C60/pentacene/Au and pentacene/C60/Au. *Synthetic Metals*, **156**, 32–37 (2006). DOI:10.1016/j.synthmet.2005.10.001.

[125] G. Beernink, T. Strunskus, G. Witte and Ch. Wöll. Importance of dewetting in organic molecular-beam deposition: Pentacene on gold. *Applied Physics Letters*, **85**, 3, 398–400 (2004). DOI:10.1063/1.1775040.

[126] Norbert Koch, Steffen Duhm, Jürgen P. Rabe, Antje Vollmer and Robert L. Johnson. Optimized hole injection with strong electron acceptors at organic-metal interfaces. *Physical Review Letters*, **95**, 23, 237601 (2005). DOI:10.1103/PhysRevLett.95.237601.

[127] Dorota Chylarecka, Christian Wäckerlin, Timur K. Kim, Kathrin Müller, Frithjof Nolting, Armin Kleibert, Nirmalya Ballav and

Thomas A. Jung. Self-assembly and superexchange coupling of magnetic molecules on oxygen-reconstructed ferromagnetic thin film. *The Journal of Physical Chemistry Letters*, **1**, 9, 1408–1413 (2010). DOI:10.1021/jz100253c.

[128] Hisao Ishii, Kiyoshi Sugiyama, Eisuke Ito and Kazuhiko Seki. Energy level alignment and interfacial electronic structures at Organic/Metal and Organic/Organic interfaces. *Advanced Materials*, **11**, 8, 605–625 (1999). DOI:10.1002/(SICI)1521-4095(199906)11:8<605::AID-ADMA605>3.0.CO;2-Q.

[129] Gilles Horowitz. Organic thin film transistors: From theory to real devices. *Journal of Materials Research*, **19**, 07, 1946–1962 (2004). DOI:10.1557/JMR.2004.0266.

[130] Manabu Kiguchi, Manabu Nakayama, Toshihiro Shimada and Koichiro Saiki. Electric-field-induced charge injection or exhaustion in organic thin film transistor. *Physical Review B*, **71**, 3, 035332 (2005). DOI:10.1103/PhysRevB.71.035332.

[131] Michael Shur, Michael Hack and John G. Shaw. A new analytic model for amorphous silicon thin-film transistors. *Journal of Applied Physics*, **66**, 7, 3371–3380 (1989). DOI:doi:10.1063/1.344481.

[132] O. Tal, Y. Rosenwaks, Y. Preezant, N. Tessler, C. K. Chan and A. Kahn. Direct determination of the hole density of states in undoped and doped amorphous organic films with high lateral resolution. *Physical Review Letters*, **95**, 25, 256405 (2005). DOI:10.1103/PhysRevLett.95.256405.

[133] S. Yogev, E. Halpern, R. Matsubara, M. Nakamura and Y. Rosenwaks. Direct measurement of density of states in pentacene thin film transistors. *Physical Review B*, **84**, 16, 165124 (2011). DOI:10.1103/PhysRevB.84.165124.

[134] Inc. Wolfram Research. *Mathematica Edition: Version 9.0*. Wolfram Research, Inc., Champaign, Illinois (2012).

[135] A. Sharma, F. W. A. van Oost, M. Kemerink and P. A. Bobbert. Dimensionality of charge transport in organic field-effect transistors. *Physical Review B*, **85**, 23, 235302 (2012). DOI:10.1103/PhysRevB.85.235302.

[136] Steffen Duhm, Ingo Salzmann, Benjamin Bröker, Hendrik Glowatzki, Robert L. Johnson and Norbert Koch. Interdiffusion of molecular acceptors through organic layers to metal substrates mimics doping-related energy level shifts. *Applied Physics Letters*, **95**, 093305 (2009). DOI:10.1063/1.3213547.

[137] Joachim Stöhr and Hans Christoph Siegmann. *Magnetism - From Fundamentals to Nanoscale Dynamics*. Springer (2006). ISBN 9783540302827.

[138] U. Flechsig, F. Nolting, A. Fraile Rodríguez, J. Krempaský, C. Quitmann, T. Schmidt, S. Spielmann and D. Zimoch. Performance measurements at the SLS SIM beamline. In *AIP Conference Proceedings*, volume 1234, (pages 319–322). American Institute of Physics (2010). DOI:10.1063/1.3463200.

[139] Christian Wäckerlin, Pablo Maldonado, Lena Arnold, Aneliia Shchyrba, Jan Girovsky, Jan Nowakowski, Md Ehesan Ali, Tatjana Hählen, Milos Baljozovic, Dorota Siewert, Armin Kleibert, Klaus Müllen, Peter M. Oppeneer, Thomas A. Jung and Nirmalya Ballav. Magnetic exchange coupling of a synthetic Co(II)-complex to a ferromagnetic Ni substrate. *Chemical Communications*, **49**, 91, 10736–10738 (2013). DOI:10.1039/C3CC45401K.

[140] Kuo-Chuan Ho and Yi-Ham Tsou. Chemiresistor-type NO gas sensor based on nickel phthalocyanine thin films. *Sensors and Actuators B: Chemical*, **77**, 1-2, 253–259 (2001). DOI:16/S0925-4005(01)00742-0.

[141] Kuo-Chuan Ho, Chun-Ming Chen and Jung-Yu Liao. Enhancing chemiresistor-type NO gas-sensing properties using ethanol-treated lead phthalocyanine thin films. *Sensors and Actuators B: Chemical*, **108**, 1-2, 418–426 (2005). DOI:16/j.snb.2004.12.109.

[142] C. J. Liu, J. J. Shih and Y. H. Ju. Surface morphology and gas sensing characteristics of nickel phthalocyanine thin films. *Sensors and Actuators B: Chemical*, **99**, 2-3, 344–349 (2004). DOI:16/j.snb.2003.11.034.

Publication list

Scientific articles

1. Tatjana Hählen, Claudio Vanoni, Christian Wäckerlin, Thomas A. Jung and Soichiro Tsujino. Surface doping in pentacene thin-film transistors with few monolayer thick channels. *Applied Physics Letters*, **101**, 3, 033305–033305–4 (2012). DOI:doi:10.1063/1.4737214

2. Christian Wäckerlin, Kartick Tarafder, Dorota Siewert, Jan Girovsky, Tatjana Hählen, Cristian Iacovita, Armin Kleibert, Frithjof Nolting, Thomas A. Jung, Peter M. Oppeneer and Nirmalya Ballav. On-surface coordination chemistry of planar molecular spin systems: novel magnetochemical effects induced by axial ligands. *Chemical Science*, **3**, 11, 3154–3160 (2012). DOI:10.1039/C2SC20828H

3. Christian Wäckerlin, Jan Nowakowski, Shi-Xia Liu, Michael Jaggi, Dorota Siewert, Jan Girovsky, Aneliia Shchyrba, Tatjana Hählen, Armin Kleibert, Peter M. Oppeneer, Frithjof Nolting, Silvio Decurtins, Thomas A. Jung and Nirmalya Ballav. Two-dimensional supramolecular electron spin arrays. *Advanced Materials*, **25**, 17, 2404–2408 (2013). DOI:10.1002/adma.201204274

4. Christian Wäckerlin, Pablo Maldonado, Lena Arnold, Aneliia Shchyrba, Jan Girovsky, Jan Nowakowski, Md Ehesan Ali, Tatjana Hählen, Milos Baljozovic, Dorota Siewert, Armin Kleibert, Klaus Müllen, Peter M. Oppeneer, Thomas A. Jung and Nirmalya Ballav. Magnetic exchange coupling of a synthetic Co(II)-complex to a ferromagnetic Ni substrate. *Chemical Communications*, **49**, 91, 10736–10738 (2013). DOI:10.1039/C3CC45401K

5. Christian Wäckerlin, Kartick Tarafder, Jan Girovsky, Jan Nowakowski, Tatjana Hählen, Aneliia Shchyrba, Dorota Siewert, Armin Kleibert, Frithjof Nolting, Peter M. Oppeneer, Thomas A. Jung and Nirmalya Ballav. Ammonia coordination introducing a magnetic moment in an on-surface low-spin porphyrin. *Angewandte Chemie International Edition*, **52**, 17, 4568–4571 (2013). DOI:10.1002/anie.201208028

6. Tatjana Hählen, Thomas A. Jung and Soichiro Tsujino. Detection of monolayer charge transport in pentacene thin film transistor. *In preparation*

Conference contributions

Oral presentations

1. Tatjana Hählen, Claudio Vanoni, Thomas A. Jung and Soichiro Tsujino. Molecular surface doping of organic field effect transistor with a few monolayer channel thickness. *Joint Annual Meeting of SPS and ÖPG*, Lausanne, Switzerland (June 15–17, 2011)

2. Tatjana Hählen, Claudio Vanoni, Thomas A. Jung and Soichiro Tsujino. Surface transfer doping in an organic field effect transistor with a few monolayer channel thickness. *Molecular Electronics: From Organic Electronics to Single Molecules*, EMPA, Dübendorf, Switzerland (June 24, 2011)

3. Tatjana Hählen, Claudio Vanoni, Christian Wäckerlin, Thomas A. Jung and Soichiro Tsujino. Surface doping with different molecules on a few monolayer pentacene thin-film transistor. *E-MRS 2012 Spring Meeting*, Strasbourg, France (May 14–18, 2012)

4. Tatjana Hählen, Claudio Vanoni, Christian Wäckerlin, Thomas A. Jung and Soichiro Tsujino. Functional one monolayer thin pentacene thin film transistor and molecular surface doping. *Next Nano Stars*, Basel, Switzerland (March 3, 2013)

5. Tatjana Hählen, Claudio Vanoni, Christian Wäckerlin, Thomas A. Jung and Soichiro Tsujino. Channel thickness influencing the surface doping efficiency in pentacene thin film transistors. *International Conference on Organic Electronics (ICOE)*, Grenoble, France (June 18–20, 2013)

Poster presentations

1. Tatjana Hählen, Claudio Vanoni, Thomas A. Jung and Soichiro Tsujino. Molecular surface doping of pentacene monolayers in a field effect transistor. *European Conference on Molecular Electonics (ECME)*, Barcelona, Spain (September 7–10, 2011)

2. Tatjana Hählen, Claudio Vanoni, Christian Wäckerlin, Thomas A. Jung and Soichiro Tsujino. In-situ Surface Doping with Organic Electron Acceptors/Donors in Organic Thin-film Transistor Devices. *International Conference on the Physics of Semiconductors (ICPS)*, Zürich, Switzerland (July 29 – August 3, 2012)

3. Tatjana Hählen, Claudio Vanoni, Christian Wäckerlin, Thomas A. Jung and Soichiro Tsujino. Surface doping in organic thin film transistors with different doping molecules. *Swiss NanoConvention 2013*, Basel, Switzerland (May 23–24, 2013)

Acknowledgments

I would like to thank all the people who supported me during my PhD work at PSI being this by teaching, discussions or encouragement.

First of all I would like to thank Prof. Dr. Thomas Jung and Dr. Soichiro Tsujino for giving me the possibility to do my PhD thesis under their supervision and for their support during all this time. I especially thank Soichiro for always having time to discuss experimental results and their interpretation. Thanks for all your input and also your patience when I could not always as quickly follow your thoughts. Thanks to Thomas for teaching me more about scientific writing by giving inputs both for papers and this thesis. Thanks also to Dr. Michel Calame for accepting to be my referee and taking the time to carefully read my thesis.

I sincerely thank all people giving me technical support during this PhD work. Thanks to Rolf Schelldorfer for his knowledge and assistance with the experimental setup as well as with the AFM measurements. Thanks to Anja Weber for her help in the preparation of the sample templates. I also acknowledge the support of Koni, Arnold and Jana. Thanks also to Dr. Celestino Padeste for his introduction into the chemistry and the preparation of SAMs.

A special thanks goes also to Christian Wäckerlin who first introduced me into the UHV techniques. Thanks also for your help with the XPS and UPS measurements including the interpretation of the results. I also thank the other group members Dorota Siewert, Nirmalya Ballav, Jan Girovsky, Harald Rossmann, Jan Nowakowski, Aneliia Shchyrba and Milos Baljozovic. It was a pleasure to work with you, especially also during the intense beamtimes.

Thanks also to all the people from LMN who made my stay at PSI even more pleasant. Thanks for the interesting discussions and nice lunches. Stefan, Anja, Celestino, Salvo and Robert, thank you also for the nice discussions on the bus to and from PSI. A special thanks goes also to my two office mates Anna Mustonen and Nassir Mojarad. It was a pleasure sharing the office with you.

I also have to thank all my friends who supported and accompanied me during my PhD time. A special thanks goes to Nils, Dania, Anja, Philipp, Marietta, Daniela and Rahel.

Last but not least, I have to thank my family who supported me during all my studies and my PhD time. I especially thank my loved Christian who went with me through all ups and downs which come along such a thesis.